Abstract

Title of Dissertation: The Physics of High Altitude Lightning

Juan Alejandro Valdivia, Doctor of Philosophy, 1997

Dissertation directed by: Professor Dennis Papadopoulos
Department of Physics

It has been very surprising to discover in recent years that some of the energy dissipated by lightning can couple upwards into the upper atmosphere driving the impressive high altitude lightning phenomena. To understand these phenomena requires modeling of nonlinear processes driven by high electric power densities. The objective of this thesis is to provide the physics framework within which some of the observed phenomena can be studied and quantitatively understood and modeled.

The first part of the thesis deals with red sprites, the millisecond-long red optical flashes that stretch at altitudes between 50 - 90 km. In this thesis we set forth the hypothesis that the fractal nature of the lightning discharge is responsible for the presence of localized regions of high power density in the upper atmosphere while maintaining low average integrated power. Such inhomogeneous radiation pattern naturally reduces the required current threshold

for sprites to values closer to measurements as compared with dipole type of models. To understand the radiation pattern generated by the tortuous structure of lightning, fractal antennae are studied in detail, with special emphasis on the dependency on the fractal characteristics -the fractal dimension- of the discharge.

The second part of the thesis addresses the issue of the generation of the observed γ-ray flashes. The γ-rays observed are consistent with the generation of a runaway discharge. Runaway discharges have been studied only in the absence of a magnetic field. The magnetic field effect on the runaway discharge may be important at heights consistent with HAL since the gyromotion becomes more important than the other $B = 0$ time scales, e.g. collisions, ionization, etc. We developed the theory of the runaway discharge for $B \neq 0$. Results indicate that the threshold conditions for the runaway discharge are changed radically in the presence of the Earth's magnetic for heights above 20 km constraining the electron acceleration between the ionizing collisions, hence inhibiting the discharge. Consequently, runaway discharges driven by static electric fields are a very unlikely source of γ -rays and red sprites, requiring extremely large electric fields with amplitudes at least 10 times larger than expected.

The Physics of High Altitude Lightning

by

Juan Alejandro Valdivia

Dissertation submitted to the Faculty of the Graduate School of the
University of Maryland at College Park in partial fulfillment
of the requirements for the degree of
Doctor of Philosophy
1997

Advisory Committee:

Professor Dennis Papadopoulos, Chairman/Advisor
Professor A. S. Sharma
Professor A. Hassam
Professor R. Sagdeev
Professor J. Wang

Dedication

To my parents

Acknowledgements

I greatly appreciate the encouragement, guidance and friendship from my advisors Dennis Papadopoulos, Surja Sharma and Gennady Milikh. Dennis, for his invaluable intuition and for encouraging me to develop independently. I sincerely appreciate it. Surja, for his strong guidance, support and uncompromising example. Gennady, for his priceless commitment and help throughout the whole development of this thesis. Also, I want to thank David Book for some very interesting discussions.
Finally, I want to thank all the people I have played "futbol" with over the past years that made graduate school a very enjoyable experience.

The work was supported by: NSF grant ATM-9422594

Table of Contents

List of Tables

List of Figures

The Physics of High Altitude Lightning

Juan Alejandro Valdivia

May 23, 1997

This comment page is not part of the dissertation.

Typeset by LaTeX using the `dissertation` class by Pablo A. Straub, University of Maryland.

Part I

Introduction

Chapter 1

Observations, Models and Directions

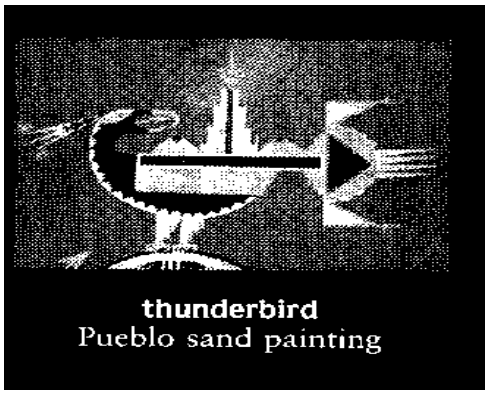

1.1 Lightning

Lightning preceded the presence of life on Earth, and according to some theories was instrumental in causing it. It has been present in the human culture since antiquity. In ancient Greece, Zeus would create lightning from the top of mount Olympus when he was in a bad mood. North American Indian tribes attribute lightning to the thunderbird. The thunderbird would produce lightning by flashing its feathers and thunder by flapping its wings.

Benjamin Franklin was the first to realize, as late as the mid 18th century, that lightning was an electrical phenomenon, by noticing the similarity of lightning with the sparks produced by rubbing a dielectric material. He conducted experiments to show that lightning was electrical and in 1750 invented the light-

ning rod as a protection against lightning. Figure 1.1 shows the famous kite experiment which demonstrated the electrical nature of lightning. This experiment, if conducted correctly, produces sparks from the hanging key to the ground.

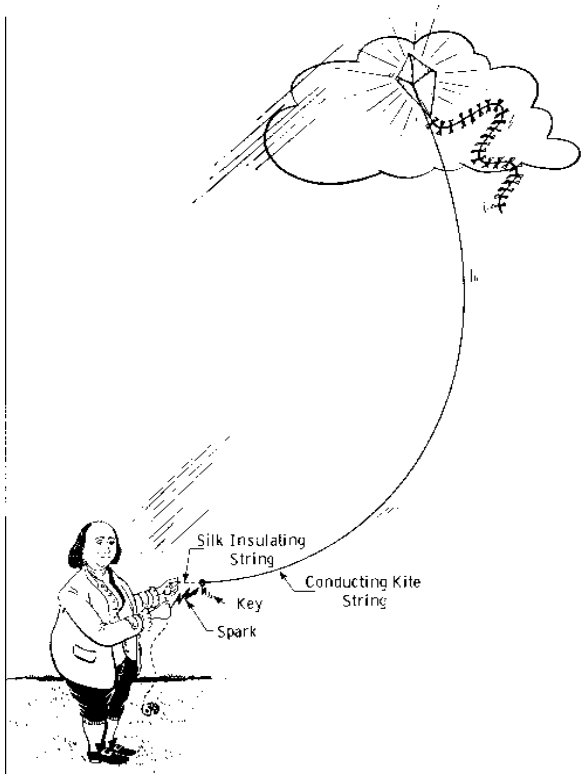

Figure 1.1: The famous kite experiment suggested and performed by B. Frankling to show that lightning was indeed an electrical phenomenon. If this experiment is performed in the wrong way, it may kill the experimentalist.

We can distinguish two types of lightning discharges, cloud-to-ground and intracloud. Most discharges observed from the ground are cloud-to-ground discharges. An example of a cloud-to-ground discharge, or stroke, is displayed in Fig. 1.2 which is taken form *Uman* [1987]. Lightning discharges are ultimately caused by the air motion around the clouds, causing charge separation. This stored energy is dissipated in the form of a lightning discharge or stroke. The

stroke starts with a stepped leader in a series of 1 μsec steps of length of about 50 m. Before the stepped discharge reaches the ground, a second discharge of the opposite charge starts from the ground. The two discharges meet shorting the circuit and a return stroke is formed which propagates upwards along the ionized channel lowering the charge.

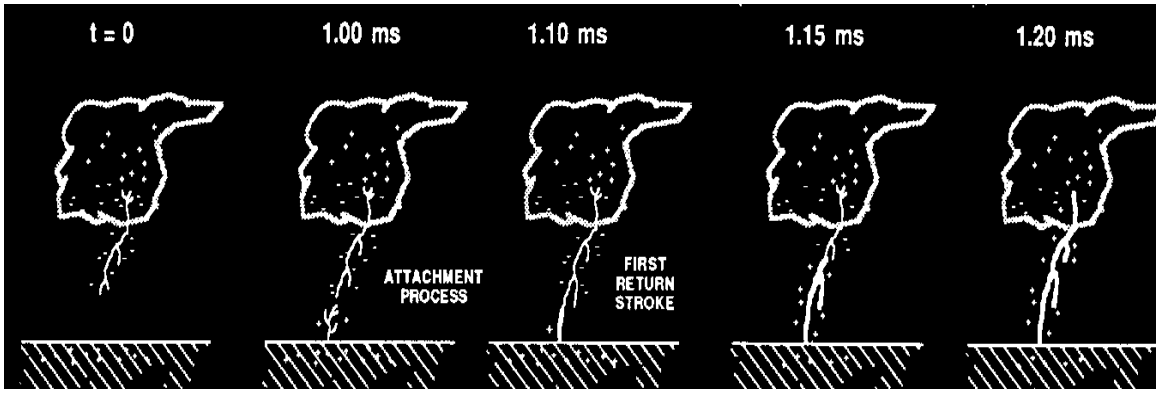

Figure 1.2: A cloud-to-ground lightning discharge. It starts with the stepped leader propagating down. Before the stepped discharge reaches the ground, a second discharge of the opposite charge starts from the ground. The two discharges meet shorting the circuit and a return stroke is formed which propagates upward lowering the charge. This picture is taken from Uman 1987.

The velocity of propagation of the return stroke is a fraction of the velocity of light [*Uman* 1987]. A cloud-to-ground discharge acts as a vertical electric dipole antenna and radiates predominantly in the horizontal direction. An intracloud discharge occurs mainly inside the cloud or between clouds in the horizontal direction. It acts as a horizontal electric dipole antenna radiating its energy predominantly upwards as well as downwards. *Uman* [1987] reports measurements of intracloud discharges suggesting a propagation speed equal to a fraction of the speed of light. The length of the discharge may reach tens, and sometimes

hundreds, of kms in the so called spider lightning mode [*Lyons*, 1994], hence generating a large dipole moment.

A lightning flash lasts for about 0.5 sec [*Uman* 1987] and is composed of a few strokes, which last for a few msec. A flash may discharge a charge as large as $Q = 100$ C which was originally separated by a distance, on average, of 5 km, dissipating about $\frac{9\times10^9 Q^2}{R} = 10^9 - 10^{10}$ J of energy and generating an average power of about $10^9 - 10^{10}$ W. Since the global flash rate, which is distributed preferentially near the equator, is about 100 flashes/sec, the total mean power generated globally by lightning is about $10^{11} - 10^{12}$ W. As a reference, the averaged power consumption of the United States is about 5×10^{11} W.

Most of the initial energy stored in the separated charge is dissipated in the form of heat and radio waves [*Uman* 1987]. In fact only a very small amount of energy is accessible, or released, at the ground in the case of a cloud-to-ground stroke. Lightning generates two types of electric fields: static electric fields are produced by the separated charge, while electromagnetic pulses (EMP) are produced by the moving charges as they are accelerated during the lightning stroke.

1.2 Observations of HAL

Over the years lightning was thought to be a predominantly low altitude (< 10 km) phenomenon with little of its energy coupling to the mesosphere and ionosphere. As a result, recent observations relating lightning to energy dissipation at altitudes between 30 and 90 km came as a major surprise. These phenomena, grouped under the name of high altitude lightning (HAL), include (a) Red sprites, (b) Blue jets, (c) Gamma ray bursts, (d) Radio bursts (e) more? A diagram referring to the different phenomena and the location of their occurrence is shown in Fig 1.3.

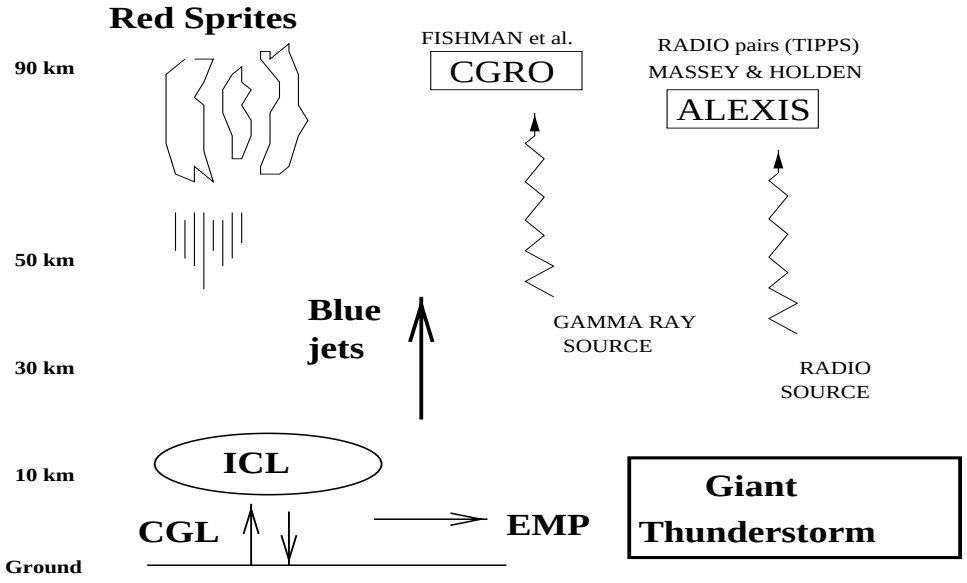

Figure 1.3: The different manifestations of High Altitude Lightning: (a) Red sprites, (b) Gamma ray burst, (c) Radio Burst, (d) Blue jets. These phenomena are associated with thunderstorms, e.g. intracloud lightning (ICL) or cloud-to-ground (CGL) lightning discharges.

Band	Energy	Range	Lifetime	Quenched	Color
$N_2(1P)$	7.35 eV	$500 < \lambda < 1100nm$	$8\mu sec$	< 60 km	Red
$N_2(2P)$	11.0 eV	$300 < \lambda < 500nm$	$0.04\mu sec$	< 40 km	Blue
$N_2^+(1N)$	3.17 eV	$300 < \lambda < 600nm$	$0.06\mu sec$	–	Blue
$O_2(B)$	1.63 eV	$200 < \lambda < 500nm$	$12sec$	< 90 km	Blue

Table 1.1: Optical bands

Besides the intrinsic scientific interest, HAL phenomena are important in that they can couple large amounts of energy to the upper atmosphere and provide a direct transient coupling between the ionosphere and the stratosphere, with implications to the global electric circuit of the earth and its atmosphere. The high altitude phenomena may also have important influence in the general chemistry composition of the atmosphere, e.g. blue jets occur around the ozone layer peak. Some of these phenomena are characterized, and in fact named, by their optical signatures or their emission spectrum (some of the relevant optical bands and their properties are listed in Table 1.1):

- **Red sprites** are millisecond-long optical flashes predominantly in the red that stretch at altitudes between 50 - 90 km, with horizontal extent of a few tens of kms. Their peak luminosity is about 10-100 kR (a Rayleigh corresponds to a photon flux of 10^6 $\frac{photons}{cm^2 s}$ column integrated), hence less than that of an average aurora. These high altitude optical flashes were detected more than 100 years ago [*Kerr*, 1994], however, interest on the subject was sparked recently, following the observations of a group at the University of Minnesota [*Franz et al.*, 1990] during tests of their low-light-level camera. Observations of these optical emissions have been the focus

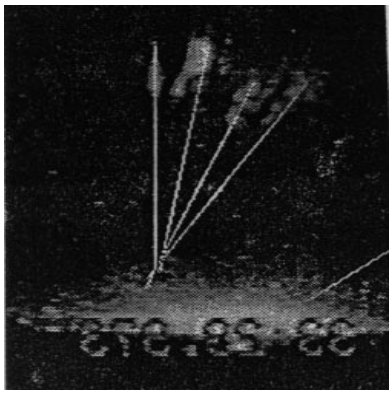

Figure 1.4: The photo of a red sprite showing clear fine spatial structure [Winckler et al., 1995].

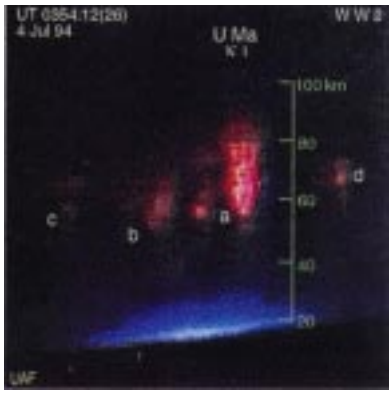

Figure 1.5: The optical emissions from a red sprite [Sentman et al. 1994].

of many recent ground and aircraft campaigns [*Boek et al.*, 1992; *Vaughan et al.*, 1992; *Winckler et al.*, 1993; *Sentman et al.*, 1993; *Lyons* , 1994]. Two examples are shown in Fig. 1.4 and Fig. 1.5 respectively. Red sprites are associated with the presence of massive thunderstorm clouds, although the luminous columns do not seem to touch the cloud tops. The generic anatomy of the red sprites was described by *Sentman et al.* [1995] and included faint bluish tendrils often extending downward from the main body of sprites. Among the most puzzling aspects of the observations is the presence of fine structure in the emissions [*Winckler et al.* 1996]. Vertical striations with horizontal size of 1 km or smaller, often limited by the instrumental resolution, are apparent in the red sprite emissions. The relatively limited number of observations does not allow a proper statistics of its occurrence. *Sentman and Wescott* [1993] reported that red sprites occur in about 0.5-1 % of the ordinary lightning events, while *Lyon*'s observations indicate a higher occurrence rate.

- **Blue jets** are predominantly blue structures that propagate with an upward speed of about 100 km/sec from the cloud top to an altitude of up to $40-50$ km with about 100 msec duration [*Westcott et al.* , 1995]. The blue color is probably due to the excitation and subsequent emission of the $N_2(2P)$ and $N_2^+(1N)$ bands. The $N_2(1P)$ and O_2 (B) are collisionally quenched at these heights. Blue jets have a conical shape (Fig. 1.6) and an optical intensity of 10 kR. The total energy dissipated is of the order of 3×10^7 J. The blue jet propagation speed, close to 100 km/s, matches the electron low energy diffusion speed at the relevant heights.

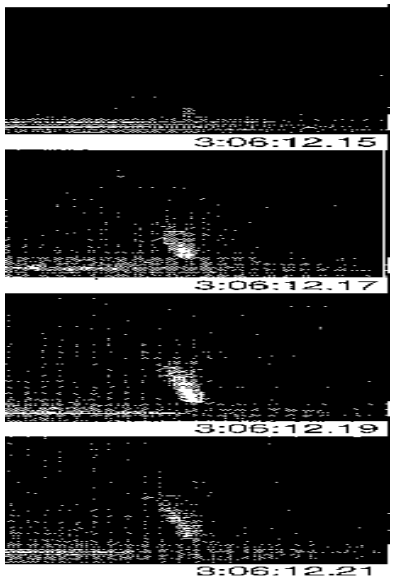

Figure 1.6: A blue jet propagating from the cloud top. It has an upward speed of about 100 km/s [Wescott et al., 1994].

- **Gamma-ray Bursts** were first observed by the Compton Gamma Ray Observatory (CGRO) in correlation with thunderstorms [*Fishman et al.*, 1994]. They have msec duration (Fig. 1.7) and a spectrum consistent

with bremsstrahlung emission of 1 MeV electrons. For the gamma rays to escape atmospheric absorption, the source should be located above 30 km in height. The emissions have an equivalent energy of 10-100 J.

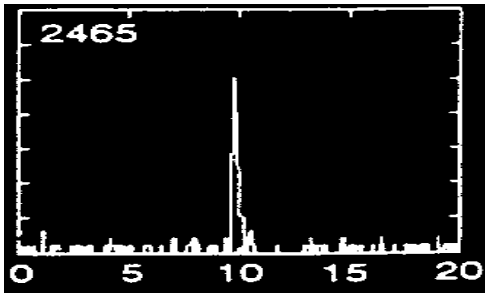

Figure 1.7: A gamma ray burst observed with CGRO[Fishman et al., 1994]. The x axis is in msec.

- Radio bursts of duration $3 - 5$ μsec, appearing mostly in pairs, were observed by the Alexis satellite [*Massey and Holden*, 1995]. Their frequency range is $25 - 100$ Mhz and their intensity 10^4 larger than normally generated by thunderstorms. The delay between the two radio bursts is about 20-60 μsec. The emissions have an energy of about 10^{-13} J/m^2 and are dispersed, signifying sub-ionospheric origin.

1.3 Models and Problems Associated with HAL

The observations associated with HAL phenomena came as a major surprise to the community. A number of models were proposed to account for the startling HAL observations. All the models considered electric fields - quasistatic (QS) or electromagnetic pulses (EMP) - as the agents responsible for transferring the energy form the lightning discharge site upwards. The coupling of this power to the upper atmosphere and lower ionosphere generates the observables discussed in section 1.2 (Fig. 1.3).

Lightning generates two types of fields. During the charging state - when the positive and negative charges are separated in the cloud - static fields are slowly generated in the atmosphere and ionosphere which are quickly (with time scale $\frac{1}{\epsilon_o \sigma} \sim 0.01$ sec at $h = 80$ km) neutralized in the weakly conducting atmosphere. When the lightning stroke occurs, the static fields are suddenly reduced in the ionosphere leaving for a short time an unbalanced electric field. Such a field could be responsible for the energy deposition and emissions. On the other hand, electromagnetic pulses (EMPs) are generated as the moving charges are accelerated during the lightning stroke. The EMPs transfer the energy to the ionosphere by energizing the ionospheric electrons. This energy transfer is then responsible for the emissions.

1.3.1 Red Sprites; Theories and Problems

Red sprites are a relatively new phenomenon, and only few attempts have been made to describe it. Early papers examined the EM radiation from lightning, using dipole models, and ignored the aspects of the energy coupling to the atmo-

sphere. *Farrell and Desch* [1992] discussed the radio emission spectrum due to the upward propagation of hypothetical return current pulses with 10 msec duration. Their model was intended to explain the absence of VLF emissions between 0.3–15 kHz associated with long-lasting discharges [*Nemzek and Winckler*, 1989; *Franz et al.*, 1990]. *Hale and Baginski* [1987] suggested that an electric field in the ionosphere can be induced by the monopole that remains in the cloud following the discharge. As indicated by *Farrell and Desch* [1993] the latter model has several difficulties, since it occurs on a temporal scale much longer than that of the observed events. *Krider* [1992; 1994] considered the electric field radiated by a return lightning stroke, and concluded that considerable fields can be produced in the lower ionosphere if the velocity of the stroke is close to the speed of light. However the physical mechanism which could produce the drastic increase of the lightning stroke speed remains unclear.

The first published theoretical model of red sprites [*Milikh et al.*, 1995], including energy deposition, associated the red sprite generation with transient electric fields induced by large intracloud lightning discharges, which were modeled as horizontal electric dipoles. Heating, ionization and emissions were computed using the results of a model developed by *Papadopoulos et al.* [1993a] for EMP atmospheric breakdown. They found the overall emissions consistent with a horizontal cloud discharge moment in excess of 6×10^3 C-km to produce the required emissions at heights of about $60 - 70$ km. The paper demonstrated that the energization of the ionospheric electrons by the transient fields could account for several of the observed features.

Two subsequent publications reached the same conclusion following a similar approach, but emphasizing different sources for the lightning generated electric

fields. The first [*Pasko et al.*, 1995], following an earlier suggestion of *Hale and Baginski* [1987], assumed that the dominant electric fields were laminar static fields established in the atmosphere after the lowering of a positive charge to the ground by a cloud-to-ground discharge, i.e. an electric monopole at an altitude of 10 km. They then proceeded to compute electron heating, ionization and emissions using the *Papadopoulos et al.* [1993a] model. They found that the overall emissions were consistent with discharges lowering in excess of 100 C of charge. The analysis emphasized the importance of dielectric relaxation on the field timescale. The second one [*Rowland et al.,* 1995] assumed that the fields were due to the transient far field of a vertical electric dipole generated by cloud-to-ground discharges and followed a similar analysis as *Milikh et al.*, [1995].

In comparing the laminar [*Pasko et al.*, 1995] and EMP [*Milikh et al.*, 1995; *Rowland et al.,* 1995] models against the observations we note that: all models can account for the color and the altitude of the maximum emission. To account for the total optical emission of 10-100 kR, both models require unrealistically large values in the discharge parameters. A reduction by a factor of 5-10 in the required charge, or cloud dipole moment, will be more in line with the statistics of the observations. Furthermore, the laminar model fails to account for the appearance of displaced pairs of red sprites. Displaced pairs occur naturally in the EMP model by considering energy deposition due to the part of the EM pulse reflected from the ground.

All of the above models, while successful in explaining some observed characteristics of the "red sprites', such as the color and the generation altitude of the emissions, suffer from two important drawbacks. First, dipole or monopole

distributions generate electric fields smoothly distributed at ionospheric heights, thereby failing to account for the persistent fine structure of the red sprites which show vertical striations with horizontal size of 1 km or smaller, often limited by the instrumental resolution [*Winckler et al.*,1996]. Second, the threshold current, or charge, and dipole moment requirements of all three models have been criticized as unrealistically large [*Uman, unpublished comment* 1995].

1.3.2 Gamma-Rays and Blue Jets; Theory and Problems

Interest in the runaway discharge was recently renewed by the unexpected observations of γ-ray flashes detected by the Compton Gamma-ray Observatory [CGRO] overflying massive thunderstorms in the equatorial regions [*Fishman et al.*, 1994]. It was shown that the observed γ-ray intensity and spectrum is consistent with bremsstrahlung, due to a beam of relativistic electrons with MeV average energy, generated at altitudes higher than 30 km. The generation altitude is a key requirement since γ-rays generated below 30 km will be absorbed by the atmosphere and will not reach satellite altitudes. Therefore, early speculations centered on the runaway discharge driven by the quasi-static fields induced by lightning [*Bell et al.*, 1995; *Roussel-Dupre and Gurevich*, 1996]. Such runaway air breakdown is an avalanche of electrons, started by a cosmic ray secondary, that get accelerated to relativistic energies in the presence of a sufficiently large electric field. *Taranenko and Roussel-Dupre* [1996] have proposed that "gamma ray flashes of atmospheric origin as well as blue jets and red sprites are naturally explained by high-discharges produced by runaway air breakdown". Such a relativistic electron discharge interacting with the ambient atmosphere would be responsible for the emissions observed in HAL.

Even though the source of gamma ray flashes and blue jets is probably connected with runaway air breakdown, such connection is not so clear for red sprites. The main objection is that all the standard runaway electric field threshold are radically increased in the presence of the Earth's magnetic field [*Gurevich et al.*, 1996; *Papadopoulos et al.*, 1996] which becomes relevant at heights over 20 kms at low latitudes. Therefore, for the later part of the blue jets, and certainly for any participation in the red sprite evolution, the Earth's magnetic field must be included in such models. This increase in the field threshold due to the presence of the Earth's magnetic field becomes the most important constraint in the modeling of these HAL phenomena, as produced by a runaway air breakdown. An additional problem with the runaway discharge at altitudes exceeding 60 km is that the ionization mean free path of the runaway electrons is longer than the scale height of the density gradient in the neutral ionosphere. Hence, the runaway electrons are free to escape the atmosphere.

1.4 Objectives and Directions of this Work

The main objective of this work is to explore the physical processes related to the newly discovered phenomena of high altitude lightning (HAL). We are interested in determining the essential features of lightning discharges and thunderstorms responsible for the observed HAL phenomena. In particular we will address the issues of red sprites and gamma ray flashes.

1.4.1 Red Sprites and Issues

As we mentioned in the previous section red sprite models based on the simple dipole lightning discharges suffer from a number of deficiencies. They don't account for the sprite's fine spatial structure and require large charge or current thresholds. To avoid these problems, in this thesis we considered and found that the self-similar structure of the lightning discharge introduces profound modifications in the intensity and structure of the electromagnetic field pattern at high altitudes.

It is well known that lightning discharges follow a tortuous path [*LeVine and Meneghini*, 1978]. *Williams* [1988] has shown that intracloud discharges resemble the well known Lichtenberg patterns observed in dielectric breakdown. These patterns have been recently identified as fractal structures of the Diffusion Limited Aggregate (DLA) type with a fractal dimension $D \approx 1.6$ [*Sander*, 1986; *Niemeyer et al.*, 1984]. By incorporating the dendritic fractal structure of the lightning channel as described by *Williams* [1988] and by *Lyons* [1994] (who termed it spider lightning) in the calculation of the lighting induced fields, results in a natural explanation of the observed fine structure of the red sprites and in a significant reduction of the required threshold charge or equivalent dipole moment.

Therefore, in this thesis we study the properties of fractal antennae in general.

Fractal Antennae

Besides its application to the sprite problem, fractal antennae are interesting in their own right. For example, fractal antennae are broadband and due to their

spatially structured gain could be of particular interest in ionospheric modification and in other settings [*Werner and Werner* , 1995; *Jaggard* 1990].

In particular, careful consideration will be given here to the dependence of the antenna gain on the fractal description of the antenna, e.g. its fractal dimension. Among the most relevant issues concerning fractal antennae, specially for lightning, is that their radiation pattern exhibit an increase in the radiated power density, at least at certain positions, as compared with non-fractal (dipole) models. It is this power density increase that will be responsible for reducing the required threshold current and charge to produce the red sprites. At the same time the spatial structure of red sprites can be understood in terms of the spatio-temporal radiation pattern of the fractal antenna. Due to the fractality, and its inherent power law distribution, the radiation pattern from the fractal antenna will be broadband, meaning that it will be relatively insensitive to the type of current pattern that produces the radiation.

Lightning and Red Sprites

The lightning discharge will radiate as a fractal antenna that, unlike a dipole antenna, generates a spatially non-uniform radiation pattern with regions of high field intensity and regions of low field intensity. The non-uniform radiation pattern can cause the observed fine structure of red sprites. Furthermore, such a fractal antenna naturally leads to an increase in the radiated power density, as compared with dipole-type models.

We apply the ideas from fractal antennae to the generation of red sprites. The concept of antenna gain and spatial structure will be given special consideration for specific fractal models of lightning discharges. Here we will include

the propagation, with self absorption, of the lightning induced radiation fields through the lower ionosphere, the heating of the ambient electrons, and the subsequent optical emissions. The required current (and charge) threshold and the emission pattern depend critically on the type of discharge, i.e. its dimension. The entire energy transfer process is modeled with the help of a Fokker-Planck code. This code was developed to study the modification of the electron distribution function [*Tsang et al.*, 1991] in the presence of field energization and inelastic loses.

The modeling of lightning as a fractal antennae reduces the required current (and charge) threshold for the production of sprites as compared with dipole models. Furthermore, such a fractal antenna naturally generates a spatially inhomogeneous emission pattern.

Red Sprite Spectrum

While the gross phenomenology of the emissions, termed red sprites, has been known for some time now, their spectroscopic structure is only currently emerging [*Mende et al.*, 1995; *Hampton et al.*, 1996]. We generated the first model of the red sprite spectrum, with the help of a Fokker-Planck code [*Tsang et al.*, 1991], that is based on the energization of ionospheric electrons by lightning induced fields. Comparison of the modeled spectrum with the measured ones [*Mende et al.*, 1995; *Hampton et al.*, 1996], constraints the local power density absorbed by the plasma and the electron energy spectrum in the emission region. This last result may help us discriminate among different models.

1.4.2 Generation of Runaway Beams

For heights of relevance to HAL phenomena, i.e. $h > 20$ km, the standard electron runaway process under a static electric field is strongly influenced by the presence of the magnetic field, specially close to the equator, where most of the thunderstorms occur and the γ-ray flashes observed. We have therefore, developed the theory of the runaway process under the influence of both electric **E** and magnetic **B** fields The conditions for the electron runaway are different from those described for a pure static electric field. In fact, the electric field threshold is critically increased in the presence of a magnetic field suggesting that the runaway process may be an improbable candidate as a source of HAL phenomena, at least for red sprites. We will estimate the size of the runaway basin in momentum space as a function of the electric and magnetic fields. Such determination will be relevant in understanding the feasibility of the runaway process in each situation. Furthermore, we will compute the diffusion coefficient in the presence of the magnetic field for the case of the E and B parallel.

1.5 Outline of the Thesis

The thesis is organized as following:

Chapter 2: Fractal antennae

- Present the theory of fractal antennae. Derive relations showing that phase coherence comes naturally from power law distribution of phases as opposed to more homogeneous or random distributions. An example is given for Cantor sets of radiators. More closely related to lightning we study in detail the properties of fractal antennae, e.g. tortuosity and branching.

The general conclusion is that the increase in the path length of a discharge increases the radiated power density.

- Concentrate on fractal discharge models and the properties of its radiated power density. Specifically, a stochastic model is used as a representation of a fractal lightning discharge that is easily parametrized by its fractal dimension. Comparison are made with simple fractal random walk models.

Chapter 3: Red Sprites

- Compute the field pattern projected to the lower ionosphere generated by our fractal lightning discharge models. A Fokker-Planck code is used to compute self-consistently the propagation and absorption of the field through the ionosphere. Compute the optical emission of the $N_2(1P)$ transition from the electric field pattern with the help of the Fokker-Planck code. The required threshold and the emission pattern dependence on the dimension of the discharge is studied. The main conclusion is that the emission pattern depends critically on the dimension of the discharge. Under the same conditions, the discharge current thresholds required to produce similar sprite intensities from certain fractal discharges can be considerably lower than for dipole models.

Chapter 4: Spectrum of Red Sprites

- Develop the model of the optical emission spectrum from the absorption region with the help of the Fokker-Planck code for the relevant transitions of $N_2(1P)$, $N_2(2P)$, $N_2^+(1N)$. For different field strengths compute the

synthetic spectrum. The same analysis can be repeated for the height dependent field profile from a fractal antenna. The synthetic spectra are compared with actual measurements after proper consideration of the wavelength dependent atmospheric attenuation. The field strength at the emission region can be estimated by comparing different lines in the measured spectrum.

Chapter 5: Runaway Discharges in the Presence of the Magnetic Field

- Review the theory of the conventional runaway discharge under a pure static field. Develop the theory of the runaway discharge under both electric and magnetic fields. Importance is given to the application of these results to HAL phenomena. The main conclusion is that the runaway air breakdown in its present theoretical form is an unlikely candidate for some of the HAL phenomena, especially for the generation of the red sprites, which requires very large fields produced with unrealistic discharge parameters, and prohibited by the fact that the atmospheric scale length becomes shorter than the ionization mean free path.

Part II

Red Sprites

Chapter 2

Fractal Antennae

2.1 Fractal Antennae and Coherence

For the purposes of this work, we assume that a fractal antenna can be formed as an array of "small" line elements having a fractal distribution in space. Such description is consistent with our understanding of fractal discharges and lightning observations as discussed by *LeVine and Meneghini* [1978], *Niemeyer et al.* [1984], *Sander* [1986], *Williams* [1988], and *Lyons* [1994]. Appendix A develops the theory for the calculation of the fields produced by a fractal antenna composed of small line elements and for the calculation of the array factor in the far field of the fractal.

Fractals are characterized by their dimension. It is the key structural parameter describing the fractal and is defined by partitioning the volume where the fractal lies into boxes of side ε. We hope that over a few decades in ε, the number of boxes that contain at least one of the discharge elements will scale as $N(\varepsilon) \sim \varepsilon^{-D}$. It is easy to verify that a point will have $D = 0$, a line will have $D = 1$ and a compact surface will have $D = 2$. The box counting dimension

[*Ott*, 1993] is then defined by

$$D \simeq \frac{\ln N(\varepsilon)}{\ln(\frac{1}{\varepsilon})} \tag{2.1}$$

For a real discharge there is only a finite range over which the above scaling law will apply. If ε is too small, then the elements of the discharge will look like one-dimensional line elements. Similarly, if ε is too large, then the discharge will appear as a single point. It is, therefore, important to compute D only in the scaling range, which is hopefully over a few decades in ε. The fractal dimension will be an important parametrization for the fractal discharge models that we will explore later, and will impact significantly the intensity and spatial structure of the radiated pattern.

We consider a fractal antenna as a non uniform distribution of radiating elements (Fig. 2.1). Each of the elements contributes to the total radiated power density at a given point with a vectorial amplitude and phase, i.e.

$$\mathbf{E} \cdot \mathbf{E}^* \sim (\sum_{n=1}^{N} \mathbf{A}_n e^{i\phi_n}) \cdot (\sum_{m=1}^{N} \mathbf{A}_n e^{i\phi_m})^* = \sum_{n,m} (\mathbf{A}_n \cdot \mathbf{A}_m^*) e^{i(\phi_n - \phi_m)} \tag{2.2}$$

The vector amplitudes $\mathbf{A}_n$ represent the strength and orientation of each of the individual elements, while the phases ϕ_n are in general related to the spatial distribution of the individual elements over the fractal, e.g. for an oscillating current of the form $e^{i\omega t}$ the phases vary as $\phi \sim kr$ where $k = \frac{\omega}{c}$ and r is the position of the element in the fractal.

In the sense of statistical optics, we can consider the ensemble average of Eq. (2.2), using an ergodic principle, over the spatial distribution $P(\phi_1, \phi_2, \phi_3, ..., \mathbf{A}_1, \mathbf{A}_2, \mathbf{A}_3, ...)$ of the fractal elements [*Goodman*, 1985]. For simplicity we assume that the distributions for each of the elements are independent, and also the same, hence

$$G = \sum_{n,m}^{N} \left\langle (\mathbf{A}_n \cdot \mathbf{A}_m^*) e^{i(\phi_n - \phi_m)} \right\rangle = N^2 \left(\frac{\left\langle |\mathbf{A}|^2 \right\rangle}{N} + \frac{N-1}{N} \left| \langle \mathbf{A} \rangle \right|^2 \left| \left\langle e^{i\phi} \right\rangle \right|^2 \right)$$

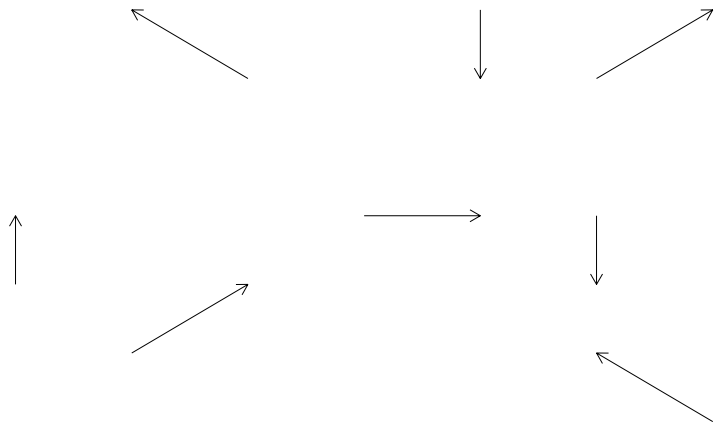

Figure 2.1: A spatially nonuniform distribution of radiators, each contributiong to the total radiation field with a given phase.

By requiring that $\left\langle |\mathbf{A}|^2 \right\rangle = |\langle \mathbf{A} \rangle|^2 = 1$ we obtain that the ensemble average is

$$\langle \mathbf{E} \cdot \mathbf{E}^* \rangle \sim G = N^2 (\frac{1}{N} + \frac{N-1}{N} \left| \left\langle e^{i\phi} \right\rangle \right|^2)$$

If the distribution of the phases is uniform (e.g. random) then $< e^{i\phi} >= 0$ and $G = 1/N$. On the other hand, if there is perfect coherence we have $< e^{i\phi} >= 1$ and $G = 1$. In general, a fractal antenna will display a power law distribution in the phases $P_\alpha(\phi) \sim \phi^{-\alpha}$ (multiplied by the factor $1 - e^{-\phi^{-\alpha}}$ so it is finite at the origin), where $\alpha = 0$ corresponds to the uniform distribution case and $\alpha \to \infty$ corresponds to perfect coherence. Figure 2.2 shows the plot of $\left| \left\langle e^{i\phi} \right\rangle \right|$ as a function of α. It can be seen that a power law distribution of phases, or similarly a power law in the spatial structure, gives rise to partial coherence.

If the distribution of the vector amplitudes does not satisfy the above relations, e.g. the radiators are oriented in arbitrary directions, then the power

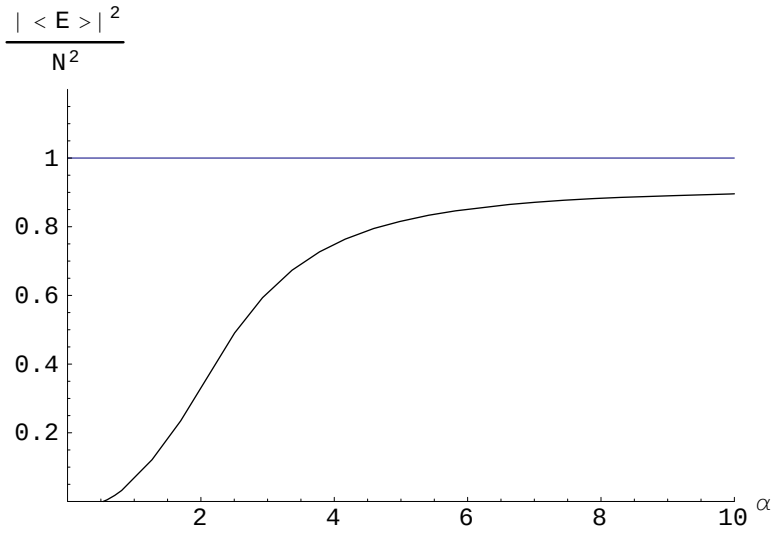

Figure 2.2: A plot of $\left|\left\langle e^{i\phi}\right\rangle\right|^2$ as a function of α.

density will be less coherent due to $\left\langle|\mathbf{A}|^2\right\rangle \geq |\langle\mathbf{A}\rangle|^2$. A similar result can be achieved by having a power law distribution in the amplitudes. In conclusion, the radiation field from a power law distribution of phases will have a point where the phases from the radiators will add up almost (partially) coherently showing a significant gain over a random distribution of phases. Hence the concept of a fractal antenna.

The partial coherence of the radiators depends on the spatial power law distribution. Such a power law distribution of phases can be visualized with the help of Cantor sets [*Ott*, 1993]. A family of Cantor sets is constructed by successively removing the middle $\eta < 1$ fraction from an interval, taken as [0,1], and repeating the procedure to the remaining intervals (see Fig. 2.3). At the n^{th} step, a radiator is placed at the mid-point of each of the remaining intervals.

Note that for $\eta = 0$ we obtain a uniform distribution of elements, but for $\eta \neq 0$ the radiators are non-uniformly distributed, and in fact the spatial distribution follows a power law that can be described by its fractal dimension. Suppose that

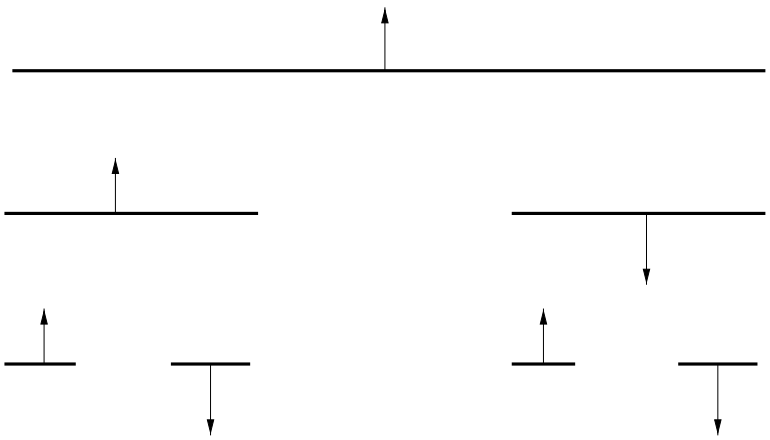

Figure 2.3: The construction of the fractal distribution of the radiators from the $\eta-$Cantor set.

for ε we require $N(\varepsilon)$ intervals to cover the fractal, then it is clear that with $\varepsilon^{'} \rightarrow \frac{\varepsilon}{2}(1-\eta)$ we would require $2N(\varepsilon^{'})$ intervals to cover the fractal. But the fractal is the same, therefore, $N(\varepsilon) = 2N(\varepsilon^{'})$. From the scaling $N(\varepsilon) \sim \varepsilon^{-D}$ we obtain that the dimension is given by

$$D = -\frac{\ln 2}{\ln(\frac{1-\eta}{2})}$$

We can go further, and write a formula for the radiation field due to the $\eta-$Cantor set of radiators. Note that if at the n^{th} step we have the radiators placed at the sequence of points $S_n = \{x_i | i = 1, ..., 2^{n-1}\}$ then at the n^{th}+1 step each radiator at x_i will be replaced by two radiators at $x_i \pm \frac{1}{2^{n+1}}(1-\eta)^{n-1}(1+\eta)$ generating the sequence $S_{n+1} = \{x_i | i = 1, ..., 2^n\}$. Since we start with $S_1 = \{\frac{1}{2}\}$ the sequences S_n at the n^{th} step are trivially constructed. The radiation field (see Eq. (2.1)) from this $\eta-$Cantor set at the n^{th} step can then be written as

$$E = \sum_{m=1}^{n} (-1)^m \mu_m e^{ikLa\ x_m + i\phi_m} \tag{2.3}$$

where $k = \frac{\omega}{c}$, L is the spatial extent of the fractal, $a = \hat{\mathbf{x}} \cdot \hat{\mathbf{r}}$ is the angular position of the detector, and ϕ_m (taken as zero) is the phase of the mth element. The radiators are given a strength proportional to the measure μ_i (or length) of the segment which defines it.

The space dependence of the radiation fields is plotted in Fig. (2.4)a-b for $\eta = 1/3$ ($D = 0.63$) and $\eta = 0$ ($D = 1$) respectively, where the sets have been taken to the 5^{th} level. The most relevant issue for our purposes is the fact that there is a direction at which phases add coherently (partially) for $\eta = 1/3$ while this does not happen for the homogeneous case $\eta = 0$.

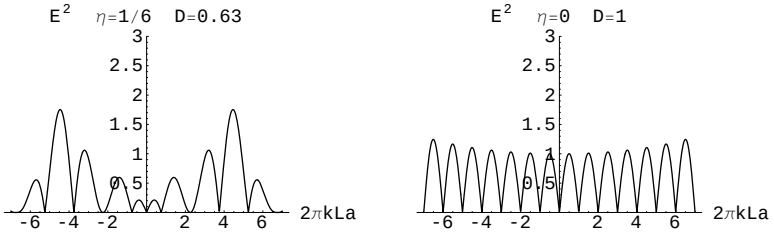

Figure 2.4: The spatial dependence of the radiation fields for (a) $\eta = 1/3$, $D = 0.63$ and (b) $\eta = 0$, $D = 1$.

Therefore, partial coherence occurs naturally in systems that have power-law spatial distributions. We are now ready to turn to the properties of fractal antennae with propagating currents. Specifically, how tortuosity and branching can increase the radiated field intensity in some locations as compared with single dipole antennae.

2.2 Radiation and Simple Fractal Models

To illustrate the properties of fractal antennae compared to those of simple dipole radiators, we take the fractal antenna as composed of small line elements and

compute its far field radiation pattern. For an oscillating current $I(t) = I_o e^{-i\omega t}$ that propagates with speed β =v/c along the antenna, the contribution from each line element to the total radiation field is (from Eq. (2.1))

$$\frac{cr\mathbf{E}_n(\mathbf{r},t)}{I_o} = e^{-i\omega t}e^{ikr}\frac{\beta\hat{\mathbf{L}}_n}{(1-\beta a_n)}e^{ikp_n b_n}e^{i\frac{ks_n}{\beta}}(e^{ikL_n a_n}e^{i\frac{kL_n}{\beta}}-1) \qquad (2.4)$$

where $a_n = \hat{\mathbf{L}}_n \cdot \hat{\mathbf{r}}$, $\mathbf{p}_n$ is the position of the beginning of the line element from the origin, and $b_n = \hat{\mathbf{p}}_n \cdot \hat{\mathbf{r}}$. Radiation occurs when there is a change in the direction of the propagating current. Also note that mathematically we can describe a radiator with a nonpropagating current in the non-physical limit $\beta \to \infty$.

In general, the radiation pattern of an antenna can be effectively excited, only by certain frequencies corresponding to the characteristic length scales of the antenna, e.g. $kL \sim 1$ (see Eq. (2.4)). Therefore, if there is no characteristic size, as in the case of a power law structure, then the antenna will generate an effective radiation pattern for a whole range of frequencies controlled by the smaller and largest spatial scale. Such antenna is called a broad band antenna, and that is why fractal antennae are so important in many applications.

By spatially superposing these line radiators we can study the properties of simple fractal antennae. Of special interest, to our high altitude lightning work, is to compare the radiation pattern of these fractal models with a simple (meaning one line element) dipole antenna.

2.2.1 Gain Due to Tortuosity

The first element in understanding fractal antennae is the concept of tortuosity in which the path length between two points is increased by requiring that the small line elements are no longer colinear. A simple tortuous model is displayed

in Fig. 2.5, where the parameter ε represents the variation from the simple dipole model (line radiator), i.e. the dipole is recovered as $\varepsilon \to 0$.

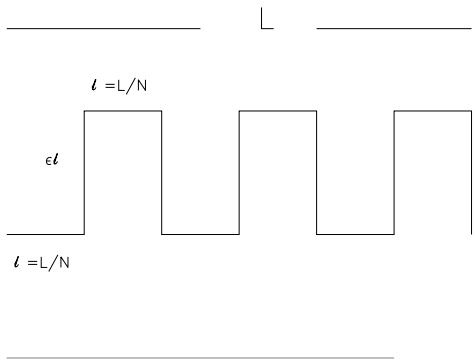

Figure 2.5: A simple tortuous variation of a line radiator. Note that the antenna will radiate every time there is a change in direction.

Except for the propagation effect, we can observe that this antenna (Fig. 2.5) can be considered as the contribution from a long line element (a dipole) plus the contribution from a Cantor set of radiators as described in the previous section (see Eq. (2.3)). Therefore, the tortuosity naturally increases the radiation field intensity, at least in some direction, as compared with the single dipole element.

The field can be written for the structure of 2.5, with the help of Eq. (2.4), as the superposition of the 2N line elements, and is given by the normalized field

$$\mathbf{E}(\varepsilon) = \frac{\beta(e^{ikla_x}e^{i\frac{kl}{\beta}} - 1)}{(1-\beta a_x)}\hat{\mathbf{x}} + \frac{\beta e^{ikla_x}e^{i\frac{kl}{\beta}}(e^{ik\varepsilon a_y}e^{i\frac{\varepsilon kl}{\beta}} - 1)}{(1-\beta a_y)}\hat{\mathbf{y}} + \ldots \qquad (2.5)$$

where $l = \frac{L}{N}$ is the length of the small segments composing the tortuous path, and $a_x = \hat{\mathbf{x}}\cdot\hat{\mathbf{r}}$ and $a_y = \hat{\mathbf{y}}\cdot\hat{\mathbf{r}}$. It is clear that in the limit $\varepsilon \to 0$ we recover the single dipole radiation pattern. The effect of the tortuosity can now be posed as the

behavior of the normalized $P(\varepsilon) = \mathbf{E}(\varepsilon) \cdot \mathbf{E}^*(\varepsilon)$ for $\varepsilon \neq 0$. In general the analysis can be simplified in the limit for small ε, i.e. $P(\varepsilon) \simeq P(0) + P'(0)\varepsilon + \ldots$. Of course $P(0)$ is the dipole contribution, and $P'(0)\varepsilon$ is the change in the radiated power density due to tortuosity. The dipole has a maximum in the radiated power density $P(0) \simeq \frac{4\beta^2}{(1-\beta a_x)^2}$, while the tortuous contribution goes as $P'(0)\varepsilon \simeq \frac{4\beta kL\varepsilon}{(1-\beta a_x)^2} f(a_x, a_y, kL, \beta, N)$. The function f depends on the given parameters, but its maximum is of the order $f \sim 1$ with clear regions in (a_x, a_y) where it is positive.

For our purposes, the most important contribution comes from the fact that $P'(0)\varepsilon$ is essentially independent of N and it scales as $\Delta P \sim \beta k \Delta s = \beta k L \varepsilon$, which corresponds to the increase in the path length of the antenna due to the tortuosity. Such technique can be applied to other geometries, giving essentially the same scaling $\Delta P \sim \beta k \Delta s$ result. This fact will be extremely relevant in our analysis since lightning has naturally a tortuous path.

2.2.2 Fractal Tortuous Walk

More generally, a fractal tortuous path can also be constructed in terms of a random walk between two endpoints [*Vecchi, et al.*, 1994]. We start with a straight line of length L, to which the midpoint is displaced using a Gaussian random generator with zero average and deviation σ (usually $\sigma = 0.5L_i$). The procedure is then repeated to each of the straight segments N times. There is a clear repetition in successive halving of the structure as we go to smaller scales, making this antenna broad band. Figure 2.6a shows a typical tortuous fractal where the division has been taken to the N=8 level and in which the pathlength s has increased 5 times, i.e. $s = 5L$. We can estimate the fractal dimension by

realizing that the total length should go as $L_{tot} \sim L(\frac{s}{\langle \ell \rangle})^{D-1}$, where $\langle \ell \rangle$ is the average segment size. This formulation is completely equivalent to Eq. (2.1).

We let an oscillating current, e.g. $I_o e^{i\omega t}$, propagate along the fractal, but in real applications we can imagine the oscillating current lasting for only a finite time $1/\alpha$. In order to have a finite current pulse propagating through the fractal random walk, we let $I(t) = I_o(e^{-\alpha t} - e^{-\gamma t})(1 + \cos(\omega t))\theta(t)$ with $\omega = 2\pi\alpha n_f$ and $\theta(t)$ as the step function. Here n_f represent the number of oscillations during the decay time scale $1/\alpha$. We chose the decay parameters as $\alpha = 10^3$ s^{-1} and $\gamma = 2 \times 10^5$ s^{-1}, hence $\gamma/\alpha = 200$, which correspond to realistic parameters for lightning [*Uman*, 1987]. The radiated power density is then computed using Eq. (A.4) and is shown in Fig. 2.6b for $\mathrm{n}_f = 5$ and $\beta = 0.1$ at the position $\mathrm{a}_x = 0$, $\mathrm{a}_y = 0$, $r = 60$ km. The dipole equivalent is given by the dashed lines in all 3 panels. The peak in the radiated power density is about 10 times larger than for the dipole case, which agrees well with the results $\frac{\mathrm{P}'(0)\varepsilon}{\mathrm{P}(0)} \sim \frac{2\pi\alpha\Delta s}{c\beta}\mathrm{n}_f \sim 10$ even though the effect from the tortuosity is not small. The larger path length of the tortuous discharge produces an increase in the radiation as compared with a dipole radiator. Of course there is a limit due to energy conservation, but in practical applications we are well under it. The increase in the high frequency components of the radiated field power spectrum (Fig. 2.6c), as compared with the dipole antenna, will be responsible for the spatially structured radiation pattern.

The far field array factor $R = \alpha \int dt \mathbf{E}^2$ (defined in Appendix A) and the peak power density depend on the path length, or equivalently on the number N of divisions of the fractal. Figure 2.7b shows the array factor as a function of the path length for the fractal shown in Fig. 2.7a. Here $\mathrm{n}_f = 5$ so that the peak of

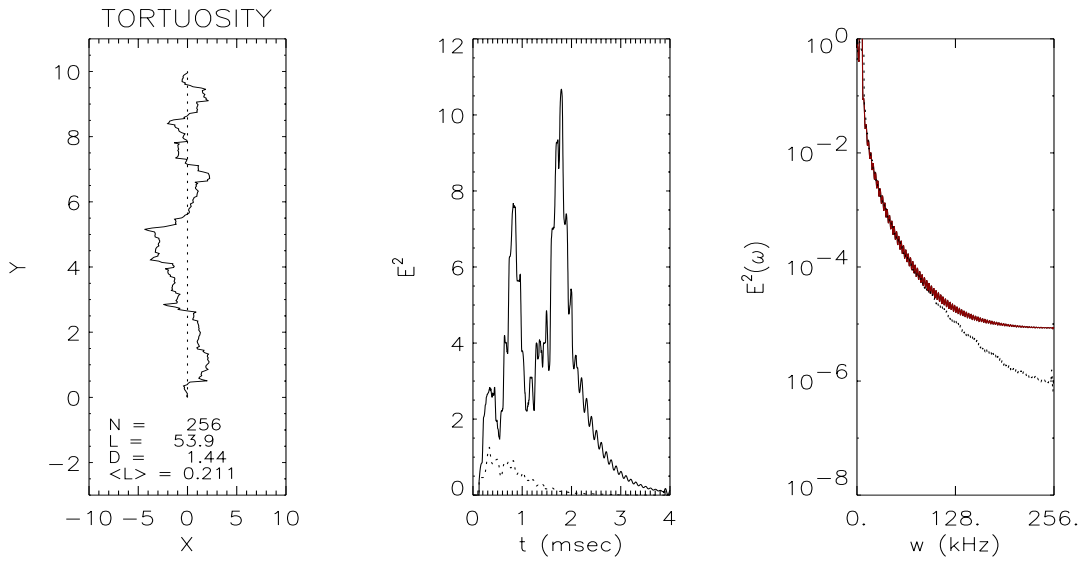

Figure 2.6: The fractal random walk (a) and its instantaneous radiated power density (b) as well as its power spectrum (c). The dashed lines represent the behavior of the single dipole.

the array factor is at $a_x = 0$ and $a_y = 0$. There is a clear increase in the array factor from the tortuous fractal as compared with the single dipole.

Therefore, the effect of tortuosity can increase the radiated power density at certain locations as compared to a single dipole antenna.

Another important concept related to fractal antennae is the spatial structure of the radiation field. We can see from the array factor, Eq. (A.5), that for large n_f $f[\tau, \zeta] \simeq e^{-\tau}(2 + \cos(\zeta\tau))$. The spatial dependence of the array factor will be determined by the factor $\frac{\alpha\zeta\Delta r}{c}$ over the fractal. Consequently, the radiation pattern will have spatial structure when $\frac{\alpha\zeta\Delta r}{c} > 2\pi$, which translate into $n_f > 50$. Figure 2.8b shows the array factor at the height $h = 60$ km for the discharge structure shown in Fig. 2.8a with $n_f = 200$. Therefore, such a tortuous fractal can also display a spatial structure in the radiation pattern. But it is more

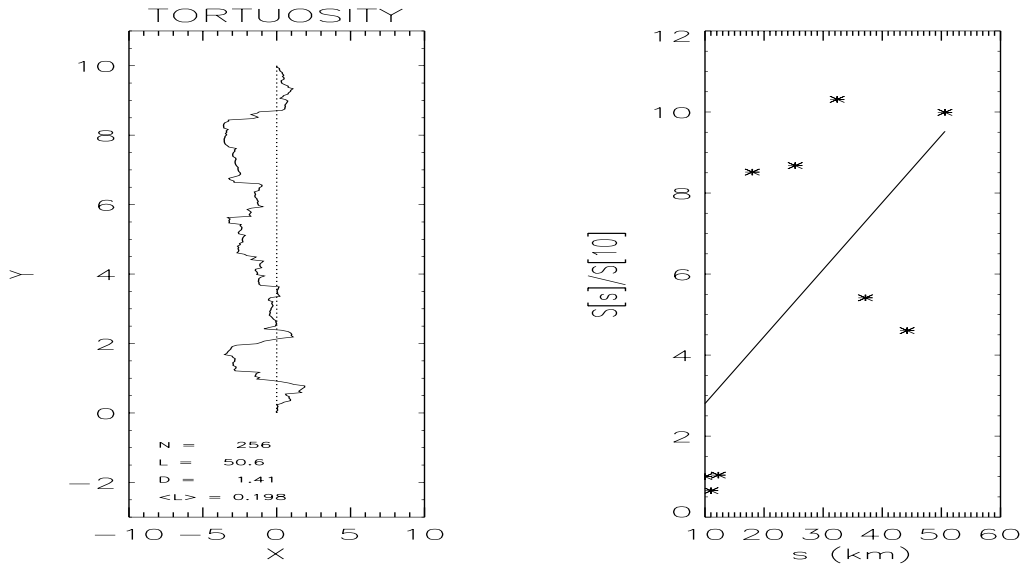

Figure 2.7: (a) The tortuous discharge. (b) The array factor dependence, normalized to the dipole, on the pathlength.

natural for the spatial structure to be generated through a branching process as we will see in the next section.

There is an energy constraint that limits the degree of tortuosity of a fractal lightning discharge since we cannot radiate more energy than what is initially stored as separated charge. Also, if the line elements of the antenna given by Fig. 2.5 get too close together, then their contribution to the radiated field will tend to cancel each other. Therefore, there is an optimal number of elements forming an antenna, and this optimal number translates into an optimal dimension of the fractal, more on this later.

2.2.3 Branching and Spatial Structure

Another element in understanding fractal antennae is the concept of branching. Take the simple branching element shown in Fig. 2.9 where the current is divided

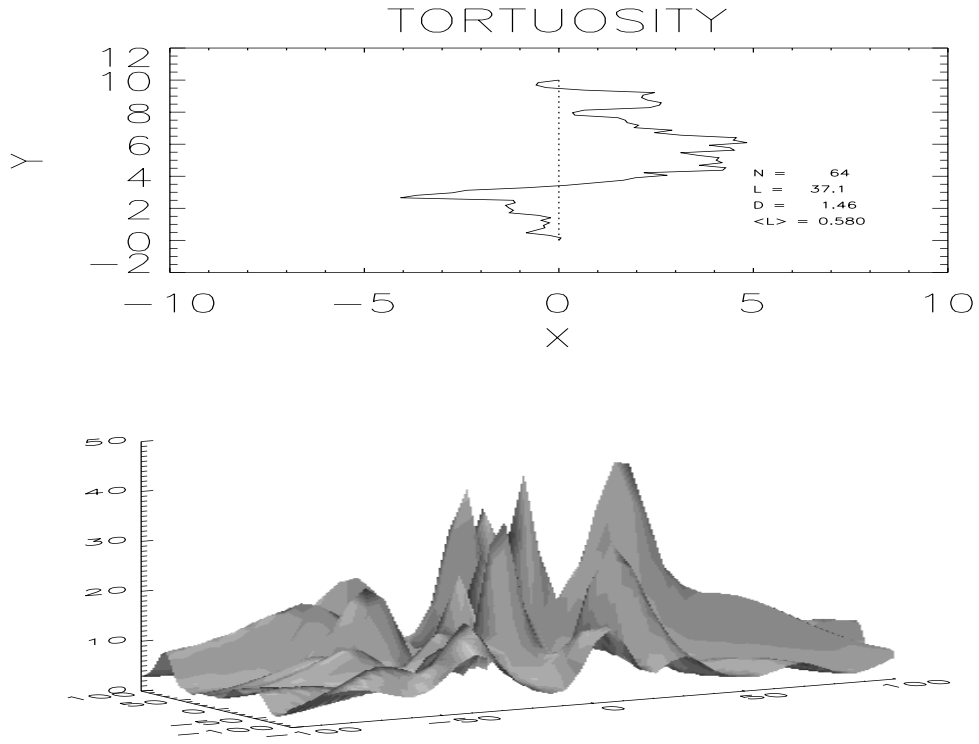

Figure 2.8: The fractal structure (a) and its array factor(b) showing clear spatial structure in the radiation pattern.

between the two branching elements. We can compute the radiation field, for a propagating current $\mathrm{I}_o e^{i\omega t}$, as

$$\mathbf{E}(\varepsilon) = \hat{\mathbf{x}}\frac{\beta(e^{ik\ell a_x}e^{i\frac{k\ell}{\beta}}-1)}{(1-\beta a_x)}+\hat{\mathbf{y}}\frac{\beta e^{ik\ell a_x}e^{i\frac{k\ell}{\beta}}}{(1-\beta a_y)}\frac{1}{2}\{(e^{ik\ell\varepsilon a_y}e^{i\frac{\varepsilon k\ell}{\beta}}-1)-(e^{-ik\ell\varepsilon a_y}e^{i\frac{\varepsilon k\ell}{\beta}}-1)\}\ldots \tag{2.6}$$

where $\ell = L/2$ and ε is the variation from the single dipole, i.e. we recover the dipole as $\varepsilon \to 0$.

Again, the analysis can be simplified in the limit for small ε, i.e. $\mathrm{P}(\varepsilon) \simeq \mathrm{P}(0) + \mathrm{P}'(0)\varepsilon + \ldots$. Of course $\mathrm{P}(0)$ is the dipole contribution, and $\mathrm{P}'(0)\varepsilon$ is the change in the radiated power density due to the line branching. The dipole has a maximum in the radiated power density $\mathrm{P}(0) \simeq \frac{4\beta^2}{(1-\beta a_x)^2}$, while the branching

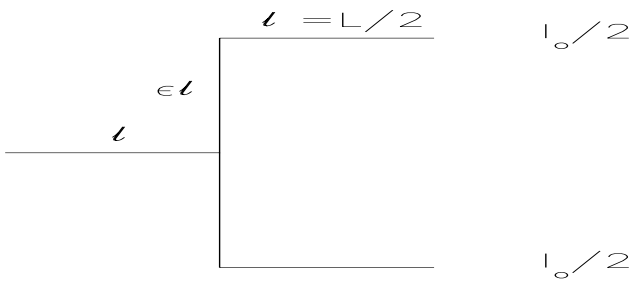

Figure 2.9: A simple branching situation in which we distribute the current among the branching elements.

contribution goes as $\mathrm{P}'(0)\varepsilon \simeq \frac{\beta k L \varepsilon}{(1-\beta a_x)^2}\mathrm{f}(a_x, a_y, kL, \beta, N)$. The function f depends on the given parameters, but its maximum is of the order $\mathrm{f} \sim 1$ with clear regions in (a_x, a_y) where it is positive. Therefore, the branching process can give rise to an increase in the radiated power density at certain position. Of course this increase is due to the increase in the path length. This effect will saturate as ε is increased passed one, since then the strongest contribution will come from the dipole radiator given by $2\varepsilon L$.

A interesting and manageable broadband antenna can be described in terms of the Weierstrass functions [*Werner and Werner*, 1995]. We take successive branching elements, as shown in Fig. 2.10a, where we distribute the current at each branching point so that the branching element keeps a fraction α of the current. The n^{th} branching element is displaced by a factor ε^n with respect to the origin. If we concentrate only on the contribution from the last branching set, as shown in Fig. 2.10a, we can write the field as

$$\mathrm{E}_x \sim \sum_{n=1}^{N} \varepsilon^{n(d_o-2)} \cos(kl\varepsilon^n a_y + \phi_n(\beta))$$

$$\phi_n(\beta) = \frac{kl}{\beta}\varepsilon^{n-1}(2+\varepsilon)$$

where we have redefined $\alpha = \varepsilon^{d_o-2}$ and $a_y = \cos\theta$. In the limit $\beta \to \infty$ and N$\to \infty$ we obtain the Weierstrass function that is continuous but not differentiable, i.e. is a fractal, and furthermore, its dimension in the sense given by Eq. (2.1) is d_o. For the purpose of illustration we truncate the above sum to $N = 8$. In Fig. 2.10b, we show the dependence of the field as a function of $a_y \ \epsilon \ [-1, 1]$ with $a_x = 0$ for $\beta \to \infty$. The parameters values are shown in the figure caption. Figure 2.10c shows the gain factor given by

$$G = \frac{\max |E|^2}{\frac{1}{2}\int da_y \, |E|^2}$$

as a function of the dimension $d_o \ \epsilon \ [0, 1]$. We chose this range since the fractal already has a dimension 1 in the perpendicular directions, i.e. D=1+d_o.

Note the increase in the gain as a function of dimension. In general, there is an optimal value of D that generates the highest power density and that does not necessarily has to be for $D = 2$. In Fig. 2.10b all the elements from the antenna add up coherently at $a_y = 0$, hence providing perfect coherence. For a finite $\beta < 1$ the propagation brings a different phase shift at each element. Figure 2.10d shows the effect for $\beta = 0.1$ as a function of θ. Note that at no point there is perfect coherence, but there is clear partial coherence. The peak value of E^2 is actually sensitive to β.

Even though fractal antennae naturally lead to the concept of an increase in the peak radiated power, it also has a second important consequence due to branching. As we have seen in the case of the Wiertrauss function, fractal antennae naturally result in the generation of a spatial structure in the radiated power density. This interplay between the spatial structure and the increase in

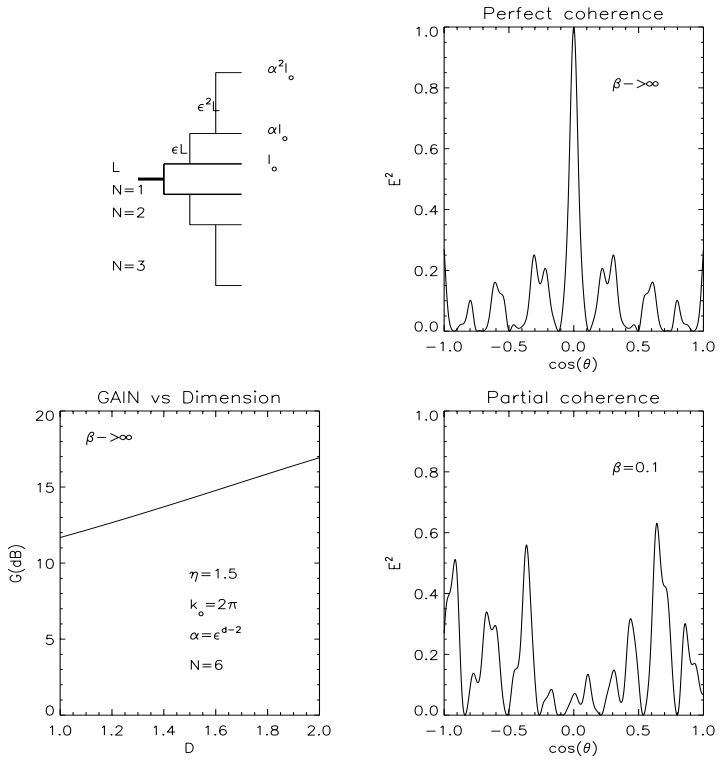

Figure 2.10: The branching process to produce a Weierstrass radiation pattern. (a) The brunching process with the branching length increasing as $\varepsilon^n L$ and the current decreasing as $\alpha^n I_o$. (b) the radiation pattern with $\beta \to \infty$ given perfect coherence. (c) The gain vs the dimension. It also contains the parameters used in all 3 figures. (d) Patial coherence for $\beta = 0.1$.

the peak radiated power are the essential ingredients of fractal antennae and why they are so important. A clear example can be illustrated in Fig. 2.10d where there are multiple relevant peaks of the radiated power in space.

2.3 Modeling Lightning as a Fractal Antenna

The hypothesis of this work is that the structure of the red sprites can be attributed to the fact that the power density generated by lightning does not have the smooth characteristics expected from the dipole model of Eq. 2.7, but the structured form expected from a fractal antenna [*Kim and Jaggard*, 1986; *Werner et al.*, 1995]. Previous studies of lightning assumed that the RF fields causing the atmospheric heating and emissions, were produced by an horizontal dipole cloud discharge moment M that generates an electric field at the height z, given by

$$E = \frac{M}{4\pi\epsilon_o z^3} + \frac{1}{4\pi\epsilon_o c z^2}\frac{dM}{dt} + \frac{1}{4\pi\epsilon_o c^2 z}\frac{d^2M}{dt^2} \tag{2.7}$$

where c is the velocity of light and ϵ_o is the permitivity of free space. It is important to realize that a lightning discharge must be horizontal, as in intracloud lightning, to project the energy upwards into the lower ionosphere. A vertical discharge, as in cloud-to-ground lightning, will radiate its energy horizontally as a vertical antenna.

It is obvious that such a horizontal dipole results in electric fields that vary smoothly with distance. However, it is well known that lightning discharges follow a tortuous path [*LeVine and Meneghini*, 1978]. It was shown [*Williams*, 1988] that intracloud discharges resemble the well known Lichtenberg patterns observed in dielectric breakdown. In fact a time-integrated photograph of a surface leader discharge is illustrated by Figure 2.11 . These patterns have been recently identified as fractal structures of the Diffusion Limited Aggregate (DLA) type with a fractal dimension $D \approx 1.6$ [*Sander*, 1986; *Niemeyer et al.*, 1984].

As noted previously, the tortuous path increase the effective dipole moment,

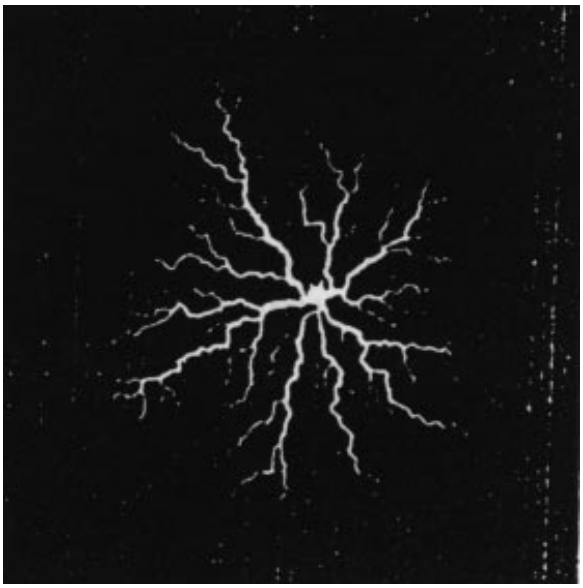

Figure 2.11: Time-integrated photograph of a surface leader discharge (Lichtenberg pattern) [Niemeyer et al., 1984]

since now the pathlength along the discharge is longer that the Euclidean distance. To understand this analogy, we construct a tortuous walk between two points separated by a distance R as shown in Fig 2.12. Take the tortuous path as N small steps of averaged step length $L_o \ll R$, then the total path length S along the tortuous discharge is

$$S \sim NL_o \sim (\frac{R}{L_o})^{D-1} R$$

where the number of small steps is $N \sim (\frac{R}{L_o})^D$ with D as the box counting dimension [*Ott*, 1993]. As we have seen before, the change in the path length increases the radiated power density as $\mathrm{E}^2 = E_o^2 + \beta k(S - R)$ where $\mathrm{E}_o^2 \sim \beta^2$ Therefore, for $R \sim 10$ km (typical for an intracloud discharge), $L_o \sim 50$ m, $\beta = 0.1$, and $D \sim 1.6$, with obtain $\frac{E^2}{E_o^2} \sim 1 + \frac{kR}{\beta}((\frac{R}{L_o})^{D-1} - 1) \sim 1 + 5f(kHz)$ where f is the frequency of the current.

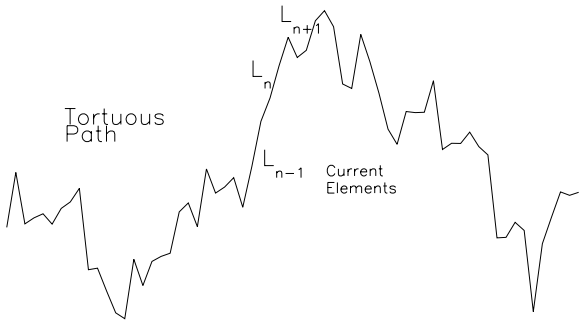

Figure 2.12: Tortuous path between two point.

This is only an analogy, but it gives us good intuition that a fractal lightning discharge will produce an increase in the radiated field intensity, at least locally, as compared with a dipole model and a spatially structured radiation pattern. A fractal dielectric discharge of size R can be modeled as a set of non-uniformly distributed small current line elements [*Niemeyer et al.*, 1984] that represent the steps of the discharge breakdown as it propagates during an intracloud lightning discharge. The size of the elementary current steps is about $L_o \sim 50$ m [*Uman*, 1987]. As a current pulse propagates along this horizontal fractal discharge pattern it radiates energy upwards (see Appendix A on how the fields are calculated) as well as downward.

To determine the extent over which the non-uniformity of the lightning discharge current affects the power density structure projected in the lower ionosphere, we will now construct a simple fractal model of the lightning discharge that will yield a spatio-temporal radiation pattern at the relevant heights.

2.3.1 Fractal Lightning: Stochastic Model

We want to generate a fractal model that can be parametrized by its fractal dimension. For this purpose, we follow *Niemeyer et al.* [1984] who proposed a two dimensional stochastic dielectric discharge model that naturally leads to fractal structures. In this model the fractal dimension D can be easily parametrized by a parameter η. Femia et al. [1993] found experimentally that the propagating stochastic Lichtenberg pattern is approximately an equipotential. Then, the idea is to create a discrete discharge pattern that grows stepwise by adding an adjacent grid point to the discharge pattern generating a new bond. The new grid point, being part of the discharge structure, will have the same potential as the discharge pattern. Such local change will affect the global potential configuration, see Fig. 2.13.

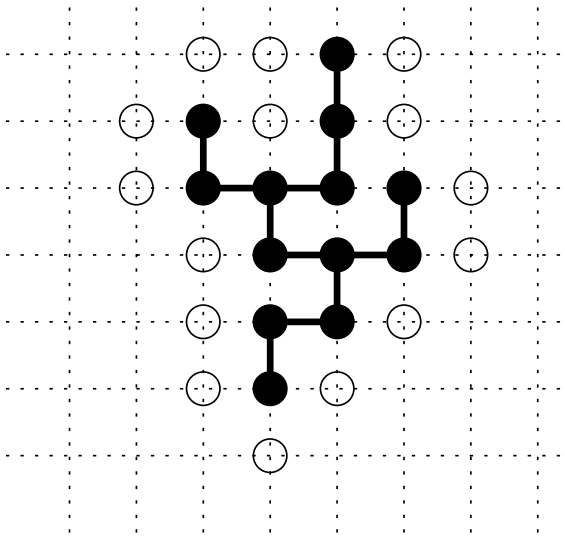

Figure 2.13: Diagram of the discrete discharge model.

The potential for the points not on the discharge structure is calculated by

iterating the discrete two dimensional Laplace's equation

$$\nabla^2\phi = 0$$

$$\phi_{i,j} = \tfrac{1}{4}(\phi_{i+1,j} + \phi_{i-1,j} + \phi_{i,j+1} + \phi_{i,j-1})$$

until it converges. This method reproduces the global influence of a given discharge pattern as it expands. The discharge pattern evolves by adding an adjacent grid point. The main assumption here is that an adjacent grid point denoted by (l,m) has a probability of becoming part of the discharge pattern proportional to the η power of the local electric field, which translates to

$$p(i,j) = \frac{\phi_{i,j}^{\eta}}{\sum_{l,m}\phi_{l,m}^{\eta}}$$

in terms of the local potential. Here we have assumed that the potential at the discharge is zero. The structure generated for $\eta = 1$, corresponding to a Lichtenberg pattern, is shown in Fig. 2.14.

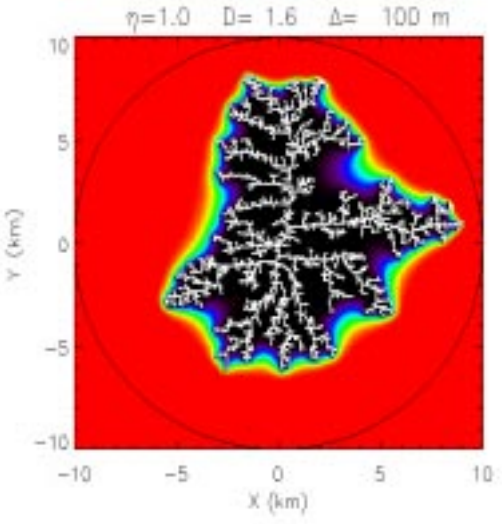

Figure 2.14: Fractal discharge generated with $\eta = 1$.

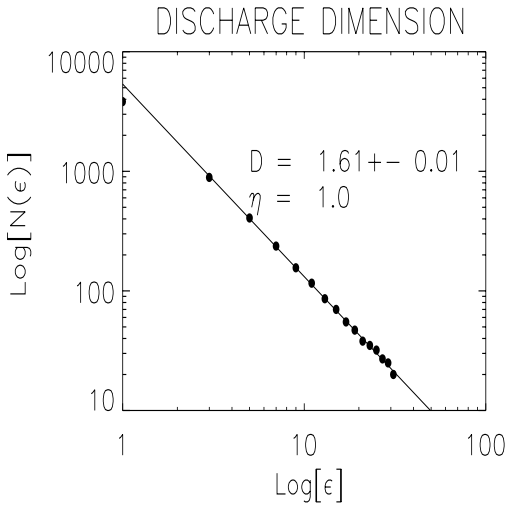

Figure 2.15: The plot of $lnN(\epsilon)$ vs $\frac{1}{\epsilon}$ for $\eta = 1$.

The color coding corresponds to the potential. Figure 2.15 shows a plot of $N(\varepsilon)$ vs. $Log(\varepsilon)$ for the fractal discharge of Fig. 2.14, i.e. $\eta = 1.0$. Again the scaling behavior only occurs over a few decades, but it is very clear. The dimension of this structure is $D \simeq 1.6$.

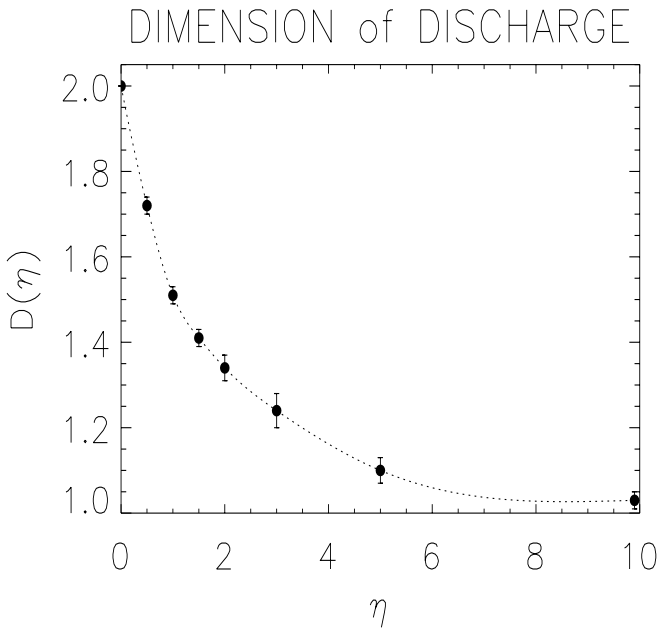

Figure 2.16: The dimension of the stochastic model as a function of η with the estimated error bars.

Note that this model, and also the dimension of the discharge, is parametrized by η. Intuitively we expect that when $\eta = 0$ the discharge will have the same probability of propagating in any direction, therefore, the discharge will be a compact structure with a dimension $D = 2$. If $\eta \to \infty$ then the discharge will go in only one direction, hence $D = 1$. Between these two limits, the dimension will be the function $D(\eta)$ shown in Fig 2.16. As an example the corresponding structure generated for $\eta = 3$ (Fig 2.17) has a dimension of $D = 1.2$.

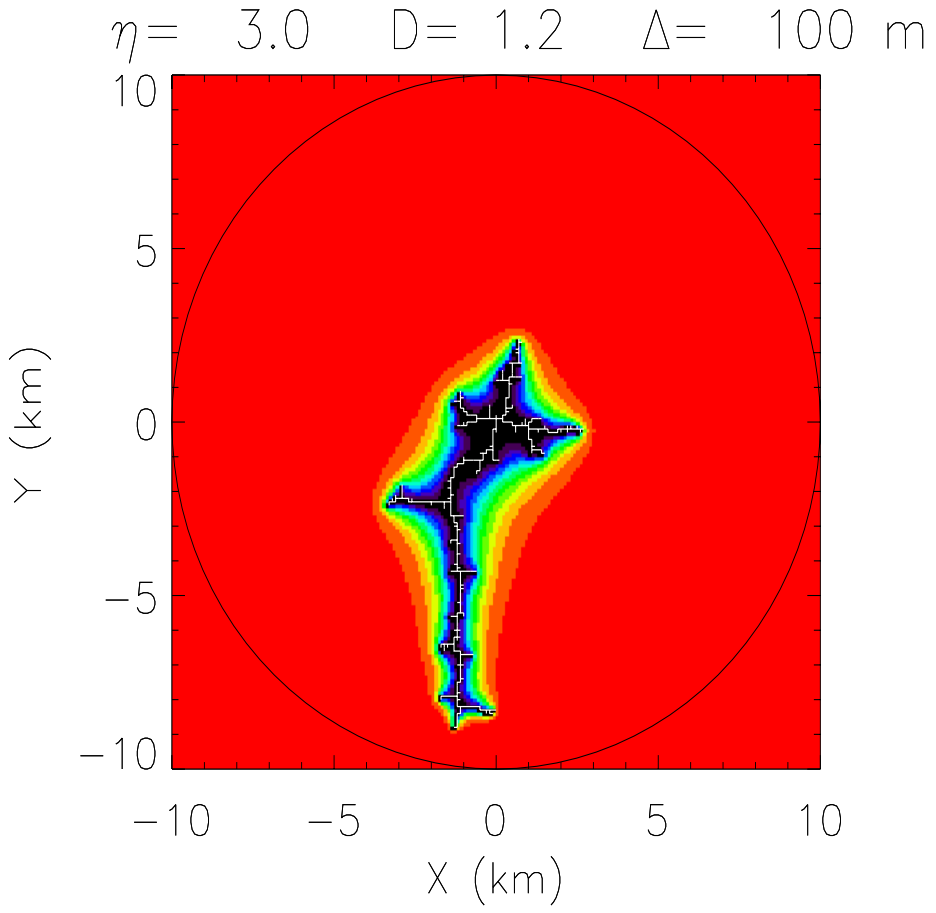

Figure 2.17: Fractal discharge generated for $\eta = 3$.

To compute the radiated fields, we must describe the current along each of the segments of the fractal discharge. We start with a charge Q_o at the center of the discharge. The current is then discharged along each of the dendritic arms. At each branching point we chose to ensure conservation of current, but intuitively we know that a larger fraction of the current will propagate along the longest arm. Suppose that a current I_o arrives at a branching point, and if L_i is the longest distance along the i^{th} branching arm, we intuitively expect that the current on the i^{th} arm should be proportional to L_i^{η}. Therefore, we satisfy

charge (or current) conservation if the current along the i^{th} branching arm is

$$I_i = \frac{L_i^\eta}{\sum_j L_j^\eta}$$

2.3.2 Computing the Fields from the Fractal Structure

A current pulse propagates along the horizontal (in the x-y plane) 2 dimensional fractal discharge structure, e.g. $I(x,t) = I(t - \frac{s}{v})$ generating radiation fields. The radiation field is the superposition, with the respective phases, of the small line current elements. The intracloud current pulse is taken as a series of train pulses that propagate along the arms of the antenna

$$I(t) = I_o(e^{-\alpha t} - e^{-\gamma t})(1 + \cos(\omega t))\theta(t)$$

with $\omega = 2\pi\alpha n_f$ and $\theta(t)$ as the step function. Here n_f represent the number of oscillations during the decay time scale $1/\alpha$. We chose the decay parameters as $\alpha = 10^3$ s^{-1} and $\gamma = 2 \times 10^5$ s^{-1}, hence $\gamma/\alpha = 200$, which correspond to realistic parameters for lightning [*Uman*, 1987]. The total charge discharged is then $Q = I_o/\alpha$, which for $I_o = 100\ kA$ gives $Q \sim 100\ C$. As we have seen before, we require $n_f \sim 100$ to create the spatial structures so that the exponential decay $e^{-\alpha t}$ can be considered as the envelope of the oscillating part.

On a given position the time dependence of the field intensity E^2 has a fractal structure, as it is shown in Fig. 2.18a for the stochastic discharge model with $\eta = 3$. The frequency spectrum of the electric field is shown in Fig. 2.18b. It is very important to realize that the relevant frequencies are below a few hundred kHz. By restricting the field frequencies to below a few hundred kHz, the analysis is greatly simplified, since then the conductivity and dielectric tensors can be considered as independent of time in the lower ionosphere (see Appendix B).

The large conductivity of the ground at these frequencies can be included by assuming to first order an image discharge of opposite current below a perfectly conductive plane. The primary discharge is taken to be at $z_o = 5$ km above the ground. This parameter is not very relevant, since we are interested in the field at heights of about $h \sim 80$ km, therefore, moving the discharge from 5 to 10 km will only change the field strength by a marginal 10%.

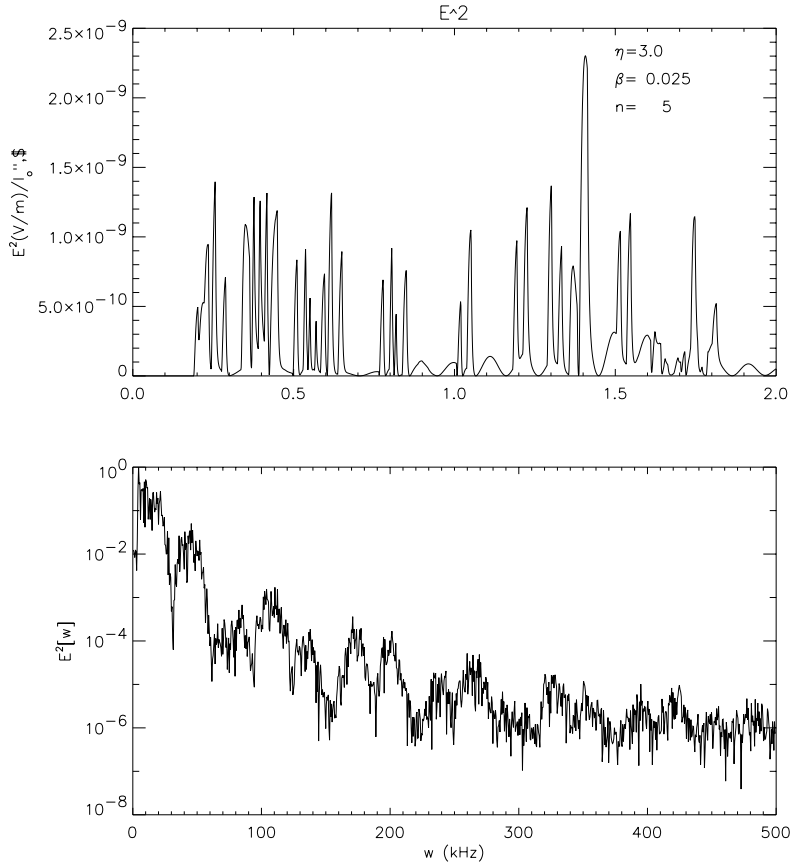

Figure 2.18: (a) The field power density due to the stochastic discharge model at a given position as a function time (b) and the frequency spectrum of the field.

2.3.3 How does the Fractal Dimension Affect the Field Pattern?

For a 2-dimensional fractal structure, we expect that the strength of the radiated power density depends on the fractal structure, i.e. its fractal dimension. If the strength of the k Fourier component is A_k then the field in the far field [*Jackson* 1975] at r along the axis of the fractal will be given by

$$\mathbf{E} \sim \int dk A_k \int_\mu d\mu \mathbf{R}(\mu) \sin(k\rho)$$

where dμ (the fractal measure) is the contribution of the fractal from a given polar position (ρ,ϕ). $\mathbf{R}(\mu)$ is the phase contribution from the elements of the fractal at position (ρ,ϕ) and in the far field should be proportional to the direction of the local current. Note that a radially propagating uniform 2 dimensional current structure will generate no field at the axis since contributions to $\mathbf{R}(\mu)$ from different parts of the fractal will cancel each other.

The cross section of the fractal at a given radius ρ will resemble a Cantor set in $\phi \epsilon [0, 2\pi]$, and the phase contribution will be given by $\mathbf{S}(\rho) = \int_\mu d\phi \mathbf{R}(\rho, \phi)$ which will be finite for an asymmetrical fractal. The integration can be carried as a Lebesgue integral or as a Riemann-Stieltjes integral over this pseudo-Cantor set [*Royden*, 1963]. Note that if the fractal is uniformly distributed along ϕ, corresponding to D=2, then $\mathbf{S}(\rho) = 0$. Similarly, for a delta function at $\phi = \phi_o$ corresponding to D=1, $\mathbf{S}(\rho)$ gives a positive contribution. $\mathbf{S}(\rho)$ is a very complicated function that depends on the details of the current distribution along the fractal. In an average sense we can suppose that $S(\rho) \sim f(D)$ where $f(D = 1) = 1$ and $f(D = 2) = 0$ but f can be greater than one for other values as has been investigated in previous sections when branching and propagation

occurs. Therefore,

$$E \sim f(D) \int dk A_k \int_\mu dm(\rho)\ I(\rho) \sin(k\rho)$$

where dm(ρ) represents the amount of the fractal between ρ and $\rho + d\rho$ and I(ρ) is the averaged current over ϕ at radius ρ. A fractal will have a mass up to a radius ρ given by $m(\rho) = (\frac{\rho}{L_o})^D$ by noting that a 2 dimensional antenna will have more elements than a one dimensional fractal. In general, due to the branching process, some of the current does not reach the radius R. But for simplicity, if all of the current reaches the end of the fractal at radius R, then $dm(\rho)\ I(\rho) = d\rho$. In such case, the above integral gives

$$E \sim f(D) \int dk\ k^{-1} A_k (1 - \cos(kR))$$

Note that $\varepsilon = (\frac{\ell}{R})$ in some sense selects the Fourier component $k = \frac{2\pi\beta}{\varepsilon R}$ which has a strength $A_k \sim N(\varepsilon) \sim \varepsilon^{-D}$. The integral over k gives $g(D) \simeq (\frac{L_o}{R})^{D-1}$, therefore, the field is given by

$$E \sim f(D) g(D) \tag{2.8}$$

which shows that the field has a maximum value at a specific value of $D\ \epsilon\ [1, 2]$ since $f(D)$ decreases and $g(D)$ increases with D respectively.

On the other hand, the Rayleigh length, the distance beyond which the field start decaying to their far field values, behaves as $R_L(\varepsilon) \sim \frac{\varepsilon R}{2\pi\beta}$ for a given ε. Red sprites occur at a height $z \sim 80$ km, therefore, for $z > R_L(\varepsilon)$, elements with sizes smaller than ε do not contribute to the field, i.e. as we increase z we wash out the information of increasingly larger spatial scales of the fractal. It is the power law dependence, as specified by the fractal dimension, that determine the field pattern.

Even though, the radiation pattern will depend on the details of the fractal structure, we expect that the most relevant parameter in determining the radiation pattern will be the fractal dimension, as found by Myers et al. [1990] for simple fractals. There is an interplay between the dimension and the spatial structure of the radiation pattern. For a dimension close to $D \sim 1$or $D \sim 2$, there will be no significant spatial structure. While an intermediate dimension can produce a significant spatial structure.

2.3.4 Fields from the Stochastic Model

First we start by computing the array factor based on the far field approximation (see Appendix A). We take $n_f \sim 200$ and $\beta = 0.1$ and compute the array factor at a height $z = 60$ km. Figure 2.19 shows the array factor for the discharge structure shown in Fig. 2.17 with $\eta = 3$.

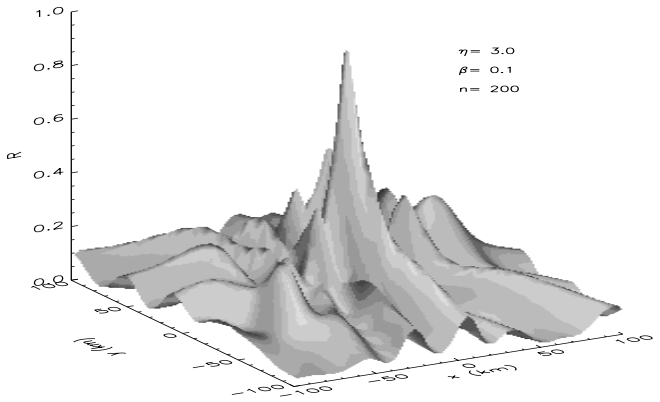

Figure 2.19: The array factor for $\eta = 3$.

The length of the elementary current elements is about 100 m. The array factor shows clear structure. A cross-section of the normalized array factor are

shown in Fig. 2.20 and Fig. 2.21 for $\eta = 1$ and $\eta = 2$ respectively.

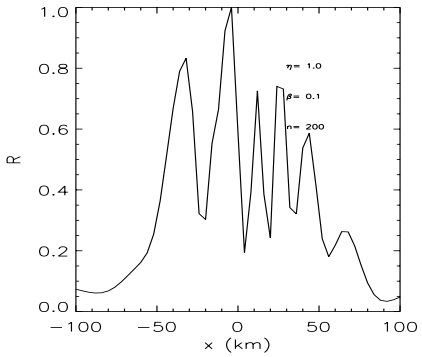

Figure 2.20: Cross-section of the array factor for $\eta = 1$.

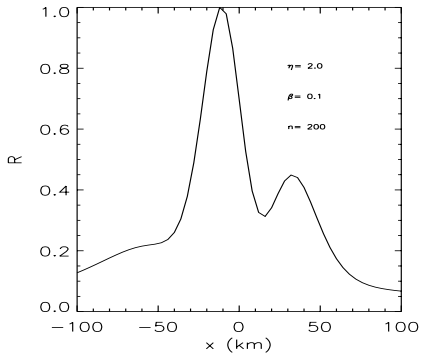

Figure 2.21: Cross-section of the array factor for $\eta = 2$.

Similarly, the array factor at $x = 10$ km, $y = 10$ km, $z = 60$ km is shown as a function of the fractal dimension of the discharges for $\beta = 0.05$ and $\beta = 0.025$ in Fig. 2.22a for $n_f = 0$ and Fig. 2.22b for $n_f = 200$.

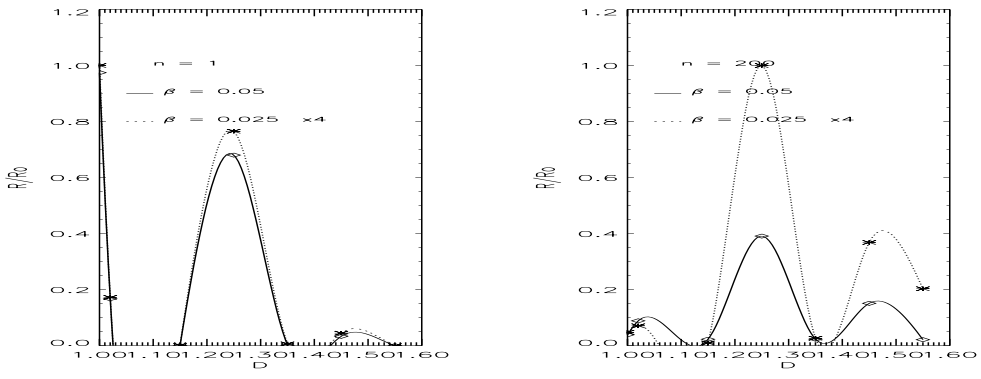

Figure 2.22: The array factor (a) For $n_f = 1$ and (b) for $n_f = 200$. The graph has been interpolated for the purpose of illustration.

The fractal dimension dependence of the array factor is very intriguing, but is of clear significance for our lightning studies. What about the time dependence

of the radiations fields? Figure 2.23 shows the time dependence of the radiation fields for $\eta = 1, 2, 3, 5, 10$ with $n_f = 200, 50, 1$ where each figure is carefully labeled. Again the relevance of the $\eta = 3$ case is very striking. Each column of

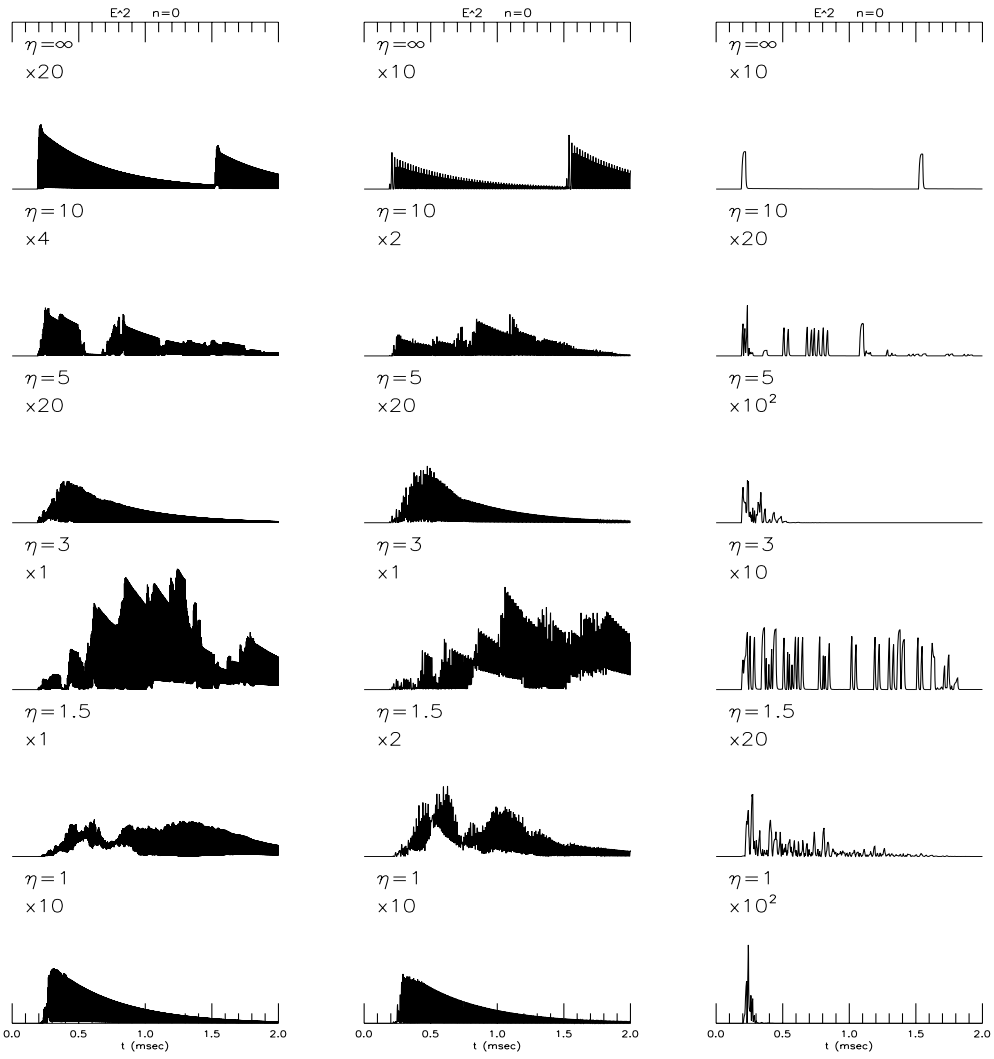

Figure 2.23: The time dependence of the radiation fields for the fractal models. See explanation in text.

graphs represent the time dependence for $n_f = 200, 50, 1$ respectively, where the rows represent the case for $\eta = 1, 2, 3, 5, 10$. The amplitude of the field has been

multiplied by the factor displayed next to the graph.

We take the case for $\eta = 3$ and we study the dependence of the array factor as a function of the current frequency as parametrized by n_f. Figure 2.24 shows the frequency dependence of the array factor at this location $x = 10$ km, $y = 10$ km, $z = 60$ km. Initially the array factor increases linearly with n_f as expected but then it starts to oscillate as the spatial variation of the field pattern becomes relevant.

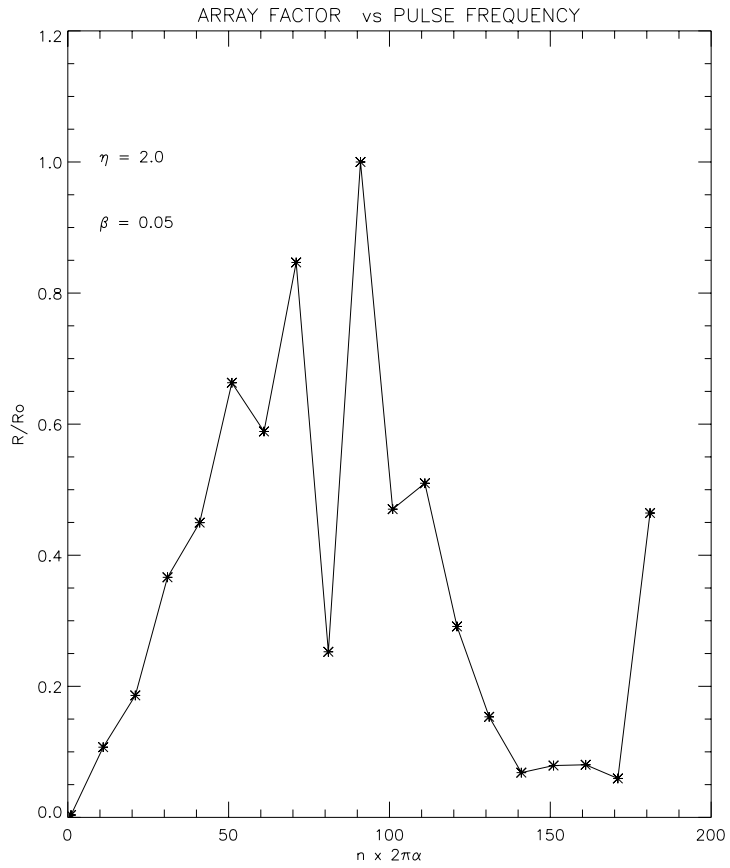

Figure 2.24: The array factor as a function of n_f for $\eta = 3$.

In conclusion, the fractal nature of the discharges, being a simple random walk or a stochastic discharge model, leads naturally to an increase in the peak

power density as compared with the dipole model. This increase is related to the increase in the antenna path length, or tortuosity, and on the branching process. It will be shown later that this gain in peak power density leads to a significant reductions in the discharge properties (e.g. charge, peak current) required to produce the observed sprite emissions. Furthermore, if the discharge has a high frequency component, as expected from an acceleration and deceleration process in each of the single steps, then the radiation pattern can show spatial structure. This spatial structure of the lightning induced radiation pattern will be related to the spatial structure of the red sprites in the next chapter.

Chapter 3

Modeling Red Sprites

3.1 The Model

We now combine the ideas developed in the previous chapters and apply them to the modeling of red sprites. We have seen that the radiation pattern and intensity is critically dependent on the fractal model, e.g. the fractal dimension of the discharge. Therefore, we expect that the lightning parameters required to produce the red sprites are critically dependent on the discharge fractal dimension as well. We will study the current threshold required to produce the sprite for different fractal dimensions.

The modeling of the effects of the fractal lightning discharge on the lower ionosphere involves a series of steps, as it is shown in Fig. 3.1:

- Task 1: Modeling of the fractal lightning discharge and its spatio-temporal current profile as developed in Section 2.3.1. The phase coherence over the extent of the fractal will become extremely relevant. In fact, it will be the self-similarity over the fractal that will produce the spatially structured field profile.

- Task 2: Computation of the electromagnetic field in the lower ionosphere from the spatio-temporal current profile. The computation of the electromagnetic field must consider self-consistently the propagation of the lightning related EMP fields in the lower ionosphere as the field changes the properties of the medium by energizing the electrons and generating highly non-Gaussian distribution functions. The propagation and absorption of the electromagnetic fields is developed in Appendix B. The electron energization in the presence of inelastic losses due to collisions with neutrals is computed with the help of a Fokker-Planck code. The Fokker-Planck formalism is also developed in Appendix B. Once we have such a model we can estimate the radiation pattern from the fractal discharge structure that are projected into the upper atmosphere and lower ionosphere.

- Task 3: Calculation of the intensity of the stimulated high altitude optical emissions, using the spatio-temporal electric field profile. The energized electrons collide with the neutrals inducing excited states which are then followed by emissions. The computation of the optical emissions from $N_2(1P)$ from the field pattern in the lower ionosphere is described in Appendix B. The computed optical emissions can be compared with the observations.

Therefore, the main parameters controlling the model are:

- The fractal structure of the model as represented by its fractal dimension. The fractal dimension should be one of the most relevant parameters controlling the spatio-temporal optical emissions since it controls the strength of the field's Fourier components (as seen before). For simplicity the size

R of the discharge is taken as $R = 10$ km as developed in Chapter 2.

- The current pulse peak and width, hence the total charge discharged. The altitude of the stroke taken as $z_o = 5$ km with its image discharge at $z_o = -5$ km.

- The ambient electron density height profile, generally taken as the tenuous night time profile.

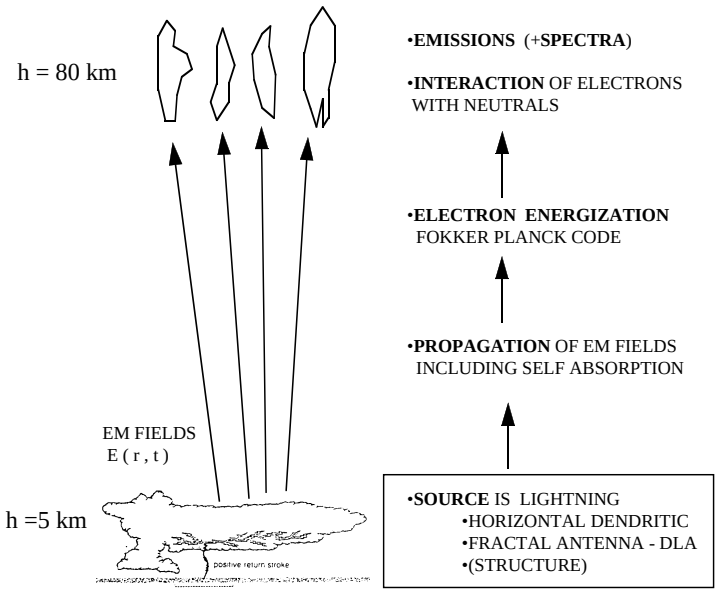

Figure 3.1: A diagram of the tasks involved in the treatment. From the fractal structure, we compute the fields generated and their interaction with the medium in the lower ionosphere

The spatial geometry is defined with z as the height from the ground and x-y as the constant height cross-section. The horizontal fractal lightning discharge is constructed in the x-y plane at a height of $z_o = 5$ km from the ground (with the image discharge at $z_o = -5$ km). The point $x = 0$ km and $y = 0$ km corresponds to the center of the discharge.

3.2 $N_2(1P)$ Emissions from the Stochastic Model

The stochastic fractal model is specially suitable for understanding the dependence on the dimension of the discharge, since $D(\eta)$ can be easily parametrized as is plotted in Fig. 2.16. The spatio-temporal emission pattern from the fractal discharge model can now be computed from the field pattern that includes self-absorption. As an example, we take a discharge current of $I_o = 200$ kA and $\beta = v/c = 0.025$. Since the decay time is $\alpha = 1000$ s^{-1}, the total amount of charge discharged is $Q = 200$ C. The statistical relevance of such values for lightning and the generation of sprites will be discussed latter.

For this case the field is below the ionization threshold in the lower ionosphere. For intensities exceeding the ionization threshold, the time evolution of the electron density must be included.

The fractal dimension for the lightning discharge is $D \sim 1.25$. The instantaneous field amplitude at $z = 85$ km and $x = 0$ km, including self-absorption, is shown in Fig. 3.2a and the instantaneous optical emission of the $N_2(1P)$ in Fig. 3.2b.

To compare the results with the sprite observations, we must average the photon flux over the time scale of sprites. The averaged number of photons per

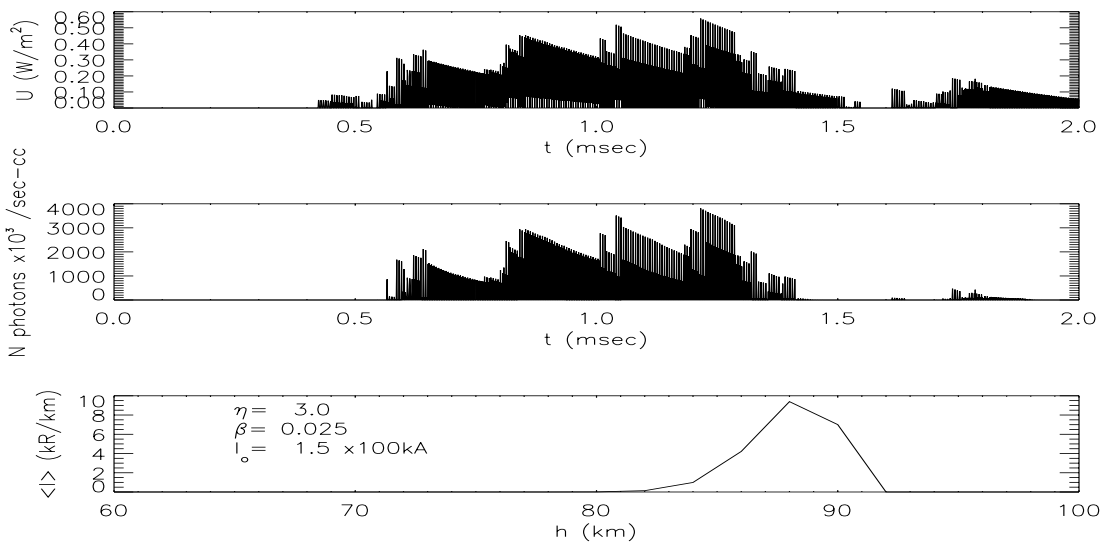

Figure 3.2: (a) The instantaneous field profile with self-absorption included for $\eta = 3$. (b) The instantaneous emissions of the $N_2(1P)$. (c) The number of photons averaged over time as a function of height in units of kR/km.

sec per cm^3 can now be calculated as

$$< N(s^{-1}cm^{-3}) >= \frac{1}{\Delta t}\int_0^{\Delta t} \nu_{ex}^{1p}(E(t))n_e dt \tag{3.1}$$

where n_e is independent of time since we stay below the ionization threshold. The number of photons averaged over time as a function of height is shown in Fig. 3.2c in units of kR/km. The units of kR/km is defined in terms of the detector optical path (column integration), so that, a sprite with a horizontal size of 20 km having an average of 10 kR/km would measure an intensity of $I(kR) \simeq 200$ kR for an optimal detector inclination.

Of course, this value is computed locally at a single point, and we must repeat this procedure in space to deduce the spatial dependence of the emissions. The time averaged emission pattern from the lower ionosphere, for the horizontal

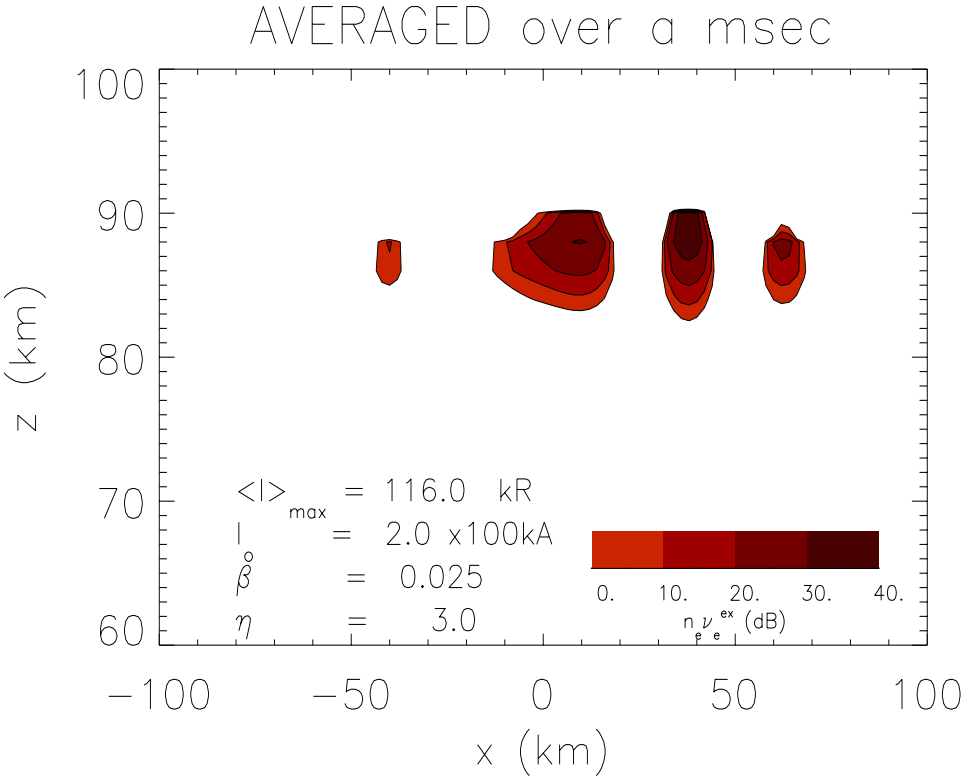

Figure 3.3: The time averaged emission pattern. The temporal emission pattern has been time averaged for about a millisecond (duration of sprite). The column integrated emission intensity was about 30 kR for an optimal optical path.

cross-section along the line $y = 10$ km, is shown in Fig. 3.3 for the discharge current of $I_o = 200$ kA. The color coding represents the number of photons emitted per sec per cc in dBs normalized by its average over the image region. The maximum intensity is about 100 kR for column integration along the x axis. We did check that the field intensities at all times were below the ionization threshold for this current of $I_o = 200$ kA. The fractal nature of the discharge can in fact produce a non-uniform emission pattern.

A plot of the number of emitted photons in units of kR/km as a function of the discharge current I_o is shown in Fig. 3.4 for the position at the core of the

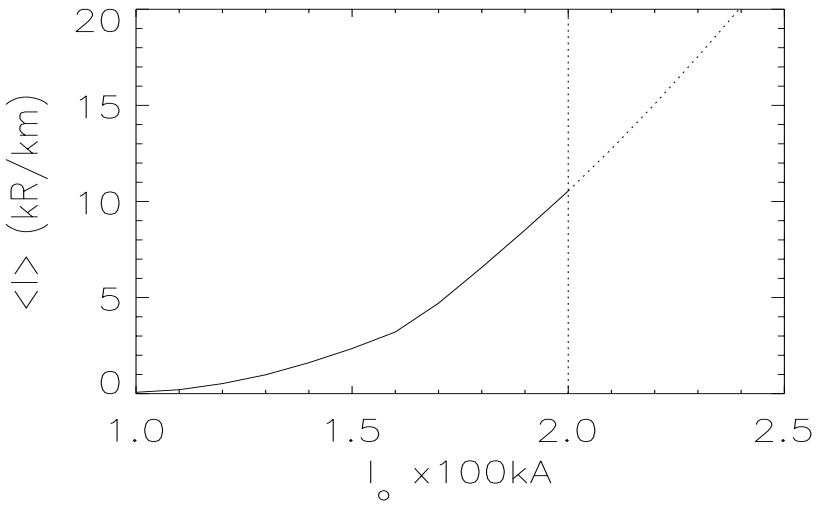

Figure 3.4: The emission intensity for the optimal optical path as a function of the current strength I_o. The ionization theshold occurs at $I_o = 170$ kA.

sprite, i.e. as given for Fig.3.2. If the field becomes larger than the ionization threshold, we must incorporate the time evolution of the electron density. The ionization threshold is reached when $\tilde{\epsilon} \geq 0.1$ eV which for our fractal model with the propagation speed $\beta = 0.025$ occurs at a critical current $I_o \sim 200$ kA. Since the power density scales as $S(W/m^2) \sim I_o^2 \beta^2$, we can use Fig.3.4 as a reference for the requirements of the lightning parameters to generate the sprite. Hence, for a faster discharge a sprite can be produced with a lower current amplitude.

We proceed next to determine the spatial structure of the optical emissions as a function of the dimension D. We consider the 4 fractal discharges $\eta = 1, 2, 3, \infty$ shown in Fig. 3.5 with dimensions $D = 1.55,\ 1.3,\ 1.2,\ 1.0$ respectively, where the thickness of the line corresponds to the strength of the current.

The emission patterns along the cross-section $x = 10$ km, averaged over the duration of the discharge using Eq. (3.1) is shown in the four panels of Fig 3.6.

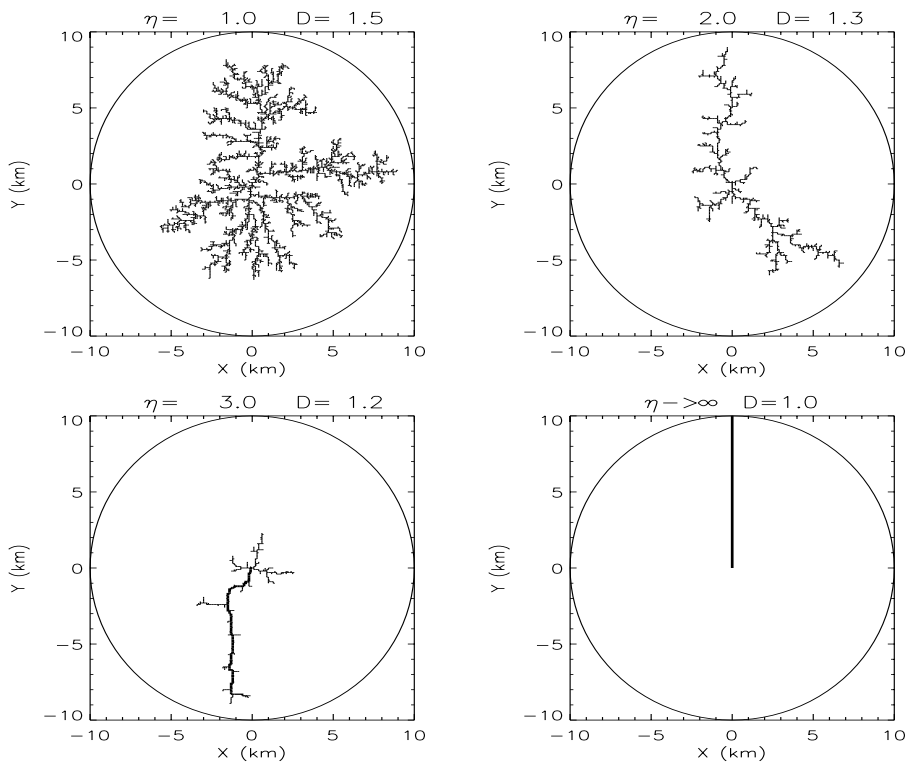

Figure 3.5: The fractal structures for dimensions D= 1.55, 1.3, 1.2, 1.0 ($\eta = 1, 2, 3, \infty$) respectively . The thickness of the lines corresponds to the current strength, and current conservation has been satisfied at each branching point.

The velocity of the discharge was taken as $\beta = 0.025$ and the amount current as $I_o = 200$ kA. The emission rate, e.g. number of photons per cc per second, is computed in dB with respect to the averaged emission rate over the image area.

The maximum intensity in kR for a optimal column integration along the x axis, is shown in Fig. 3.7 as a function of the dimension of the discharge $D(\eta)$. Since the optical emission intensity is extremely sensitive to the power density, a factor of 2 on the electric field strength can have profound effects on the emission pattern of a given fractal discharge. Hence the sensitivity of the optical emission pattern on the dimension of the discharge.

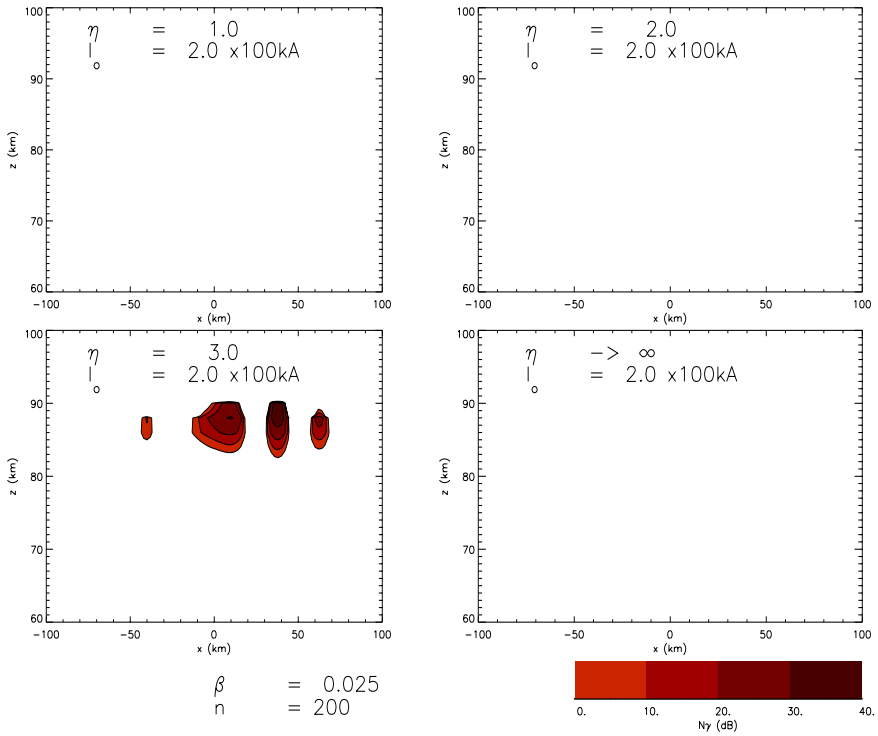

Figure 3.6: The emissions pattern as a function of dimension. $\beta = 0.025$.

As seen in Fig. 3.6 different fractals require different current peaks (or propagation speed) to produce similar emissions intensities. For the 4 fractals of Fig. 3.6 we find the necessary current peak I_o needed to produce an emission intensity of about 100 kR. The corresponding emission patterns are shown in Fig. 3.8 with their peak current I_o. We note that the emission pattern corresponding to the fractal $\eta = 3$ has considerable spatial structure as compared with the other cases in the figure. We see that by having a spatially structured radiation pattern, the fractals can increase the power density locally in specific regions of the ionosphere and generate considerable optical emissions with relatively low (more realistic) lightning discharge parameters.

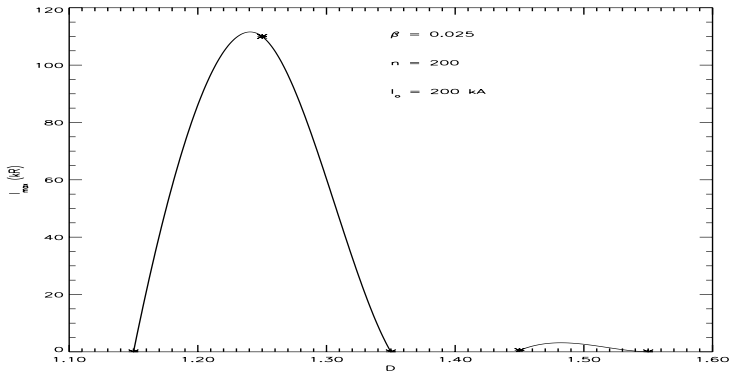

Figure 3.7: The maximum intensity in kR as a function of the dimension. The graph has been interpolated (actual points are shown by asterix *).

3.3 Importance of the Fractal Nature of Lightning

We have generated a novel model of red sprites that relies on the fractal structure of the lightning discharge. Such fractal structure is reflected in the fine structure of the subsequent optical emission pattern. The incorporation of the fractal structure of lightning provides a clear method for the generation of the fine structure of red sprites. For an optimal configuration, so that the fields get projected upwards, the lightning discharge must be horizontal, i.e. the so called intracloud lightning or "spider lightning" [*Lyons*, 1994]. It is important to notice that in our model with $\beta = 0.025$ the ionization starts occurring for $I_o > 200$ kA (i.e. for $I_o > 200$ kA the equation for the evolution of the electron density n_e should be included).

We can compare these results with the simple tortuous random walk models (see Section 2.2.2). The maximum field strength at $x = 10$ km $y = 10$ km, $z = 60$ km is shown in Fig. 2.20a and the emission strength in Fig. 2.20b as a

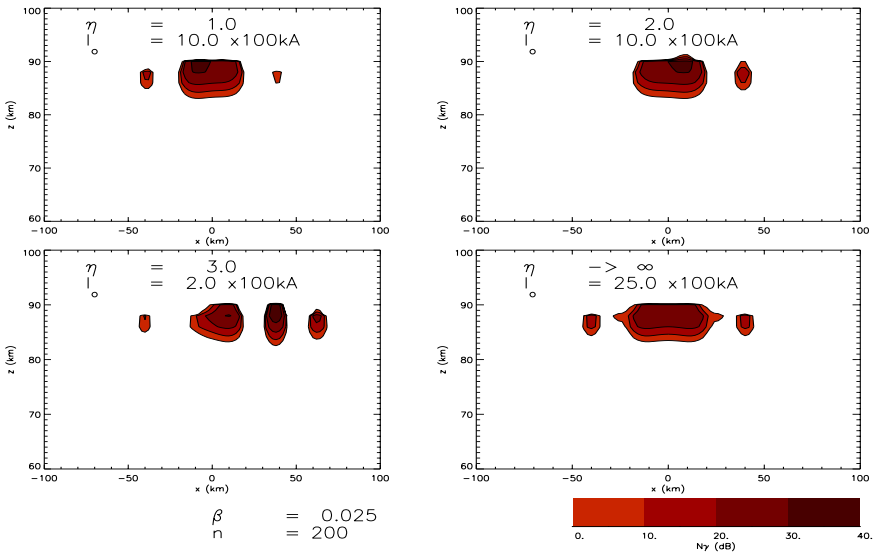

Figure 3.8: The emissions patterns at the line x=10 km corresponding to the four fractal structures of Fig 3.5 which have dimensions D= 1.55, 1.3, 1.2, 1.0 respectively. The current is chosen so that the emission intensity is about I(kR)$\simeq$100 kR, and $\beta = 0.025$.

function of the pathlength or dimension.

Therefore, we can obtain a significant increase in the strength of the radiated fields by treating the discharge as a fractal. Factors of 5 in the power density are not rare.

Certain fractals can radiate more effectively than others, but in general this problem is very complicated. The power density, and thus the emission pattern and intensity, scales as $S(W/m^2) \sim \beta^2 I_o^2$. There is some dependence in the radiation fields as a function of β as can be observed from Fig. 2.22. Clearly, Q, β, I_o, D are the relevant parameters that control the optical emission pattern and intensity.

Statistics of intracloud lightning are in the best cases incomplete, but in-

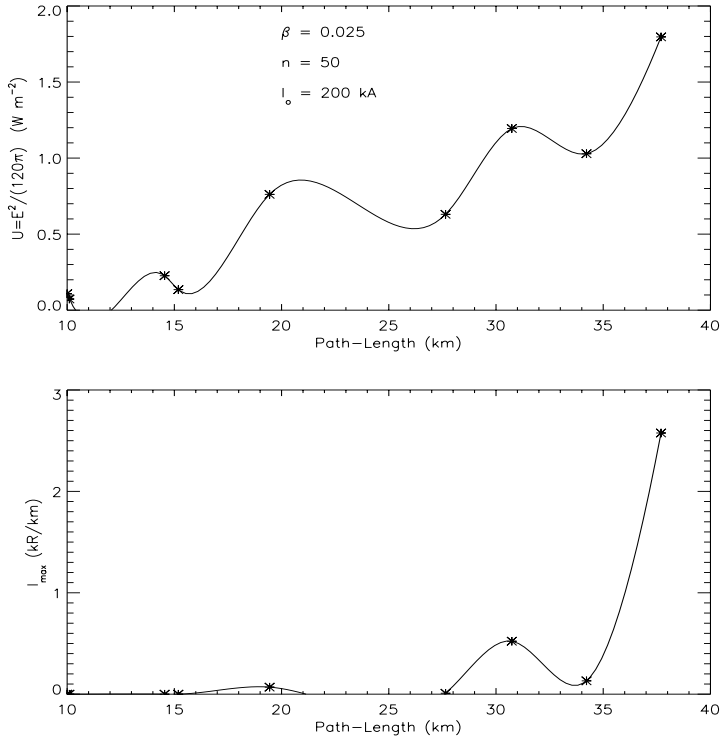

Figure 3.9: (a) The random walk model. (b) The time averaged intensity in kR/km for the random walk model as a function of the path length. The path length is increased after each succesive sudivision.

formation about some independent measurements can be found in the book by *Uman* [1987]. It seems to suggest that in extreme cases the intracloud discharge can reach $Q \sim 100$ C or 100 kA, with a length of 10s of kms. Some rough estimates can be made of the relevance of the model discharge parameters by comparing with the statistics of cloud-to-ground discharges given in *Uman* [1987]. A current peak of $I_o \sim 100$ kA, consistent with a charge transfer of $Q = 100$ C, occurs between 1-5 of the time. Statistics on the velocity of propagation are even less complete but few accounts seem to suggest a propagation speed of about $\beta \sim 0.01 - 0.05$. Therefore, our model discharge parameters seem to agree

with the statistics of red sprites observations as described in the introduction (Chapter 1).

We live in a world where dielectric discharges seem to have $D \sim 1.6$ [*Sanders* 1986, *Niemeyer et al.*, 1984]. On the other hand lightning discharges seem to show lower dimensions, a fact that might become relevant due to the sensitivity of the emission strength on the fractal dimension of the discharge. The optimal emissions intensity is obtained for dimensions $D \sim 1.3$ for the fractal models used above.

Chapter 4

Spectrum of Red Sprites

We proceed next to model the spectrum of red sprites due to the electron energization by the electric field from lightning. It capitalizes on the fact that there are two distinct timescales. A fast timescale on which a steady state electron distribution function $f(\mathrm{v})$ is established by balancing the electron energization rate with inelastic loses (see Appendix B), and a slow radiation timescale dominated by interlevel transfer and collisional quenching.

The electron energization is computed with the help of the Fokker-Planck code (described in Appendix B). We assume first that sprites located at a certain height z, and for the sake of definiteness assume that $z = 80$ km [*Lyons* , 1994; *Sentman et al.*, 1995; *Bossipio et al.*, 1995; *Winckler et al.*, 1996]. Then we discuss a more realistic model of a spatially integrated spectrum of red sprites.

Radiative deexcitation of the excited molecules produces optical flashes that superficially resemble those observed during auroras. However, unlike auroras which last for hours and in which even forbidden transitions need to be considered, red sprites have millisecond duration, so that only N_2 transitions faster than a millisecond excited by direct electron impact or through cascades need

to be retained (Fig. C.1). The radiative deexcitation involves:

- Direct pumping of the v vibrational level of the α electronic state by the electron impact.
- Cascade excitation.
- Radiation losses.
- Collisional quenching.

The usage of the stationary equations for the population of vibrational level is justified by the fact that radiative lifetime of the relevant electronic states have to be shorter than the duration T of electromagnetic pulse from lightning in order to be effectively pumped. Therefore, a stationary distribution of n_v^α is established during the pulse.

Note that since we consider the shape of sprite spectrum, only relative line intensities are of interest. Furthermore, the vibrational-electronic population depends linearly on the electron density (see Eq. (C.2)); as a result the spectrum is not affected by the possible increase in the electron density due to the ionization of the neutral gas by "hot" electrons. Using the above computational scheme we find the synthetic source spectrum $I_s(E_o, \lambda)$ of N_2 localized at 80 km which includes the first and second positive and first negative bands. It is presented in Fig. 4.1 for two values of the electric field amplitude $E_0 = 35$ and 70 V/m. Notice that only the 1P and 2P bands give a distinctive contribution to the source spectrum, while the $N_2^+(1N)$ band plays only a minor role since it can only be excited by "tail" electron having energy in excess of 19 eV. In comparison, this $N_2^+(1N)$ band is among the brightest in auroras since it is caused by high energy electrons.

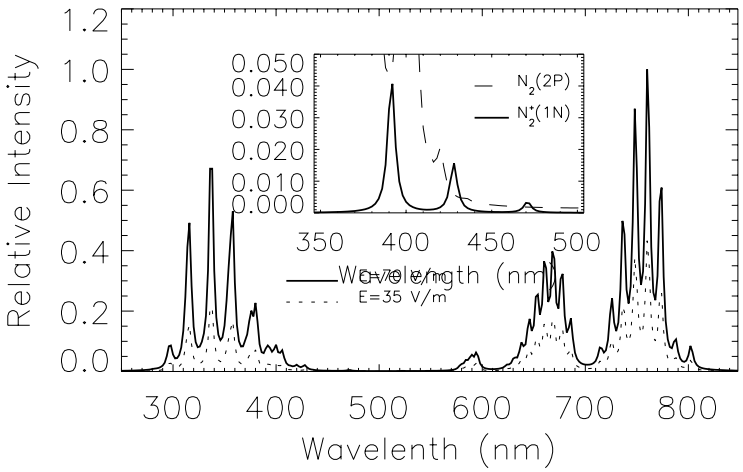

Figure 4.1: The source spectrum for field intensities E_o=35 and 70 V/m. Also shown is a zoom of the $N_2^+(1N)$ band, showing that its contribution is small for this type of electron energies.

The observed spectrum depends on the location of the detector. If observed from space, the spectrum is the same as the source spectrum $I_s(E_o, \lambda)$, while if observed from either ground or airplane it will be distorted by atmospheric attenuation. Atmospheric attenuation depends on the zenith angle χ of the optical source, the altitude h_o of the detector, and on the properties of the atmosphere, such as relative humidity and aerosol density. We consider the following contributions to the attenuation:

- absorption by ozone
- absorption by oxygen
- absorption by water vapor
- Rayleigh scattering by air molecules
- Mie scattering by aerosols.

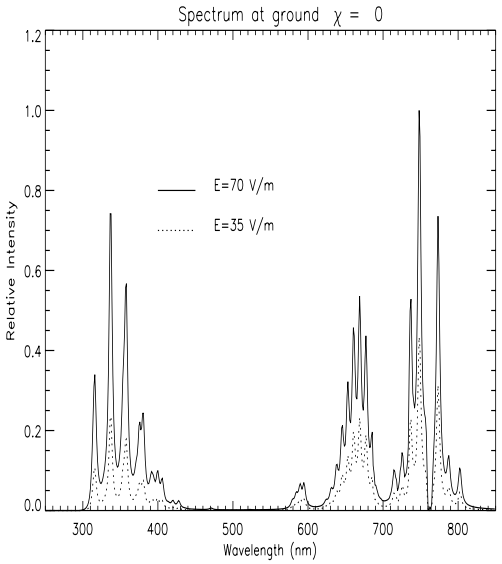

Figure 4.2: Spectrum with $\chi = 0$.

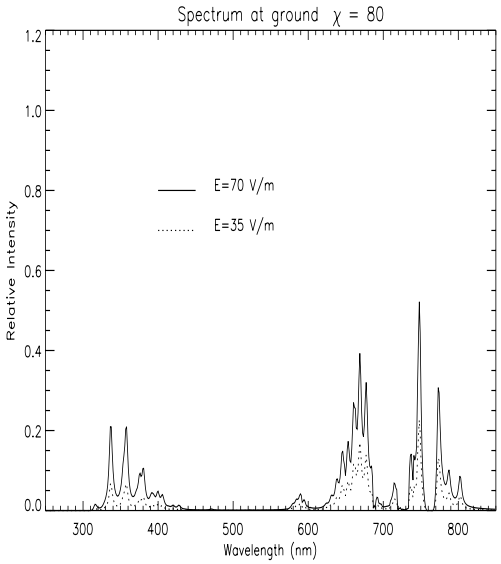

Figure 4.3: Spectrum with $\chi = 80$.

Figure 4.2 reveals the model sprite spectrum as observed by a ground based detector viewing the source at zero zenith angle $\chi = 0$. This spectrum differs significantly from the synthetic source spectrum 4.1 . First, the $N_2(2P)$ and $N_2^+(1N)$ bands are attenuated more significantly than the $N_2(1P)$ band. This effect is stronger for longer optical paths corresponding to higher zenith angle as seen in Fig 4.3 . By comparing the two peaks of the $N_2(1P)$ band, say 5-2 and 4-2 which undergo different absorption, one can estimate the zenith angle of the observed sprite.

From the optical spectrum one can retrieve the intensity of the pumping electric field. This is accomplished by comparing lines either belonging to different bands or to the same band. In the first case the ratio of excitation rates of the corresponding electronic levels depends on the direct pumping of the levels (mainly) and from cascades excitation. In the second case this ratio is controlled by the cascades excitation only.

Since only a few lines belonging to the 1P band have been observed so far [*Mende et al.*, 1995; *Hampton et al.*, 1996], in what follows we consider the vibrational transitions v - v′and $v_1 - v_1'$ belonging to the $N_2(1P)$ band. For given values of the relative intensities of two chosen spectral lines $I_{vv'}$ and $I_{v_1 v_1'}$ we obtain using Eqs. (C.2), (C.3) that

$$\frac{I_{vv'}}{I_{v_1 v_1'}} = \frac{A_{vv'}}{A_{v_1 v_1'}} \frac{\nu_{ex}^B F_{1,v'} + \sum_\alpha \nu_{ex}^\alpha F_{2,v'}}{\nu_{ex}^B F_{1,v_1'} + \sum_\alpha \nu_{ex}^\alpha F_{2,v_1'}} e^{-(\tau_{vv'} - \tau_{v_1 v_1'})} \tag{4.1}$$

where the summation is over B′, C and D electronic states reflecting the effect of excitation and cascade; $\tau_{vv'}$ and $\tau_{vv'}$ reveal the atmospheric absorption of the corresponding levels.

Generally speaking, one can obtain ratios $\nu_{ex}^{B'}/\nu_{ex}^B$, ν_{ex}^C/ν_{ex}^B and ν_{ex}^D/ν_{ex}^B by using intensities of three different spectral bands. This allows the evaluation of the electric field amplitude from Fig. C.2. This procedure requires knowledge of the atmospheric attenuation, which includes the zenith angle, as well as the relative humidity, and the aerosol number density. However, if the detector is boarded on a high altitude airplane, the absorption caused by the water vapor and aerosols becomes negligible. Thus the retrieval procedure is simplified. In order to illustrate the opportunities given by the proposed method we consider data from *Hampton et al.* [1996] presented in Fig. 4.4a which only shows the $N_2(1P)$ band. The ratio of the intensities of the 6-3 to the 7-4 transitions is 0.62/0.4. We take into account that for the chosen transitions the largest role is played by the direct pumping of the B level and by the cascade from the B′ level. The difference in the atmospheric attenuations, as we check with our model, was less than a few percent for the zenith angle $\chi \sim 80$. Substituting into Eq. (4.1) the ratio of the intensities we obtain that $\nu_{ex}^{B'}/\nu_{ex}^B \simeq 0.3$, and according to Fig. C.2 this corresponds to the electric field amplitude E_o= 35 V/m which at $z = 80$

km is below the breakdown threshold. Note that this estimate was made using noisy data which are not spatially resolved, and can be considered only as an illustrative example. However, the synthetic spectrum calculated for the electric field amplitude E $_o$= 35 V/m, the zenith angle of χ =80^o, and for the detector location of 4.3 km above the sea level, which is shown in Fig. 4.4b, resembles that observed by *Hampton et al.* [1996] at similar conditions, as revealed by Fig. 4.4a.

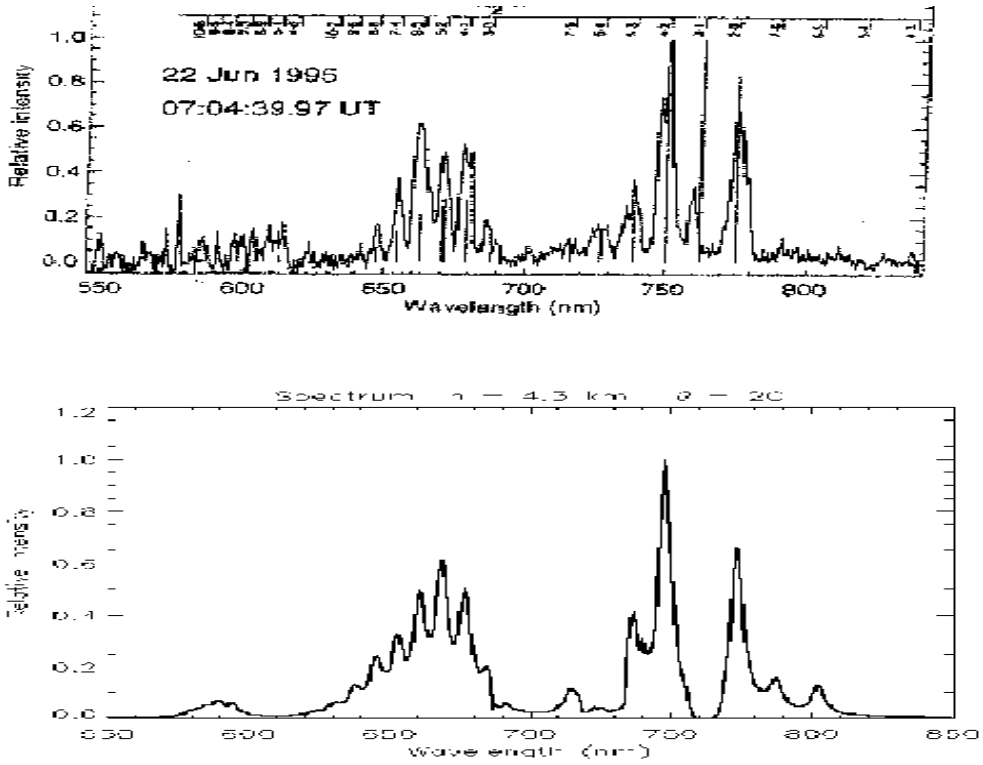

Figure 4.4: (a) The spectrum measured by Hampton et al., [1996] with χ = 80. (b) The modeled spectrum for the estimated E$_o$=35 V/m, which is close to the ionization threshold, was computed for the same conditions as the spectrum in (a)

To compare with actual spectrum measurements, we must consider the de-

tector column integration, as photons are emitted from different heights under different conditions, e.g. quiver energies, electron densities, neutral densities, collisional quenching, etc. The column integration, Eq. (C.3), must be carried carefully due to two factors:

- the height dependence of the quiver energy, the electron density, and neutral density;
- the height dependence of the collisional quenching.

We can apply the method we explained above to the electric field produced by our fractal lightning model in the lower ionosphere, as discussed in Chapter 2 and 3. For a definiteness we assume that the lightning discharge has a fractal dimension $D = 1.2$ ($\eta = 3$) with a current peak of $I_o = 100$ kA. We chose the field profile at the core of the sprites to carry the spatial integration Eq. (C.3). The result is shown in Fig. 4.5. In fact, for this electric field profile, the relative spectrum does not change considerably from the, properly normalized, spectrum computed for a slab at $h = 80$ km and of $\widetilde{\epsilon} = 0.1$ eV (35 V/m) revealed by a dashed line, the difference being only 10% for the short wavelengths of the 2P band and less than 1% for the longer wavelengths of the 1P band. We expected that the differences become more pronounce as the sprites spread downward below 70 km.

In conclusion, a model of the red sprite spectrum due to molecular excitation by ionospheric electrons accelerated by the electric field from lightning was developed. The model could allow us to evaluate the electric field amplitude by comparing the intensities of different spectral lines. The model also reveals some differences between the aurora and sprite spectra: in the aurora both permitted

and forbidden transitions play a noticeable role, while in sprites only permitted transitions are important. It seems that sprites are produced by electrons of much lesser energy than that of auroral electrons. Unlike the aurora, the collisions between excited molecules could affect sprites only in a few local spots. Sprites are normally observed at high zenith angle, so the spectrum is highly influenced by the atmospheric attenuation. For a given zenith angle and atmospheric constitution (i.e. humidity and aerosol density), the collisional quenching and the atmospheric attenuation can be computed accurately. As a result, if the measurements have good spatial resolution, the model output could in principle yield the spatial profile of the amplitude of the electric field causing the sprite.

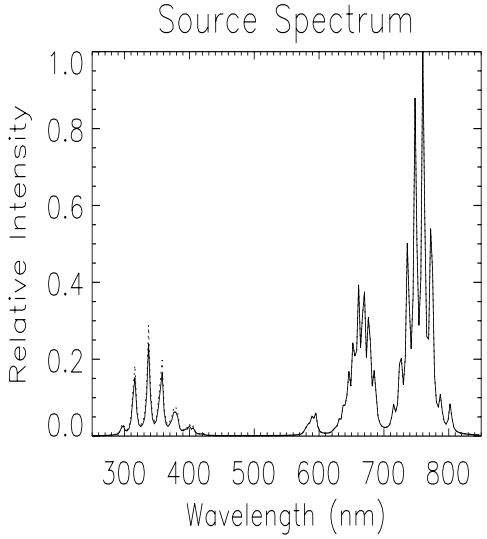

Figure 4.5: The spatially integrated source spectrum for a red sprite due to a lightning discharge of Q=100 C (solid line) along with that produced by a slab at 80 km corresponding to $\widetilde{\varepsilon} = 0.1eV$ (dashed line).

Part III

Runaway Discharge in a Magnetic Field

Chapter 5

Relativistic Beams as a Possible Source of HAL Phenomena

5.1 Runaway Breakdown

A new type of electrical air breakdown, called runaway breakdown or runaway discharge, was discussed recently by *Gurevich et al.* [1992] and applied to the preliminary breakdown phase of a lightning discharge. This phase occurs in the cloud vicinity and marks the initiation of the discharge [*Uman*, 1987]. The important property of the runaway breakdown is that it requires a threshold field by an order of magnitude smaller than the conventional breakdown discharge under the same pressure conditions. However, its initiation depends on the presence of seed electrons with energy in excess of tens keV in the high electric field region. Such energetic electrons are often present in the atmosphere as secondaries generated by cosmic rays [*Daniel and Stephens*, 1974].

The possibility for influence of cosmic ray secondaries on the lightning discharges was first discussed in a speculative manner by *Wilson* [1924]. Recently *McCarthy and Parks* [1992] attributed X-rays observed by aircrafts in associa-

tion with the effect of thundercloud electric field on runaway electrons. *Gurevich et al.* [1992] presented the first consistent analytic and numerical model of the runaway discharge and later on *Roussel-Dupre et al.* [1994] presented its detailed quantitative application to the X-ray observations.

The physics of the runaway discharge is based on the concept of electron runaway acceleration in the presence of a laminar electric field [*Dreicer*, 1960; *Gurevich*, 1960; *Lebedev*, 1965]. The runaway phenomenon is a consequence of the long range, small angle scattering among charged particles undergoing Coulomb interactions. The scattering cross section decreases with velocity as $\sigma \sim \mathrm{v}^{-4}$ [*Jackson* 1975]. As a result for a given electric field value a threshold energy can be found beyond which the dynamic friction, as shown in Fig (5.1), cannot balance the acceleration force due to the electric field resulting in continuous electron acceleration.

5.1.1 Fully Ionized Case

Here we review the basic physics of the electron runaway in unmagnetized plasmas, starting with the electron acceleration in a fully ionized plasma. The cold electrons having mean directed velocity v less than the electron thermal speed $\mathrm{v}_T = \sqrt{T/m}$ undergo the dynamical friction force

$$F = m\nu_o \mathrm{v}$$

which is proportional to the electron velocity v as shown by trace 1 in 5.1, since at $\mathrm{v} < \mathrm{v}_T$ the electron collision frequency $\nu = \nu_o$ is constant, defined by the electron thermal speed. However, for fast electrons having the velocity larger

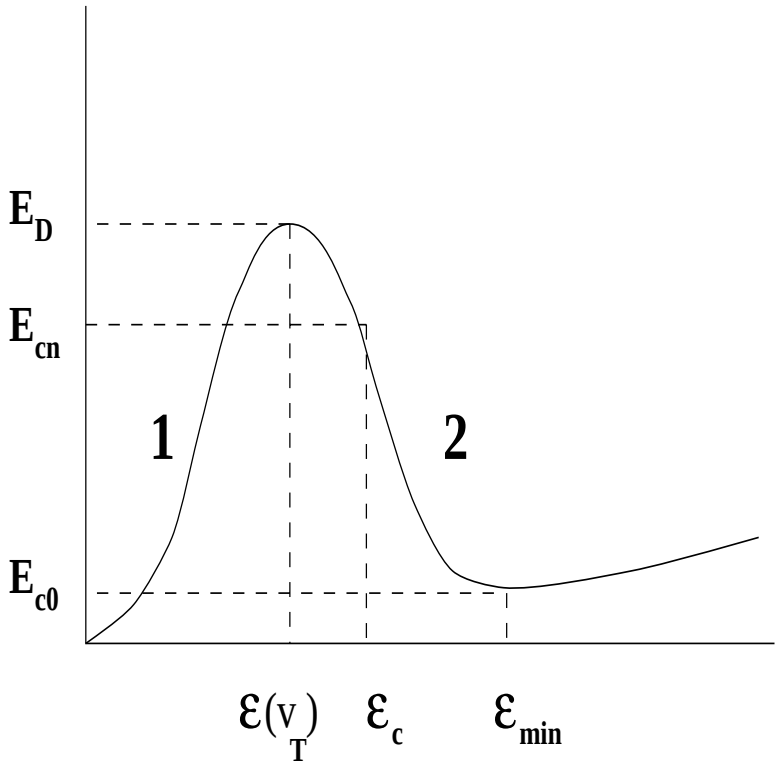

Figure 5.1: Schematic of the dynamical friction force as a function of the electron energy. Trace 1 corresponds to a cold fully ionized plasma (v$<$ v_T), Trace 2 corresponds to high energy electrons. It is valid for any plasmas fully or low ionized. Here E_D is the Dreicer field, while E_{cn} and E_{c0} are the critical and minimum runaway fields correspondingly.

than v_T, the dynamical friction force given by [*Jackson* 1975]

$$F = m\nu(\mathrm{v})\mathrm{v} = \frac{4\pi e^4 Z n_e}{m\mathrm{v}^2}\ln\Lambda \tag{5.1}$$

reduces when the velocity increases as shown by the trace 2 on Fig. 5.1, where n_e is the electron density, and Λ is the Coulomb logarithm. As a result the friction force has a maximum at v_T. The electric field which balances the dynamical

friction force at $v = v_T$ is known as Dreicer or critical field:

$$E_D = E_{ci} = \frac{4\pi e^3 Z n_e}{T} \ln \Lambda$$

As illustrated by Fig. 5.1 the dynamical friction cannot confine the plasma electrons, which become runaway, if the electric field E applied to the plasma is higher than E_D. On the contrary, if the applied field is less than E_D, electrons are confined by the dynamical friction. At the same time the electrons acquire relatively small velocity v_E, directed along E. Thus the plasma is heated resistively. However, even in this regime the friction force cannot confine fast electrons having energy $\epsilon > \epsilon_c \simeq T\frac{E_D}{E}$ (see Fig. 5.1). Such electrons are continuously accelerated by the electric field and run away. For instance, tokamaks usually operate in the regime of resistive heating, but under some conditions the runaway regime can also takes place in tokamaks.

5.1.2 Weakly Ionized Plasma

A similar situation occurs in a weakly ionized plasma. But unlike the fully ionized plasma, the collision frequency of the low velocities electrons in the weakly ionized gas is determined by the cross-section of the electron-neutral collision, rather than by the thermal electrons. However, for electrons with energies in excess of the ionization potential ($\epsilon > \epsilon_i$) the interactions with the nuclei and atomic electrons obey the Coulomb law, hence the dynamical friction force decreases with the electron energy, [*Bethe and Ashkin*, 1953] as given by Eq. (5.1). In this case the value of the critical electric field is given by *Gurevich*, [1960]

$$E_{cn} = \frac{4\pi e^3 Z N}{\epsilon_i} k_n$$

Notice that N is the density of the neutral molecules and Z is the mean molecular charge, which for air is 14.5, and k_n is the numerical factor, determined by the type of the neutral gas. In fact, for hydrogen $k_n \simeq 0.33$, for helium $k_n \simeq 0.30$. If the electric field is larger than E_{cn} the whole bulk electrons are accelerated. If the field is less than E_{cn}, only a few electrons having energy higher than ϵ_c are accelerated

$$\epsilon > \epsilon_c = \frac{2\pi e^3 Z N \ln \Lambda_n}{E}$$

where $\Lambda_n \simeq \epsilon_c / Z\epsilon_i$. These are the runaway electrons in the neutral gas.

We emphasize that the amplitude of the electric field leading to the electron runaway is limited, since only for nonrelativistic electrons the dynamical friction force drops when the electron energy increases [*Bethe and Ashkin*, 1953]. For the electrons having energy greater than $\epsilon \geq 10$ keV the dynamical friction force due to collisions with the neutral gas is given by [*Bethe and Ashkin*, 1953]

$$F = \frac{4\pi Z e^4 N}{mc^2} a\ \Phi(\gamma)$$

$$a\Phi = \frac{\gamma^2}{\gamma^2 - 1}\{\ln \frac{mc^2\sqrt{\gamma^2-1}\sqrt{\gamma-1}}{\sqrt{2}I} - [\frac{2}{\gamma} - \frac{1}{\gamma^2}]\frac{\ln 2}{2} + \frac{1}{2\gamma^2} + \frac{(\gamma-1)^2}{16\gamma^2}\} \quad (5.2)$$

where $\gamma = 1/\sqrt{1 - \frac{v^2}{c^2}}$ is the Lorenz factor, $I = 80.5$ eV, $a \simeq 10.87$ in air, and $\Phi(\gamma)$ is $F(\gamma)$ normalized to unity. For nonrelativistic electrons the dynamical friction force rapidly decreases with the increase of the electron momentum

$$F = \frac{4\pi Z e^4 N m}{p^2} \ln(\frac{p^2}{2mI})$$

The dynamical friction force, Eq. (5.2), reaches its minimum value

$$F_{\min} = \frac{4\pi Z e^4 N}{mc^2} a$$

at $\gamma \min = 3.42$, $\epsilon_{\min} = 1.2$ MeV, $p_{\min} = 3.27$ mc. F then slowly (logarithmically) increases with γ as it is shown in Fig. 5.1. Therefore, the minimum of the friction

force F_{min} is related to the minimum value of the electric field E_{c0}, which still generates the runaway

$$E_{c0} = \frac{4\pi Z e^3 N}{mc^2} a$$

Therefore in the air the runaway electrons could appear in a wide range of electric field $E_{c0} < E < E_{cn}$ which spans almost three orders of magnitude. Similar limitation on the electron runaway takes place for the electrons in a fully ionized plasma [*Connor and Hastie*, 1975].

The detailed discussion of the electron runaway in the air caused by the electric fields due to thunderstorm is presented by *McCarthy and Parks* [1992]. A new step in the theory of runaway electrons was made by *Gurevich et al.* [1992], who discussed the possibility of producing an avalanche of runaway electrons. The basic idea is that the fast electrons ionize the gas molecules producing a number of free electrons. Some of secondary electrons have energy higher than the critical energy of runaway. Those electrons are accelerated by the electric field and in turn are able to generate a new generation of fast electrons. This avalanche-like reproduction of fast electrons is accompanied by the exponential increase of the number of thermal secondary electrons, i.e. the electrical breakdown of gas occurs. Such kind of the runaway breakdown is often called runaway discharge. It has the following main properties:

- 1. The critical field of the runaway breakdown is an order of magnitude below the threshold of the conventional air breakdown.

- 2. The runaway discharge has to be triggered by the high energy electrons of $\epsilon > \epsilon_c$.

- 3. The runaway discharge develops inside the streamers directed along the

electric field [*Gurevich et al.*, 1994].

- 4. The runaway discharge is followed by the generation of x- and γ -ray emissions [*Roussel-Dupre et al.*, 1994].

These properties allow us to consider the runaway discharge as the possible mechanism which initializes the lightning discharge during thunderstorms.

To help with future calculations, we note that the value of the critical electric field as a function of altitude is given by $E_{c0} = \frac{4\pi Ze^3}{mc^2} Na \simeq 2 \times 10^5 \times e^{-h/H_o}$ V/m, where $H_o \simeq 6.5$ km is the atmospheric scale height.

5.1.3 First Neglect Friction: Go to a Parallel Frame

As the friction force becomes smaller with height, the magnetic field must be included in the analysis. This is especially true for the equatorial regions where the laminar electric field due to lightning is predominantly perpendicular to the magnetic field [*Papadopoulos et al.*, 1996]. Note that in the case of E$\perp$B, a geometry expected in the equatorial region, the electrons will be accelerated only when $E > B$, if we neglect the dynamical friction. Suppose we first neglect the dynamical friction and quantify what is the E field required to produce infinite acceleration for a given **E**, **B** configuration where θ_o is the angle between the electric and geomagnetic fields.

We follow Papadopoulos et al., [1996] and study the runaway acceleration of a test electron in crossed static electric and magnetic fields by transforming the equations of motion to a reference frame moving with the velocity βc relative to the ionospheric frame in which the transformed fields $\mathbf{E}'$, $\mathbf{B}'$ are parallel. In this frame the electrons can be treated as unmagnetized. Following *Jackson* [1975]

the electric and magnetic field in a moving frame are

$$\mathbf{E}' = \gamma(\mathbf{E} + \beta \times \mathbf{B}) - \frac{\gamma^2}{\gamma^2 + 1}\beta(\beta \cdot \mathbf{E}) \tag{5.3}$$

$$\mathbf{B}' = \gamma(\mathbf{B} - \beta \times \mathbf{E}) - \frac{\gamma^2}{\gamma^2 + 1}\beta(\beta \cdot \mathbf{B}) \tag{5.4}$$

$$\gamma = 1/\sqrt{1 - \beta^3}$$

with $\mathbf{E}'^2 - \mathbf{B}'^2 = \mathbf{E}^2 - \mathbf{B}^2$ and $\mathbf{E} \cdot \mathbf{B} = \mathbf{E}' \cdot \mathbf{B}'$. We must find the β required to have $\mathbf{E}' \| \mathbf{B}'$, however there is an infinite number of solutions since any frame parallel to the $\mathbf{E}' \| \mathbf{B}'$ direction will also preserve such relationship. We constrain the solution by requiring that $\beta \cdot \mathbf{E} = \beta \cdot \mathbf{B} = \mathbf{0}$ and $\mathbf{E}' \times \mathbf{B}' = \mathbf{0}$. Using Eq. (5.3) and Eq. (5.4) we obtain $(\mathbf{E} + \beta \times \mathbf{B}) \times (\mathbf{B} - \beta \times \mathbf{E}) = \mathbf{0}$ and with the help of the above constraints we get

$$\beta = \mathbf{E} \times \mathbf{B} \frac{E^2 + B^2 - \sqrt{(E^2 - B^2)^2 + 4(\mathbf{E} \cdot \mathbf{B})^2}}{2(\mathbf{E} \times \mathbf{B})^2}$$

but more relevant is the equation of the transformed fields

$$E'^2 = \frac{1}{2}[E^2 - B^2 + \sqrt{(E^2 - B^2)^2 + 4(\mathbf{E} \cdot \mathbf{B})}]$$

$$B'^2 = \frac{1}{2}[B^2 - E^2 + \sqrt{(E^2 - B^2)^2 + 4(\mathbf{E} \cdot \mathbf{B})}]$$

Notice that in the case $\mathbf{E} \cdot \mathbf{B} = \mathbf{0}$ we have the two limits:

- If $E > B$ then $B' = 0$ and $E' = \sqrt{E^2 - B^2}$.
- If $B > E$ then $E' = 0$ and $B' = \sqrt{B^2 - E^2}$

As a result there is not acceleration in the case of crossed electric and magnetic field with $B > E$. Therefore, the characteristic electric field in SI units is $E(\frac{kV}{m}) = 30\ B(G)$ where B is the local magnetic induction. Since at the equator

the magnetic field is $B = 0.25$ G, the required field accelerate an electron corresponds to $E = 7.5\ \frac{kV}{m}$. This threshold applies to the condition that $\mathbf{E} \cdot \mathbf{B} = \mathbf{0}$ which is the situation for electrons above a thunderstorm close to the equator.

This threshold field is also independent of height at long as the gyroradius is smaller than the mean free path of runaways which occurs at altitudes as low as 25 km for sensible electric fields [*Longmire*, 1978; *Papadopoulos et al.*, 1994]. The above results can be extended to any angle between the electric and magnetic fields. In the parallel frame, the E' field still needs to beat the coulomb friction force, i.e. $E' > E'_{c0}$. Figure (5.2) shows the condition in the $(E/B_o, \theta_o)$ plane where $E' = E'_{c0}$. Note the constraint at $\theta_o = \pi/2$.

This is a qualitative analysis, that constraints the field to a threshold value $E \sim 7.5\ \frac{kV}{m}$, which seems to be a characteristic threshold in the presence of the Earth's magnetic field. Of course the Coulomb friction term is not covariant, hence, its frame transformation is far from trivial. The detailed quantitative approach will be presented in the following sections.

5.2 Boltzmann Equation

The Boltzmann equation for the high energy ($\varepsilon > 10$ keV) electron distribution function where the interactions are primary Coulomb in nature can be written as [*Roussel-Dupre et al.*, 1994]

$$\frac{\partial f}{\partial t} - e(\mathbf{E} + \frac{\mathbf{v}}{c} \times \mathbf{B}_o) \cdot \frac{\partial f}{\partial \mathbf{u}} = \frac{\partial_e f}{\partial t} \tag{5.5}$$

$$\frac{\partial_e f}{\partial t} = \frac{1}{\mathrm{u}^2} \frac{\partial (\mathrm{u}^2 \Phi f)}{\partial \mathrm{u}} + \frac{(\frac{Z}{2} + 1)\Phi}{4\mathrm{u}\gamma} \frac{\partial}{\partial \mu} [(1 - \mu^2) \frac{\partial f}{\partial \mu}]$$
$$+ \frac{\beta}{2a} \int d\Omega \int_{\gamma_i}^{\infty} d\gamma' [\frac{\gamma'^2 - 1}{\gamma^2 - 1}] f(\gamma', \mu') \tilde{\sigma}(\gamma', \gamma, \zeta) \tag{5.6}$$

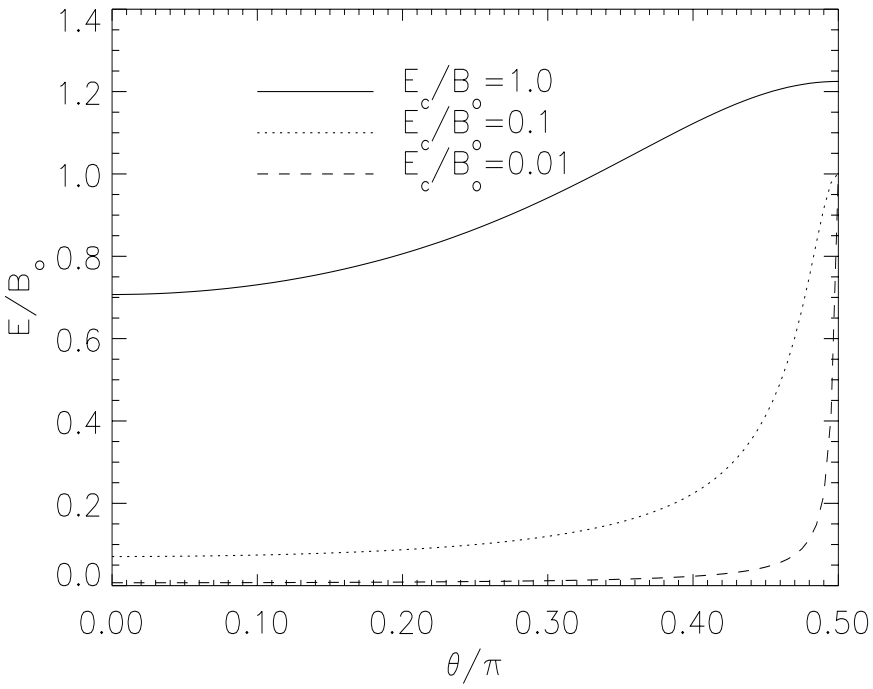

Figure 5.2: The curve in the (E,θ) plane where the transformed field is equal to zero.

where $\mathbf{u} = \gamma\beta$, ζ is the angle between the incident and the scattered electron, $\tilde{\sigma}(\gamma', \gamma, \zeta)$ is the normalized dimensionless double differential ionization cross-section [*Roussel-Dupre et al.*, 1994], γ_i corresponds to the ionization energy ε_i, and the time has been normalized to $t \rightarrow t/\tau_c$ with

$$\tau_c = 8.5\, e^{h/H_o}\ (n\,\mathrm{sec})$$

The three terms of the right part of Eq. (5.6) corresponds to:

- The change of energy due to the friction force for electrons moving through the neutral gas.
- The angular scattering effect.

- The production of secondary electrons creating the runaway avalanche if the secondary has energy greater than threshold energy.

The exact solution of this complicated equation is out of the scope of this work, but it is instructive to understand the time scales and relative importance of the different terms. The main questions is: **what are the constraints imposed by the magnetic field?**

5.2.1 Mean Free Path

In attempting to apply the concept of runaway breakdown driven by a laminar lightning induced vertical electric field at altitudes exceeding 30 km one is faced with a main difficulty. For such altitudes the effective mean free path $\lambda_R(\gamma)$ for runaway electrons given by

$$\lambda_R(\gamma) = \frac{\mathrm{v}}{\nu(\mathrm{v})} = \beta\gamma \frac{mc^2\sqrt{\gamma^2-1}}{\gamma F(\gamma)} \simeq 2.5\ \beta\gamma \frac{\sqrt{\gamma^2-1}}{\gamma\Phi(\gamma)} e^{h/H_o}\ m$$

can exceed the electron gyroradius

$$\lambda_B(\gamma) = \beta\gamma \frac{c}{\Omega_B} \simeq 55\ \beta\gamma\ m$$

in the geomagnetic field.

The height h at which the electron gyroradius becomes greater than the runaway mean free path is shown in Fig. 5.3a as a function of the electron energy. So even at relatively low heights $h \sim 25$ km, the magnetic field becomes relevant. Conversely, we could insist in a low energy runaway at the cost of a high field. Figure 5.3b shows the electric field required to produce a runaway

$$\frac{E(\gamma)}{E_{c0}} = \Phi(\gamma)$$

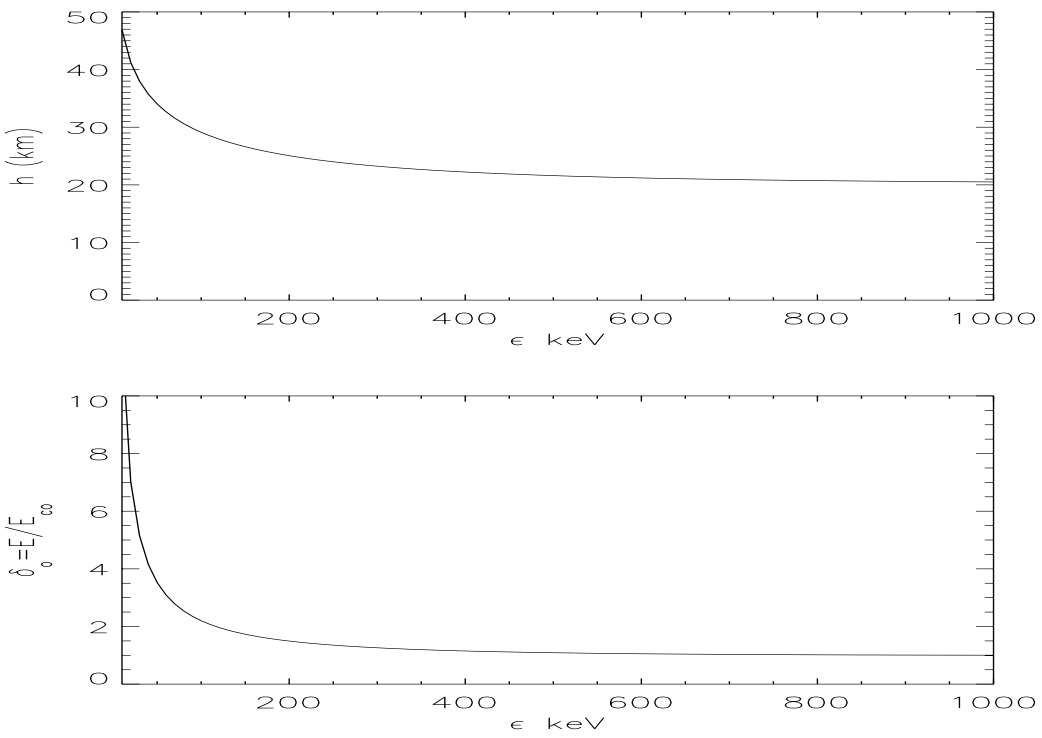

Figure 5.3: (a) The height h at which the electron gyroradius becomes greater than the runaway mean free path. (b) The normalized field required to produce the runaway breakdown at a given energy.

as a function of γ, normalized by the minimum field E_{c0} required to produce a runaway for $\gamma = 3.4$. Notice that in this graph we are assuming that magnetic effects can be neglected. The large electric field required to produce a low energy runaway may become a relevant constraint, since lightning induced electric fields of that magnitude may be hard to produce.

5.2.2 Scattering

The magnetic field gyration can be considered as a form of scattering and should be compared with the scattering term of Eq. (5.6). Their ratio can be written

as

$$\tau_s(\gamma)\frac{\Omega_B}{\gamma} \sim \frac{1}{3}\frac{\sqrt{\gamma^2-1}}{(\frac{Z}{2}+1)\Phi(\gamma)}e^{h/H_o}$$

as long as the distribution function is not extremely structured in the angle μ, i.e. no filaments exist. First if $\tau_s(\gamma)\frac{\Omega_B}{\gamma} < 1$ the collision dominates the runaway process and the electrons can be considered as unmagnetized. If $\tau_s(\gamma)\frac{\Omega_B}{\gamma} > 1$ then the magnetization becomes a considerable factor. The height at which the gyrofrequency becomes more important than the scattering frequency, $\tau_s(\gamma)\frac{\Omega_B}{\gamma} = 1$, is shown in Fig. 5.4 as a function of the electron energy.

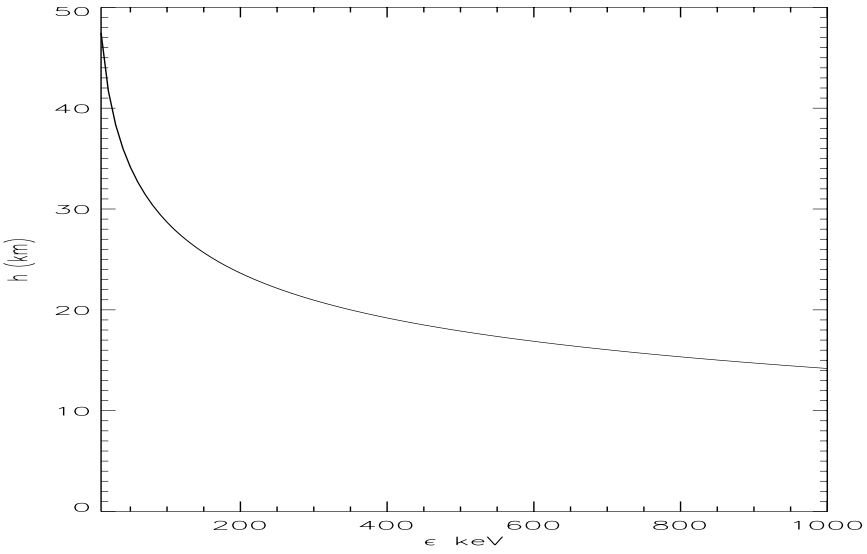

Figure 5.4: The height at which the gyrofrequency becomes a relevant factor.

Again we reach the same conclusion that the magnetic field becomes very relevant at heights $h \geq 25$ km, and must be included in the analysis.

5.2.3 Ionization

The time scale for ionization can be found from the last term in the right of Eq. (5.6) and is given by $\tau_i \sim 10 \times \tau_c$. Hence the time scale for the avalanche is slower than the time scale for the changes in energy or scattering. Therefore, we can study the runaway process and the threshold requirements for the runaway process using single particle trajectories, as we will do next. As a result, the electric and magnetic fields must be included in a theory of the runaway acceleration for heights above $h \sim 30$ km where the high altitude phenomena seems to occur. Furthermore, we can learn relevant properties of the runaway process by observing single particle trajectories.

5.3 Runaway Discharge in a B Field

In the presence of a magnetic field the conditions for electron runaway are different from those described for a pure static electric field. In order to discuss the effects caused by magnetic field we will study the motion of fast electrons in the air under the influence of both electric **E** and magnetic field **B**. The equation of motion can be found from the Boltzmann equation, Eq. (5.6), and is given by

$$\frac{d\mathbf{p}}{dt} = e\mathbf{E} + \frac{e}{mc\gamma}(\mathbf{p} \times \mathbf{B}) - \nu\mathbf{p} \qquad \nu(\gamma) = F(\gamma)/p \tag{5.7}$$

where **p** is the electron momentum, ν is the electron collision frequency, F(γ) is the dynamical friction force which is a function of electron energy and is given by Eq. (5.2). We consider now the stationary solution of Eq. (5.7)

$$\mathbf{p}_{st} = \frac{eEp}{F_D(1+\omega_c^2/\nu^2)}\{\hat{\mathbf{e}} + \frac{\Omega_B^2}{\nu^2}\hat{\mathbf{h}}\cos\beta - \frac{\Omega_B}{\nu}\hat{\mathbf{e}}_\perp \sin\theta_o\} \tag{5.8}$$

where $\hat{\mathbf{e}}$, $\hat{\mathbf{h}}$ and $\hat{\mathbf{e}}_\perp$ are the unity vectors directed along **E**, **B**, and **E** $\times$ **B** correspondingly, θ_o is the angle between **E** and **B**. The electron cyclotron frequency is $\Omega_B = eB/mc\gamma$, and taking into account Eq. (5.7) the ratio Ω_B/ν can be presented as

$$\frac{\Omega_B}{\nu} = \frac{eB}{F}\frac{p}{mc\gamma} = \frac{eB}{F_D}\frac{\sqrt{\gamma^2-1}}{\gamma}$$

The function Ω_B/ν determines the effect caused by the magnetic field on the electron motion. Note that this ratio changes rapidly with the height and with the electron energy. We also have to mention that the momentum $\mathbf{p}_{st}$ is given by the solution of Eq. (5.8) which is an implicit function, since both the dynamical friction force F_D and collision frequency ν depend on the absolute value of momentum p. Actually, Eq. (5.8) represents a set of algebraic equations, which allows us to obtain $\mathbf{p}_{st}$. To solve this equation set, we consider first the equation

for the absolute value of the momentum p

$$1 = \frac{eE}{F}\frac{\sqrt{1+(\frac{\omega_c^4}{\nu^4}+\frac{\omega_c^2}{\nu^2})\cos^2\theta_o+\frac{\omega_c^2}{\nu^2}}}{1+\frac{\omega_c^2}{\nu^2}} \tag{5.9}$$

where F, Ω_B and ν all depend on p. Note that in order to obtain the above equation we took into account the following relation

$$|\hat{\mathbf{e}}+q\hat{\mathbf{h}}-q_1\hat{\mathbf{e}}_\perp| = \sqrt{1+q^2+2q\cos\theta_o+q_1^2\sin^2\theta_o}$$

where q and q_1 are certain functions. We solve Eq. (5.9) to obtain the absolute value of momentum p. Substitute it then into the right side of Eq. (5.8) to obtain the desired stationary solution in the form $\mathbf{p}_{st} = \mathbf{p}_{st}(\mathbf{E},\mathbf{B},N_m)$. Note that if the electric field is significantly higher than the critical field $E \geq 2E_{c0}$ the minimum electron kinetic energy required for runaway is $\epsilon_{st} < mc^2$. The minimum field requirement is increased in the presence of the magnetic field, hence $E \geq E_{c0}$ must at least be always satisfied.

In the absence of magnetic field ($B = 0$) Eq. (5.9) determines two stationary points at $E > E_{c0}$. The first of these points is reached for $p_{st} < p_{min}$ given by Eq. (5.2). This is an unstable point. It means that the electrons having $p < p_{st}$ are decelerated, while the electrons with $p > p_{st}$ are accelerated and run away. The mentioned above limit is correct for the momentum parallel to the electric field. If the initial electron momentum possesses a component orthogonal to $\mathbf{E}$, a separatrix appears which separates the runaway electrons from those losing their energy [*Gurevich et al.*, 1992; *Roussel-Dupre et al.*, 1994]. The same picture is correct if the constant magnetic field $\mathbf{B}$ exists which is parallel to $\mathbf{E}$. However, if a component of $\mathbf{E}$ orthogonal to $\mathbf{B}$ appears, it can significantly change the above picture. Let us consider a case when $\mathbf{E}\perp\mathbf{B}$. We first introduce the dimensionless

$$\delta_o = E/E_{c0} \qquad \eta_o = B/E_{c0}$$

parameters which allow us to rewrite Eq. (5.9) as

$$\delta_o^2 = \Phi^2(\gamma) + \eta_o^2(1 - 1/\gamma^2) \tag{5.10}$$

$$\Phi(\gamma_{\rm min}) = 1,\ \gamma_{\rm min} = 3.42$$

where $\Phi(\gamma) = F_D(\gamma)/eE_{c0}$. This equation defines the value of γ_{st} and correspondingly $\mathbf{p}_{st}$ for different parameters δ_o and η_o as solution to Eqs. (5.8) and (5.9) respectively. We find next the dimensionless critical field δ_{c0} as the minimum value of $\delta_o(\gamma)$ which still allows solution of Eq. (5.10). Equating the derivative $\mathrm{d}\delta_o^2\ /\mathrm{d}\gamma$ to zero we find

$$\eta_o^2 = -\gamma^3 \Phi(\gamma) \frac{d\Phi(\gamma)}{d\gamma}$$

and

$$\delta_{c0} = -\gamma(\gamma^2 - 1)\Phi(\gamma)\frac{d\Phi(\gamma)}{d\gamma} + \Phi^2(\gamma)$$

which determine an implicit form the dimensionless critical field δ_{c0} and minimum value γ_c, depending on the dimensionless magnetic field η_0. In fact, in the absence of a magnetic field ($\eta_o = 0$) we obtain that $\delta_{c0} = 1$, $\gamma_c = \gamma_{min} = 3.42$. Figure 5.5 reveals that the critical electric field δ_{c0} gradually increases, as the magnetic field η_0 rises.

We find now the asymptotic form for δ_{c0} at high values of η_0. In order to do it we take into account that at high η_0 the value $(\mathrm{v/c})^2 \ll 1$, so the nonrelativistic dynamical friction force can be applied. Therefore the function $\Phi(\gamma)$ is rewritten as

$$\Phi(\gamma) = \Phi_o \frac{\gamma^2}{\gamma^2 - 1} \qquad \Phi_o \simeq 0.913$$

from which we obtain that

$$\delta_{c0} = \frac{\sqrt{3}\Phi_o^{1/3}}{2^{1/3}}\eta_o^{2/3}, \qquad \frac{\gamma_c^2 - 1}{\gamma_c^2} = \frac{\sqrt{3}\Phi_o}{\delta_{c0}} \tag{5.11}$$

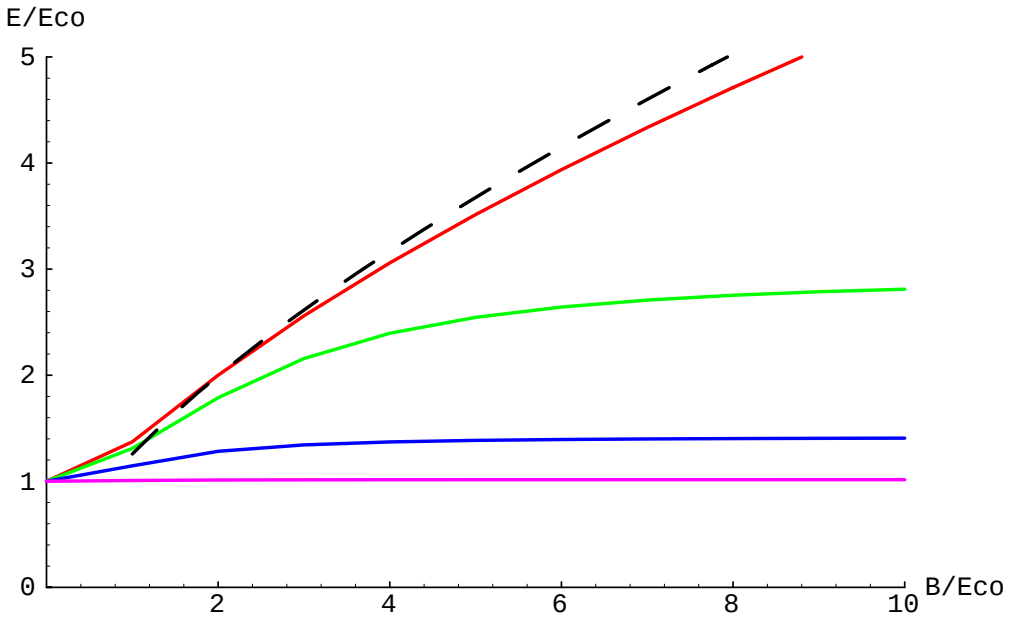

Figure 5.5: Threshold electric field E_{c0} versus magnetic field η_o obtained for θ_o = 90^o, 70^o, 45^o and 10^o (for curves from top to bottom respectively). A dashed trace shows analytical approximation valid at $\theta_o = 90^o$ for the nonrelativistic case.

The asymptote given by Eq. (5.11) is shown by a dashed trace in Fig. 5.5. The above discussion was focused on an instructive case when $\mathbf{E}\perp\mathbf{B}$. However, Eq. (5.9) allows us to obtain the critical electric field δ_{c0} as a function of the magnetic field η_0 for an arbitrary angle θ_o between the directions of the electric and magnetic field. This is shown in Fig. 5.5. In fact, for $\theta_o < 45^o$ the critical electric field practically does not depend on the value of the magnetic field, which resembles the runaway as it occurs in the absence of the magnetic field and is driven by $\mathrm{E}_{||}$. Note that the runaway electron moves at an angle α to the direction of the electric field, where the angle α is obtained from Eq. (5.8). In fact, for $\mathbf{E}\perp\mathbf{B}$, i.e. $\theta_o = 90^o$ it acquires the following form

$$\mu = \cos\alpha = (1 + \frac{\eta_o^2(\gamma^2-1)}{\gamma^2\Phi^2(\gamma)})^{-1/2}$$

The conclusion is that electrons having low energy ($\gamma \simeq 1$) move almost parallel to the direction of the electric field. This is due to the fact that for low electron energy the electron collision frequency is much higher than the cyclotron frequency ω_c, thus the effect caused by the magnetic field on the electron motion is not significant. When the electron energy increases, the electron collision rate reduces rapidly. It leads to a deflection of the electron velocity from the direction of the electric field. As the magnetic field increases the angle α gradually tends to $\pi/2$, i.e., in a strong magnetic field relativistic electrons start drifting in the $\mathbf{E} \times \mathbf{B}$ direction.

5.3.1 The Electron Runaway Basin Boundary

We study next the equation of the electron motion in order to obtain the separatrix between the two regimes: those electrons which possess trajectories that take them to higher energies, and the other electrons which possess trajectories leading to zero energy. Using the dimensionless variables δ_0 and η_0 Eq. (5.7) is presented as

$$\begin{aligned}
\frac{du_x}{d\tau} &= \delta_o + \frac{\eta_o}{\gamma} u_y \sin\theta_o - \frac{\Phi(\gamma)}{\sqrt{\gamma^2-1}} u_x \\
\frac{du_y}{d\tau} &= -\frac{\eta_o}{\gamma} u_x \sin\theta_o + \frac{\eta_o}{\gamma} u_z \cos\theta_o - \frac{\Phi(\gamma)}{\sqrt{\gamma^2-1}} u_y \\
\frac{du_z}{d\tau} &= -\frac{\eta_o}{\gamma} u_y \cos\theta_o - \frac{\Phi(\gamma)}{\sqrt{\gamma^2-1}} u_z \\
\gamma &= \sqrt{1 + u_x^2 + u_y^2 + u_z^2}
\end{aligned} \tag{5.12}$$

where we use the dimensionless momentum by normalizing the conventional momentum over mc, i.e. $\mathbf{u} = \mathbf{p}/mc$; τ is the dimensionless time

$$\tau = t/\tau_c$$

where $\tau_c = \frac{mc}{eE_{c0}} = 8.5\, e^{h/H_o}$ $(n\,\mathrm{sec})$. Here the electric field goes along the x axis, while the magnetic field is located in the x-z plane. Equations (5.12) were integrated numerically. Results of the computation are discussed starting with two limit cases: $\mathbf{E}\perp\mathbf{B}$, i.e. θ_o=90^o, and $\mathbf{E}\,||\,\mathbf{B}$, i.e. θ_o=0.

5.3.2 Electron Runaway in Perpendicular Electric and Magnetic Fields

In this case the momentum is fading along the axes z, so essentially electrons are moving in the x-y plane. At low magnetic field $\eta_o < \delta_o$ two kind of trajectories occur depending on the initial conditions. An electron having low initial energy will lose its energy and eventually stops, while an electron having high enough initial energy runs away along an almost linear trajectory in the $\widehat{e} - \widehat{e}_\perp$ plane, and gains the energy. This regime resembles the runaway process as it happened in the absence of a magnetic field. The picture changes when the magnetic field increases so that $\eta_o \geq \delta_o$. In this case three different types of trajectories occur depending on the initial conditions, as it shown in Fig. 5.6 along with the corresponding temporal evolution of the electron kinetic energy. In some cases an energetic electron starts in the $u_x - u_y$ plane and then rapidly losses its energy and eventually stops (top two panels of Fig. 5.6). In other cases the electron along a spiral trajectory while the electron kinetic energy rapidly increases (at $t \sim t_o$) and reaches then its steady state value after making several oscillations (Middle two panels of Fig. 5.6).

This regime is strongly different from what happened in the absence of a magnetic field where the runaway electrons reach very high energies, while in the $\mathbf{E}\perp\mathbf{B}$ field a steady state can be reached at a much smaller electron energy.

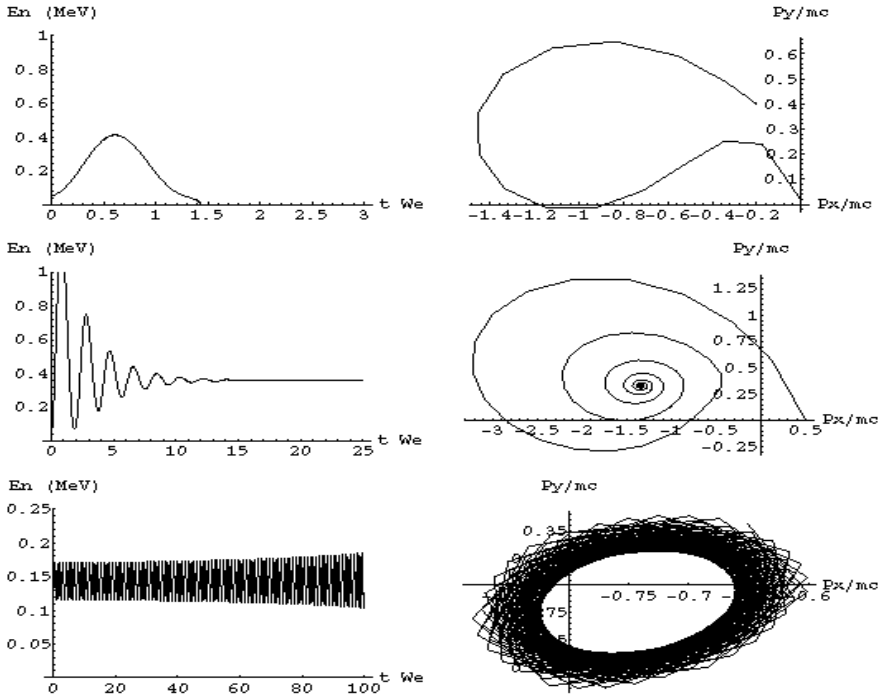

Figure 5.6: (Top two pannels) Electron trajectory in the $u_x - u_y$ plane along with the temporal evolution of its kinetic energy obtained for $\mathbf{E}\perp\mathbf{B}$ at $\delta_o = 5$, $\eta_o = 7$, and for the initial values p_x^o=0.3 and u_y^o=-0.3. (Middle two pannels) trajectory obtained at u_x^o=0.3 and u_y^o=-0.6, (Bottom two panels) trajectory obtained for $\mathbf{E}\perp\mathbf{B}$ at $\delta_o = 5$, $\eta_o = 7.5$, for the initial values u_x^o=0.3 and u_y^o=-0.65

We describe also the third kind of trajectories when the electron moves along the spiral trajectory losing its energy and eventually stops (Bottom two panels of Fig. 5.6).

This happens when the u_y momentum component reaches such negative value that the first and second terms in right part of the first of Eqs. (5.12) cancel each other ($u_y \sim -\gamma\delta_o/\eta_o$) leading to the exponential temporal decay of the u_x component. This is followed by the temporal decay of the u_y component as

comes from the second of Eqs. (5.12). However, when relativistic electrons gain and lose energy they can generate Bremsstrahlung emission, and might produce secondary runaway electrons.

We proceed by defining the separatrix as a line in the $v_x^o = v_x(t = 0)$ and $v_y^o = v_y(t = 0)$ plane which separates the initial electron velocities leading to the runaway regime from those leading to the electron deceleration in a given electric and magnetic field. This is shown in Fig. 5.7 calculated for the normalized electric field $\delta_0 = 5$, and for few different values of normalized magnetic field (η_0 = 6.0, 6.5, 7.0, and 7.5). For each of these cases the runaway process occurs for v_x^o, v_y^o located inside the domain bounded by the corresponding runaway separatrix. Note that when the applied magnetic field increases, the region of runaway shrinks. Finally, η_0 reaches the maximum value $\eta_{c0}(\delta_0)$ when the runaway ceases. In fact, at $\delta_0 = 5$ the runaway ceases at $\eta_0 = 7.8$, which is in a considerable agreement with the critical value $\delta_{c0}(\eta_0 = 7.8) = 4.9$ (see Fig. 5.5), found above by using some simplifications.

Note that a primary runaway electron is able to produce a secondary electron which also runs away, if the kinetic energy of the primary electron is at least twice that required for runaway. This is the condition of the runaway breakdown [*Gurevich et al.*, 1994]. The separatrix of runaway breakdown is obtained as it was done for the runaways, but using an additional condition that the steady state kinetic energy of the runaway electron is twice as large as its initial value. It is shown in Fig. 5.7b for the same values of electric and magnetic field as in Fig. 5.7a. Since the requirements for runaway breakdown are stronger than for just runaway, the corresponding domain is smaller than that for the runaways. In fact the runaway discharge developed at $\delta_0 = 5$ ceases if $\eta_0 > 7$.

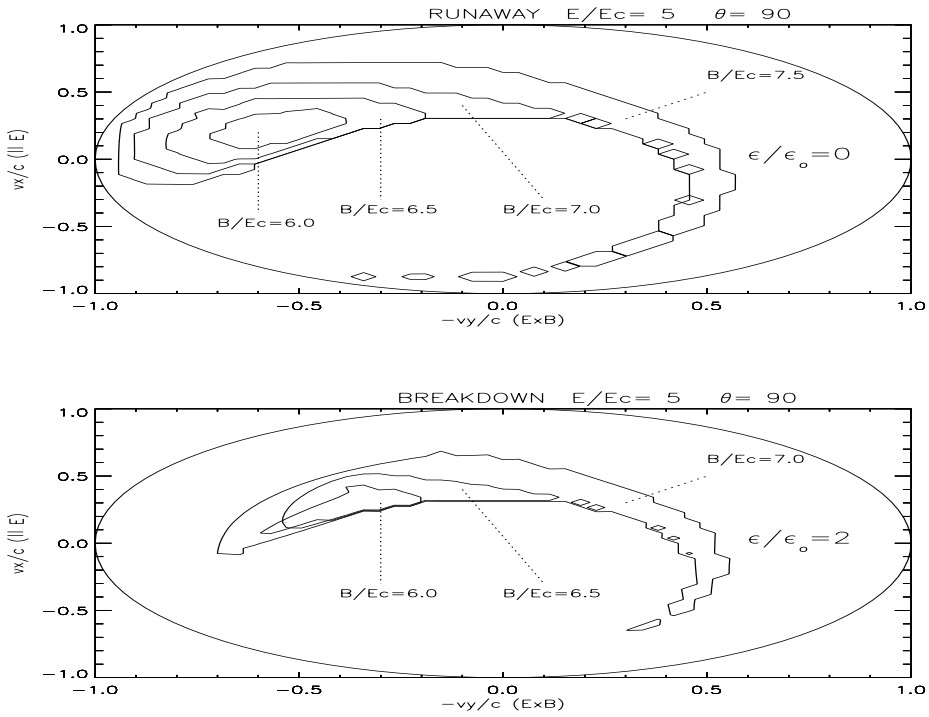

Figure 5.7: (a) Separatrix of runaway regime for $\mathbf{E}\perp\mathbf{B}$ in the (v_x^o/c, v_y^o/c) plane obtained for $\delta_0 = 5$ and $\eta_0 = 6.0$, 6.5, 7.0, and 7.5. Separatrix of runaway breakdown. (b) Same as above except using the additional condition that the steady-state kinetic energy of the runaway electron is twice as large as its initial value.

5.3.3 Spreading of the Runaway Discharge in the Presence of a Magnetic Field

We consider now the runaway discharge stimulated by a seed high energy electron. In the absence of the magnetic field the runaway discharge spreads inside a cone stretched along the direction of the electric field [*Gurevich et al.*, 1994]. Below we discuss how the magnetic field affects the structure of the runaway

discharge, and the dynamics of its spreading. We concentrate mainly on the case when the electric and magnetic field are parallel to each other. The motion of runaway electrons is studied in the spherical coordinate frame, in which both E and B vectors are directed along the x axis. The electron momentum evolves with an angle θ with the x axis, while its projection on the plane z-y evolves with an angle φ with the y axis. In this frame Eqs. (5.12) can be represented as

$$\frac{du}{d\zeta} = \gamma[\delta_o \mu - \Phi(\gamma)]$$

$$\frac{d\mu}{d\zeta} = \delta_o \gamma \frac{1-\mu^2}{u}$$

$$\frac{d\varphi}{d\zeta} = \eta_o \tag{5.13}$$

where $\mu = cos\theta$, $u = \sqrt{u_x^2 + u_y^2 + u_z^2}$, and ζ is the proper time, and $\gamma = \sqrt{1+u^2}$. Since μ is a monotone function of ζ, we can represent the trajectory in the (u, μ) plane, which is then described by the following equation

$$\frac{du(\mu)}{d\mu} = \frac{1}{\delta_o(1-\mu^2)}[\delta_o \mu - \Phi(\gamma(\mu))]$$

Therefore, μ also serves as parametrization of the problem with

$$\frac{d\zeta(\mu)}{d\mu} = \frac{u}{\delta_o \gamma (1-\mu^2)}$$

Correspondingly, the separatrix which separates in this plane the accelerating and decelerating electron trajectories is defined by the equation

$$\Phi(\gamma) = \delta_o \mu$$

Figure 5.8 shows the minimum initial electron energy required for runaway as a function of initial electron direction μ. This is calculated for a few different

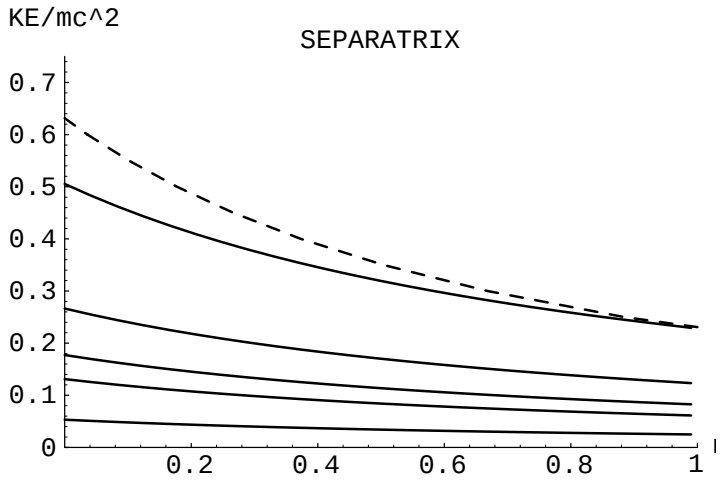

Figure 5.8: Minimum electron energy required for runaway at E||B, versus the direction of the initial electron $\mu = cos\theta$. Obtained at $\delta_0 = 2$, 3, 4, 5, and 10. Shown by a dashed line is the analytical approximation obtained at $\delta_0 = 2$ [Roussel-Dupre et al., 1994].

values of the normalized electric field (δ_o= 2, 3, 4, 5 and 10). Shown by a dashed trace is the same separatrix obtained by *Gurevich et al.* [1994] for δ_o= 2.

We consider next the diffusion of runaway electrons which occurs in the plane perpendicular to **E**, and caused by the fact that secondary electrons appear at an arbitrarily angle. As a result of this diffusion the runaway discharge caused by a single seed electron acquires a conical shape as shown by *Gurevich et al.*, [1994] in the absence of magnetic field. The runaway electron possesses two velocity components in the (y, z) plane

$$\mathrm{u}_z = \frac{d\widetilde{z}}{d\zeta} = u\sqrt{1-\mu^2}\,\sin\varphi$$

$$\mathrm{u}_y = \frac{d\widetilde{y}}{d\zeta} = u\sqrt{1-\mu^2}\,\cos\varphi$$

where y, z are given in the dimensionless units, $\widetilde{y} = y/c\tau_c$, $\widetilde{z} = z/c\tau_c$. In order to obtain the mean free path of the runaway electron we integrate this two

equations using Eq. (5.13), and take into account that the secondary electron which is born at the spot μ_o close to separatrix propagates freely till the spot μ_1, when its energy increases to twice its initial value. Therefore we have

$$r_\mu^2 = (\overline{\Delta\widetilde{y}})^2 + (\overline{\Delta\widetilde{z}})^2$$

$$\Delta\widetilde{y} = \int_{\mu_o}^{\mu_1} \frac{u(\mu)^2}{\delta_o\sqrt{1+u(\mu)^2}} \frac{\sin(\varphi_o + \eta_o\zeta(\mu))}{\sqrt{1-\mu^2}} d\mu$$

$$\Delta\widetilde{x} = \int_{\mu_o}^{\mu_1} \frac{u(\mu)^2}{\delta_o\sqrt{1+u(\mu)^2}} \frac{\cos(\varphi_o + \eta_o\zeta(\mu))}{\sqrt{1-\mu^2}} d\mu$$

where $\varphi_o = \varphi(t=0)$ and the bar shows averaging over φ_o. The characteristic time Δt needed for electron to propagate from point μ_o to μ_1 can be obtained from Eq. (5.13) as

$$\Delta t = \int_{\mu_o}^{\mu_1} \gamma \frac{d\zeta}{d\mu} d\mu = \tau_c \int_{\mu_o}^{\mu_1} \frac{u(\mu) d\mu}{\delta_o(1-\mu^2)}$$

The diffusion coefficient D is then found to be

$$D = (c^2\tau_c)\frac{r_\mu^2}{2\Delta t}$$

where the factor of 2 is due to the averaging over φ_o, and the result is shown in Fig. 5.9 for different values of electric and magnetic fields. Note that in the absence of magnetic field our results coincide with that obtained by *Gurevich et al.* [1994]. Figure 5.9 reveals that the magnetic field reduces the diffusion coefficient and confines the runaway discharge. The confinement is the only effect caused by the magnetic field parallel to the electric field, since the magnetic field cannot affect the electron kinetic energy. Note that if the magnetic field is directed at a certain angle to the electric field, the runaway discharge acquires the shape of the cone having an elliptical cross section in the plane perpendicular to **E**. The semimajor axis is directed parallel to the projection of **B** on this plane, while the small semiaxis is perpendicular to this projection.

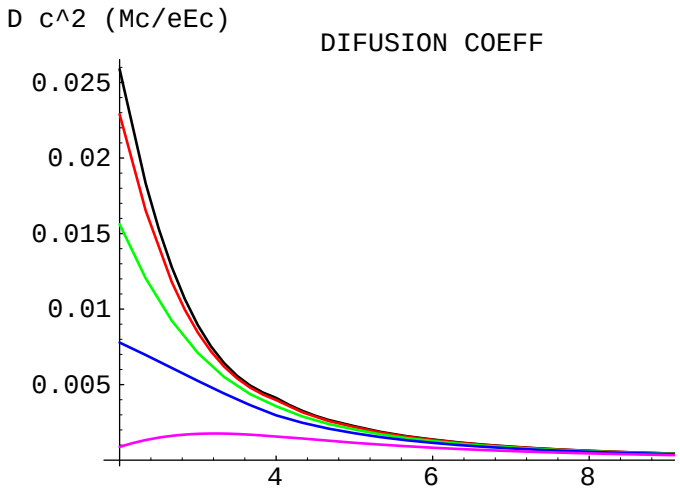

Figure 5.9: Dimensionless diffusion coefficient in the plane perpendicular to $E||B$ obtained at $\eta_o = 0$, 1, 2, 3, and 5 as a function of δ_0.

5.3.4 Electron Runaway Under an Arbitrary Angle Between Electric and Magnetic Fields

In a general case when the angle between the vectors **E** and **B** is $0 < \theta_o < 90$, three different ranges of the angle θ_o were distinguished based on the physical properties of the runaway process. They are illustrated by the runaway trajectories shown in Figs. 5.10a, 5.10b, 5.10c obtained for different θ_o.

If the angle θ_o ranges between 80^o and 90^o the runaway process differs significantly from that which occurs in the absence of the magnetic field. First, it develops only if the ratio E/B is greater than a certain threshold value, as was shown in Section 2. Second, contrary to the runaway electrons in the absence of the magnetic field where the energy gain is almost unlimited [*Roussel-Dupre et al.*, 1994], runaway electrons at $80\ ^o < \theta_o < 90^o$ reach a steady state, at which

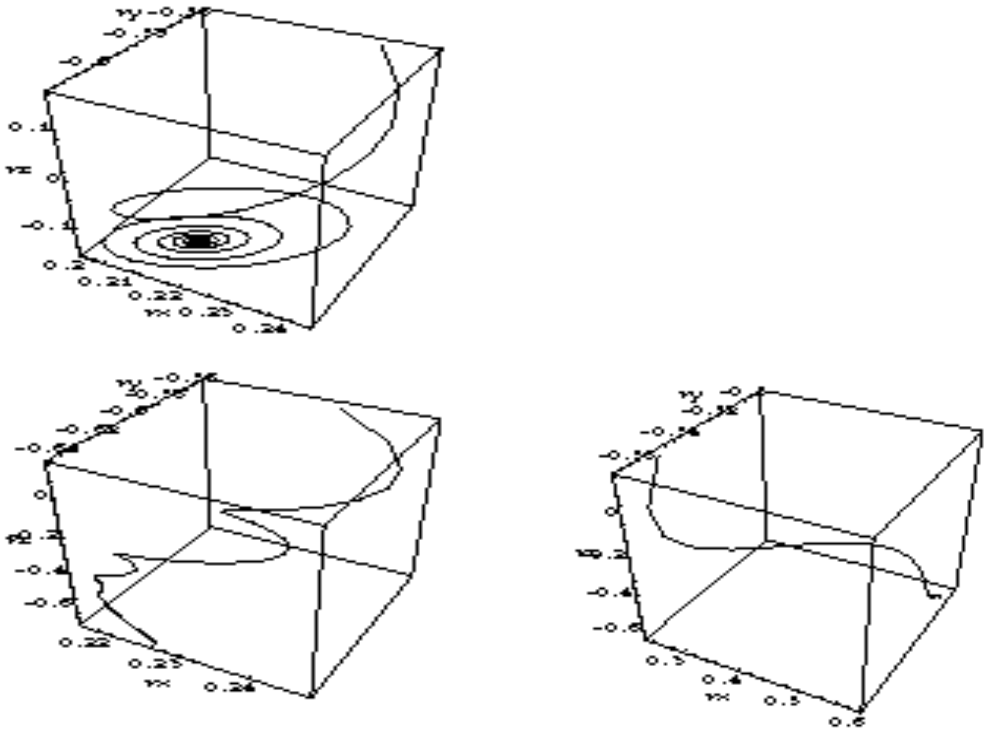

Figure 5.10: Trajectories of runaway electron in $(u_x, u_{y,}u_z)$ space obtained at δ_0 = 5, 0 = 7.5, for the initial conditions u_x^o=0.3, u_y^o=-0.2, u_z^o=0.2 , and for different angle θ_o between the electric and magnetic fields: a) θ_o = 85, b) θ_o = 80, c) θ_o = 6 0.

point they orbit across the magnetic field with a constant kinetic energy, as it is shown in Fig. 5.10a obtained for θ_o= 85^o.

In the range of $0^o < \theta_o < 60^o$ the runaway process resembles that which occurs in the absence of magnetic field, namely the electrons are moving along the direction of the magnetic field driven by a $E_{||}$ component of the electric field. This is illustrated by Fig. 5.10b, obtained at θ_o= 60^o. The latter resembles a trajectory which is almost a straight line in the $(p_x, p_{y,}p_z)$ space with a small effect of magnetic field at low momentum. However, in this case the magnetic

field manifests itself by confining the runaway process, as discussed in Section 4.

In the transient range $60^o < \theta_o < 80^o$ the runaway electron trajectories are twisted by the magnetic field when the electrons start the acceleration and have relatively low energy. The electron then gains energy along a straight trajectory, as shown by Fig. 5.10c obtained at $\theta_o = 80$.

The effect caused by the angle between the electric and magnetic fields on the runaway process is also illustrated by Fig. 5.11, which reveals the kinetic energy of a runaway electron as a function of the angle θ_o. The kinetic energy was calculated for same initial conditions, and for the time equal to that required to reach a steady state at θ_o=90^o. Note that $\epsilon_{kin}(\theta_o = 90)/\epsilon_{kin}(\theta_o = 0)$ has a small, but finite value, in fact at $\delta_o = 5, \eta_o = 7.5$ it is of the order of 10^{-2}.

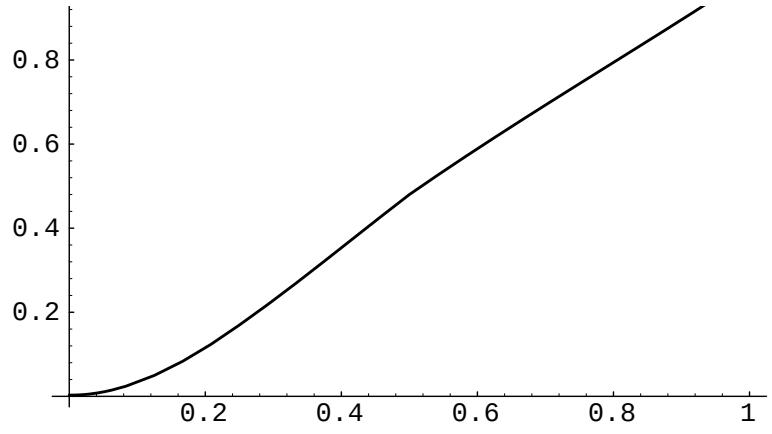

Figure 5.11: Kinetic energy of the runaway electron as a function of the angle $cos\theta_o$, obtained at $\delta_o = 5$, $\eta_o = 7$ and at initial values p_x^o=0.3, p_y^o=-0.2, p_z^o=0.2.

Figure 5.11 shows that at $\cos\theta_o > 0.5$ (i.e. $\theta_o < 60^o$) the runaway is driven mostly by the $E_{||} = E\cos\theta_o$ component of the electric field, and it is not strongly different from that which occurred in the absence of a magnetic field; while at 0 $<$ cos $\theta_o < 0.16$ (i.e. at $80^o < \theta_o < 90^o$) the effect of the magnetic field becomes

very important; and at $0.16 < \cos\theta_o < 0.5$ (i.e. at $60^o < \theta_o < 80^o$) a transient region between these two regimes exists.

The runaway boundary for an arbitrarily angle θ_o could also be investigated using the following approach. We consider an ensemble of N_0 electrons moving in air in the presence of electric and magnetic fields. The electrons which don't interact with each other, are uniformly distributed in space, as well as in the energy range, which we consider for definiteness as $1 < \gamma < 3.2$. The trajectories of the electrons were studied using Eqs. (5.12), and the trajectories which take electrons to higher energy were then distinguished from those which lead to zero energy. Figure 5.12 reveals the fraction of electrons, N/N_0, that runaway, as a function of δ_0. The calculation was made for the angle $\theta_o = 90^o$, and from left to right the value of η_0 changes from 0 to 10 with the step 1. In the absence of magnetic field, shown by the very left trace, the separatrix resembles that obtained by *Roussel-Dupre et al.* [1994], while the increase of the magnetic field leads to the significant reduction in the fraction of runaway electrons.

Finally, knowing the electron runaway boundary, one can find the characteristic ionization time in the discharge caused by the runaway electrons by using the fluid approximation, assuming that the electron distribution function is a delta-function, i.e. consider a monoenergetic flux of electrons. Note that of particular interested is the production rate of secondary runaway electrons, since their production leads to the development of the runaway breakdown.

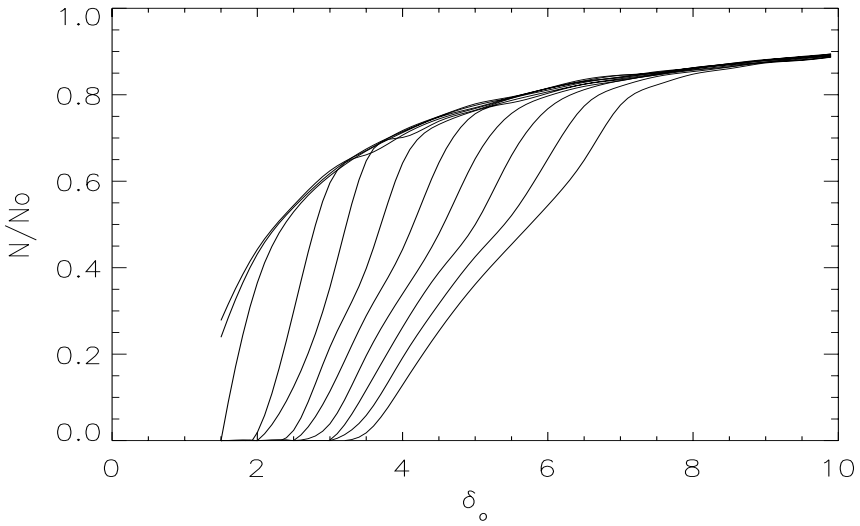

Figure 5.12: Fraction of runaway electrons as a function of the electric field δ_o obtained for different values of the magnetic field η_o, at β=90. From left to right the value of η_o changes from 0 to 10 with a step of 1.

5.4 Importance of B Field

We state now the main features regarding the behavior of runaway electrons in the constant magnetic field.

- 1. When the magnetic field is less than the critical field $\eta_o = B/E_{c0} < 1$ the affect of the magnetic field on the electron runaway is almost negligible.

- 2. The value of the threshold electric field E_η required for the electron runaway in the presence of a magnetic field increases with the increase of η_0 (see Fig. 5.5). For high values of $\eta_0 \gg 1$ the threshold field always tends to the constant value

$$E_\eta = E_{c0}/\cos\theta_o$$

where θ_o is the angle between **E** and **B**. This equation shows that at $\eta_0 \gg 1$ the threshold electric field increases with θ_o, which means that conditions of runaways are hindered.

- 3. In a case of perpendicular **E** and **B** fields, the value of threshold electric E_η field increases smoothly with η_o :

$$E_\eta \sim \eta_o^{2/3} E_{c0}$$

Since the critical field E_{c0} is approximately an order of magnitude less than the threshold of the conventional breakdown, it follows from the last equation that in a case of perpendicular electric and magnetic fields the runaway breakdown is hardly possible if $\eta_o \geq 30$.

In conclusion, the role played by the geomagnetic field in the runaway process discussed above for heights less than 20 km is negligible. Nevertheless the geomagnetic field plays a noticeable role at heights which ranges from 20 to 30 km. In fact, it significantly changes the threshold electric field E_η for $\theta_o \geq 45^o$. At the height above 40 km the effect of geomagnetic field dominates at large angles θ_o and the conditions of runaway breakdown becomes even more hindered.

Therefore at high altitudes, (z > 40 km) for angles θ_o between **E** and **B** close to $\pi/2$, the runaway breakdown is hindered, while for $\theta_o \simeq 0$ between **E** and **B**, the runaway process can proceed freely. Thus taking into consideration that the static electric field due to thunderclouds is directed almost vertically one can expect a significant difference in the parameters of high altitude discharges as they occur in the equatorial and midlatitudes.

Finally, we obtained the runaway separatrix which separates momentum space into two regimes: those electrons which possess trajectories that take

them into higher energies, and other electrons which possess trajectories leading to zero energy. Using this separatrix, the characteristic ionization time required for the creation of a secondary runaway electron can be estimated.

Part IV

conclusions

Chapter 6

Conclusions

The objective of this thesis is to provide the physics framework within which some of the observed high altitude lightning phenomena can be studied and quantitatively understood and modeled. These HAL phenomena represent clear evidence of the lightning induced energy dissipation in the lower ionosphere during a low altitude thunderstorm. The lightning energy can be coupled to the upper atmosphere by a multitude of processes such as electromagnetic pulses and runaway beams. In this thesis we studied the properties of these processes as related to HAL.

6.1 Electromagnetic Pulses

Electromagnetic pulses (EMP), as generated from our fractal lightning models, can energize the electrons in the lower ionosphere, inducing electronic transitions, as they collide with the molecules in the lower ionosphere. These electronic transitions are then followed by emissions, which are termed red sprites. The theoretical understanding of the red sprites including energy deposition was the subject of three recent publications which considered the lightning induced

electric fields as produced by horizontal [*Milikh et al.,* 1995] or vertical [*Pasko et al.*, 1995, *Rowland et al.,* 1995] dipole electric models. The models were able to account for the energetics of the sprites, but produced highly homogeneous and smooth electron heating in the lower ionosphere resulting in the absence of internal structure in the optical emissions. At the same time, *Winckler et al.* [1996] conducted a detailed study of the spatial structure of sprites with the conclusion that an extremely important characteristic of red sprites is their fine spatial structure, sometimes even down to the detector resolution. Furthermore, the threshold current and dipole moment requirements of all three models have been criticized as unrealistically large [*Uman, unpublished comment,* 1995].

We presented a novel model of red sprites, the first model to account for the fine structure of the sprites, that is based on the fact that the low altitude lightning has a fractal structure which is reflected in the subsequent spatially dependent optical emission pattern.

We conducted an extensive analysis of fractal antennae to study their properties as compared with dipole type of models. The most important results seems to suggest that by having a power law distribution of phases a fractal antennae can give a considerable increase in the radiated power density, sometimes by a factor of 10, as compared with equivalent dipole models. Such increase in the power density can be of extreme relevance to the modeling of red sprites. Furthermore, fractal antennae can naturally give a spatially structured radiation pattern. The radiation pattern depends on the structure of the discharge, but we expect, as seen from simple fractal models, that the most relevant parameter in determining the spatially dependent radiation pattern is the dimension of the self-similar fractal.

We applied the concept of fractal antennae to the sprite phenomena. Lightning was modeled as a self-similar fractal discharge from which the fields in the lower ionosphere were computed, including self-absorption. The kinetic treatment of the energy deposition and the optical emissions were computed with the help of a Fokker-Planck code [*Tsang*, 1991]. Beside the trivial parameter I_o and Q and β, we also found that the electric field power density and the structure of the optical emissions is critically dependent on the dimension D of the discharge. These models suggest that we can obtain realistic emission intensities with a current threshold of $I_o \sim 100$ kA (hence a $Q \sim 100$ C) for a particular discharge model, e.g. $\eta = 3$ and for $n_f \geq 50$. Fractal discharges of different dimensions have varying discharge parameter thresholds, but in general a sprite is generated with $I_o \geq 100$ kA. This results seems to agree well with the sprite occurrence [*Lyons,* 1994] and the statistics of lightning discharge parameters [*Uman*, 1987]. The statistical relevance must be compared more closely with sprite occurrences and intracloud discharges.

We also constructed a model of the red sprite spectrum due to molecular excitation by ionospheric electrons accelerated by the lightning induced electric field. A valuable output of the model is the scaling of the relative intensities of the emissions with the value of the electric field and/or power density. Such scaling can provide additional constraints to the required energy deposition in the red sprite region by comparing with spectrum measurements. Proper account was done of the wavelength dependent atmospheric attenuation. In principle, the model could yield the spatial profile of the amplitude of the electric field in the emission region from spatially resolved measurements of the spectrum. The model also reveals some differences between the aurora and sprite spectra: in the

aurora both permitted and forbidden transitions play a noticeable role, while in sprites only permitted transitions are important. Finally, it seems that sprites are produced by electrons of much lesser energy than that of auroral electrons.

6.2 Runaway Beams

A new type of electrical air breakdown, called runaway breakdown or runaway discharge, was discussed recently by *Gurevich et al.* [1992] and applied to the preliminary breakdown phase of a lightning discharge. If the local electric field is large enough an electron breakdown, or runaway, discharge can be created. It is often assumed that these energetic electron beams may be related to some of the other phenomena related to HAL: blue jets, gamma ray burst, radio burst pairs. The biggest issue related with runaway discharges is the fact that these phenomena seem to be occurring at heights where the magnetic field effects must be included. But when the magnetic field is incorporated in the equations, the field threshold conditions for the creation of the electron beams is substantially changed.

Therefore, we have developed the theory of the runaway beam in the presence of static electric and magnetic fields. The role played by the geomagnetic field in the runaway process for heights less than 20 km is negligible. Nevertheless the geomagnetic field plays a noticeable role at heights which ranges from 20 to 30 km. In fact, it significantly changes the threshold electric field E_η for $\theta_o \geq 45^o$, where θ_o is the angle between the **E** and **B** fields. At the height above 40 km the effect of the geomagnetic field dominates at large angles θ_o and the conditions for runaway breakdown becomes even more hindered.

Thus taking into consideration that the static electric field due to thunderclouds is directed almost vertically, one can expect a significant difference in the parameters of high altitude discharges as they occur in the equatorial and midlatitude regions. Close to the equator, $\theta_o \sim \pi/2$, and for high altitudes, ($z > 40$ km), the runaway breakdown is hindered. While at midlatitudes, for $\theta_o \leq 45$, the runaway process can proceed freely. Such observations put strong constraints on the type of models needed to explain these high altitude phenomena. At least close to the equator extremely large field may be required since the runaway process is substantially hindered at the relevant heights.

We have computed the basin of acceleration in the electron momentum phase space as the relative importance of the electric and magnetic fields are varied, giving an idea of the relative feasibility in producing the runaway avalanche. To get an idea of the importance of the diffusion process in the runaway discharge, we have computed the diffusion coefficient in the presence of the magnetic field in terms of quadratures for the specific case that E and B are parallel.

It seems that the runaway process is not energetically efficient to produce red sprites due to the height in which they occur, where the B field of the Earth would hindered the process. Even though we expect that the runaway process is ultimately responsible for the blue jets and gamma ray bursts, it is not clear yet what are the specifics of the phenomena. The work must continue.

6.3 Implications to Future Work

From the results developed in this thesis we propose a few directions in which to continue the work.

The latest observations of sprites reveal filaments that can be described as streamers propagating down from the main body of the sprite (see Fig. 6.1) with a cross-sectional diameter of 100 m or less. Given the nucleated spatial structure in the conductivity produced by the fractal lightning discharge, the streamers would start naturally in the presence of a laminar field. Therefore, a more comprehensive model of red sprites that includes both the laminar and electromagnetic lightning induced fields and their effects in the lower ionosphere can be developed from a model that solves the nonlinear wave equation, Eq. (B.2), and includes ionization and charge separation. Furthermore, the streamers will strongly influence the red sprite spectra.

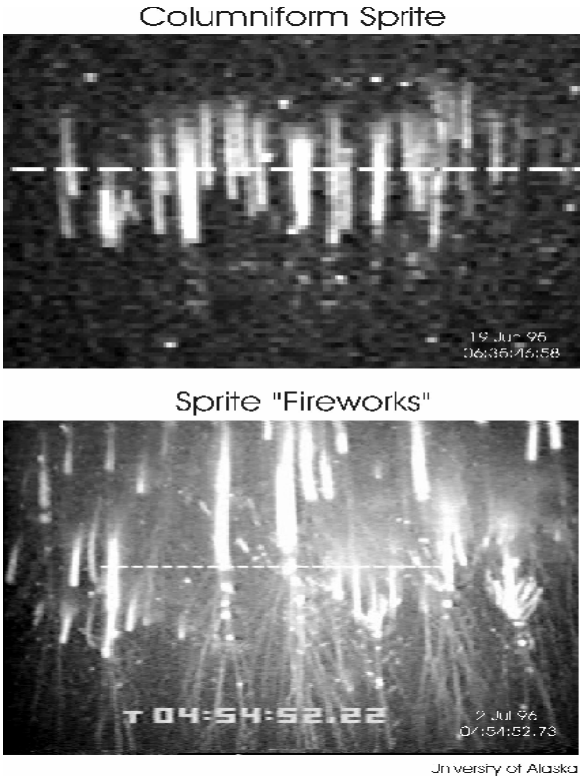

Figure 6.1: A sprite. The picture shows clear streamers, or filaments, that reach downward from the main body of the sprite.

There is still no comprehensive theory for blue jets, gamma ray flashes and radio bursts. We expect that these phenomena are ultimately related to runaway beams, but the analysis must include the magnetic field. We should develop the proper kinetic theory of runaway discharges in the presence of a magnetic field by solving selfconsistently the Boltzmann equation, Eq. (5.5), in 3D momentum space. Besides its general scientific interest, it is expected that such analysis will be extremely relevant for the understanding of blue jets, gamma ray flashes and radio bursts.

Part V

Appendices

Appendix A

Fields from a Fractal Structure

The fields from a line element can be solve with the help of the Hertz Vector [*Marion and Heald*, 1980]. In order to solve Maxwell's equations we define, in empty space, the vector function $\mathbf{Q}$ [*Marion and Heald*, 1980] that is related to the current density $\mathbf{J}$ and the charge density ρ as

$$\mathbf{J} = -\frac{\partial \mathbf{Q}}{\partial t}$$

$$\rho = \nabla \cdot \mathbf{Q}$$

Note that $\mathbf{Q}$ solves the continuity equation trivially, and furthermore, it can be used to define another vector function, namely the Hertz vector $\mathbf{\Pi}(\mathbf{x}, t)$, as

$$\nabla^2 \mathbf{\Pi} - \frac{1}{c^2}\frac{\partial^2 \mathbf{\Pi}}{\partial t^2} = -4\pi \mathbf{Q}$$

where the fields are then defined as

$$\mathbf{B}(\mathbf{x}, t) = \frac{1}{c}\nabla \times \frac{\partial \mathbf{\Pi}(\mathbf{x}, t)}{\partial t}$$

$$\mathbf{E}(\mathbf{x}, t) = \nabla \times \nabla \times \mathbf{\Pi}(\mathbf{x}, t)$$

The time-Fourier transformed Maxwell's equations, with $\mathbf{Q}(\mathbf{x},\omega) = \frac{i}{\omega}\mathbf{J}(\mathbf{x},\omega)$ and $\mathbf{J}(\mathbf{x},\omega) = \widehat{\mathbf{L}}\mathrm{I}(l,\omega)$, can be solved with the help of the Hertz vector $\mathbf{\Pi}$,

$$\mathbf{\Pi}(\mathbf{x},\omega) = \frac{i}{\omega}\int_0^L \mathbf{J}(l,\omega)\frac{e^{ik\left\|\mathbf{x}-l\widehat{\mathbf{L}}\right\|}}{\left\|\mathbf{x}-l\widehat{\mathbf{L}}\right\|}dl \tag{A.1}$$

where the line element has orientation $\mathbf{L}$ and length L, and is parametrized by $l \in [0, L]$. Values with the hat ^ indicate unit vectors, variables in bold indicate vectors, ω is the frequency, $k = \frac{\omega}{c}$. The time dependence can be found by inverting the above equation.

A.1 Fields from a Fractal Antennae

A current pulse propagates with speed $\beta = \frac{\mathrm{v}}{c}$ along a fractal structure. At the n^{th} line element with orientation $\mathbf{L}_n$ and length L_n, which is parametrized by $l \in [0, L_n]$, the current is given by $I(l, s_n, t) = I_o(t - \frac{s_n+l}{\mathrm{v}})$ where s_n is the path length along the fractal (or if you prefer a phase shift). The radiation field is the superposition, with the respective phases, of the small line current elements that form the fractal. For a set $\{\mathbf{r}_n, \mathbf{L}_n, I(s_n,t)\,|\,n = 0, ..., N\}$ of line elements, such as shown in the example diagram of Fig. A.1, the Hertz vector is given by

$$\mathbf{\Pi}(\mathbf{x},\omega) = \sum_{\{n\}}\widehat{\mathbf{L}}_n\frac{i}{\omega}\int_0^{L_n}\mathrm{I}_o(\omega)e^{i\frac{\omega}{\mathrm{v}}(s_n+l)}\frac{e^{ik\|\mathbf{r}_n-l\widehat{\mathbf{L}}_n\|}}{\|\,\mathbf{r}_n - l\widehat{\mathbf{L}}_n\,\|}dl \tag{A.2}$$

where $\mathbf{r}_n$ is the vector from the beginning of the n^{th} line element to the field position $\mathbf{x}$, ω is the frequency and $k = \frac{\omega}{c}$.

We must realize that in general Eq. A.2 for $\mathbf{\Pi}$ is very complicated, but we are interested in the far field of the small line elements ($r_n \gg L$). Therefore, we can take the far field approximation of the small line elements to obtain a closed

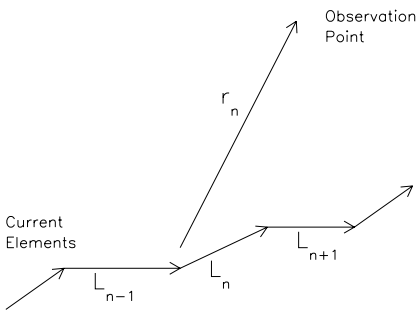

Figure A.1: A diagram that explains all the variables and coefficients

form solution for the Fourier transformed fields as

$$\mathbf{B}(\mathbf{x},\omega) = -\sum_{\{n\}} \frac{k^2 e^{ikr_n}}{r_n} f(s_n,\omega,r_n)[1+\frac{i}{(kr_n)}](\widehat{\mathbf{L}}_n \times \widehat{\mathbf{r}}_n)$$

$$\mathbf{E}(\mathbf{x},\omega) = -\sum_{\{n\}} \frac{k^2 e^{ikr_n}}{r_n} f(s_n,\omega,r_n)[(1+\frac{i}{(kr_n)}+\frac{i^2}{(kr_n)^2})\widehat{\mathbf{L}}_n$$
$$-\widehat{\mathbf{r}}_n(\widehat{\mathbf{L}}_n\cdot\widehat{\mathbf{r}}_n)(1+\frac{3i}{(kr_n)}+\frac{3i^2}{(kr_n)^2}]$$

where the geometric factor is given by

$$f(s_n,\omega,r_n) = \frac{i}{\omega}\int_0^{L_n} I_o(s_n,l,\omega)e^{-i(\widehat{\mathbf{L}}_n\cdot\widehat{\mathbf{r}}_n)kl}dl = \frac{ie^{i\frac{c}{v}s_n}}{\omega} I_o(\omega)\int_0^{L_n} e^{i(\frac{c}{v}-(\widehat{\mathbf{L}}_n\cdot\widehat{\mathbf{r}}_n)k)l}dl$$

$$f(s_n,\omega,r_n) = \frac{\beta I_o(\omega)e^{i\frac{\omega}{v}s_n}}{ck^2(1-\beta(\widehat{\mathbf{L}}_n\cdot\widehat{\mathbf{r}}_n))}(1-e^{i(\frac{c}{v}-(\widehat{\mathbf{L}}_n\cdot\widehat{\mathbf{r}}_n)k)L_n})$$

Note that even though we are in the far field of the small line elements, we can be in fact in the intermediate field with respect to the global fractal structure. Therefore, phase correlations over the fractal can be extremely relevant, and produce spatially nonuniform radiation fields. We then invert the Fourier transform of the field to real time and obtain the spatio-temporal radiation pattern due to

the fractal discharge structure

$$\mathbf{B}(\mathbf{x},t)=\sum_{\{n\}}\frac{-(\widehat{\mathbf{L}}_n\times\widehat{\mathbf{r}}_n)}{cr_n(\frac{c}{\mathrm{v}}-(\widehat{\mathbf{L}}_n\cdot\widehat{\mathbf{r}}_n))}[I_o(\tau)\mid_{t-\tau_2}^{t-\tau_1}+\frac{c}{r_n}I_1(\tau)\mid_{t-\tau_2}^{t-\tau_1}]$$

$$\mathbf{E}(\mathbf{x},t)=\textstyle\sum_{\{n\}}\frac{1}{cr_n(\frac{c}{\mathrm{v}}-(\widehat{\mathbf{L}}_n\cdot\widehat{\mathbf{r}}_n))}[(I_o(\tau)\mid_{t-\tau_2}^{t-\tau_1}+\frac{c}{r_n}I_1(\tau)\mid_{t-\tau_2}^{t-\tau_1}+\frac{c^2}{r_n^2}I_2(\tau)\mid_{t-\tau_2}^{t-\tau_1})\widehat{\mathbf{L}}_n-$$
$$\widehat{\mathbf{r}}_n(\widehat{\mathbf{L}}_n\cdot\widehat{\mathbf{r}}_n)(I_o(\tau)\mid_{t-\tau_2}^{t-\tau_1}+\frac{3c}{r_n}I_1(\tau)\mid_{t-\tau_2}^{t-\tau_1}+\frac{3c^2}{r_n^2}I_2(\tau)\mid_{t-\tau_2}^{t-\tau_1})] \tag{A.3}$$

where

$$I_1(t)=\int_{-\infty}^{t}d\tau I_o(\tau)$$
$$I_2(t)=\int_{-\infty}^{t}d\tau\int_{-\infty}^{\tau}d\tau^{'}I_o(\tau^{'})$$

can be calculated exactly for the current described above, and where

$$\tau_1=\frac{r_n}{c}+\frac{s_n}{\mathrm{v}}$$
$$\tau_2=\frac{r_n+(\widehat{\mathbf{L}}_n\cdot\widehat{\mathbf{r}}_n)L_n}{c}+\frac{s_n+L_n}{\mathrm{v}}+(\widehat{\mathbf{L}}_n\cdot\widehat{\mathbf{r}}_n)\frac{L_n}{c}$$

The value of τ_1 and τ_2 correspond to the causal time delays from the two end points of the line element.

Before finishing this section we want to mention that there is an inherent symmetry in the radiation fields. In general we will assume that the current is given by $I(t)=I_oe^{-\alpha t}(1-\cos(2\pi n\alpha t))\theta(t)$ where $\theta(t)$ is the step function, and $n\geq 1$. Note that the total charge discharged by this current is Q=I_o/α where $1/\alpha$ is the decay time of the current. But since the current propagates along the fractal, the radiation fields at a given position in space will last for a time given by $\tau=\frac{s}{\mathrm{v}}+\alpha$ where s is the largest path length along the fractal. The fields are invariant as long as αt , $\frac{L\alpha}{\mathrm{v}}$ and $\mathbf{r}\alpha$ are kept constant in the transformation. Such scaling can become relevant in studying the properties of radiation fields from fractal antennae.

In general we will use the power density $S(W/m^2) = c\varepsilon_o E^2(V/m)$, where $1/c\varepsilon_o$ is the impedance of free space, as a natural description for the amount of power radiated through a cross-sectional area.

A.2 The Far field

The far field is approximately given by

$$\mathbf{E}(\mathbf{x},t) = \sum_{\{n\}} \frac{\beta I_o(\tau)\,|_{t-\tau_2}^{t-\tau_1}}{cr_n(1-\beta(\hat{\mathbf{L}}_n\cdot\hat{\mathbf{r}}_n))} \tag{A.4}$$

In general we are going to use a current pulse defined as $I(t) = I_o(e^{-\alpha t} - e^{-\gamma t})(1+\cos(\omega t))\theta(t)$ with $\omega = 2\pi\alpha n_f$ and $\theta(t)$ as the step function. Here n_f represent the number of oscillations during the decay time scale $1/\alpha$. We chose the decay parameters as $\alpha = 10^3$ s^{-1} and $\gamma = 2\times 10^5$ s^{-1}, hence $\gamma/\alpha = 200$, which correspond to realistic parameters for lightning [*Uman*, 1987].

As a measure of the amount of energy radiated to a given point in the far field, we can define an array factor as $R(x,y,z) \sim \alpha\int E^2 dt$. From Eq. (A.4) we can write this array factor as

$$R \simeq \frac{\beta^2\zeta^2}{4(4+5\zeta^2+\zeta^4)}\sum_{n,m}\frac{\hat{\mathbf{L}}_n\cdot\hat{\mathbf{L}}_m\ \mathrm{I}_n\mathrm{I}_m}{(1-\beta a_n)(1-\beta a_m)r_n r_m}\{f[\left|\tau_n^f-\tau_m^f\right|,\zeta]+$$
$$f[\left|\tau_n^i-\tau_m^i\right|,\zeta]-f[\left|\tau_n^f-\tau_m^i\right|,\zeta]-f[\left|\tau_n^i-\tau_m^f\right|,\zeta]\} \tag{A.5}$$

$$f[\tau,\zeta] = e^{-\tau}[2+2\zeta^2+(\zeta^2-2)\cos(\zeta\tau)+3\zeta\sin(\zeta\tau)]$$

where $\tau_n^i = \alpha(\frac{r_n}{c}+\frac{s_n}{\mathrm{v}})$ corresponds to the parameters from the beginning (i) of the line element, and similarly for the endpoint (f). Also $\zeta = 2\pi n_f$ and I_n is

the current strength of the nth element. The array factor can be normalized by maximum in the array factor corresponding to the single dipole, i.e.,

$$R_o \simeq \frac{\beta^2 \mathrm{I}_o^2 \, A}{4(1-\beta a)^2 h^2}$$

where $A = \{\frac{3\zeta^4 - \zeta^2 f[\frac{1}{\alpha v}(\beta \Delta r - L), \zeta]}{2(4+5\zeta^2+\zeta^4)}\} \simeq 1$, with $\Delta r \simeq L\hat{\mathbf{x}} \cdot \hat{\mathbf{r}}$ as the difference in distance between the beginning and end points of the dipole to the detector position. h is the height of the detector.

Appendix B

Absorption and Emissions

Once we have the fractal discharge structure, we must consider the propagation of the lightning related electromagnetic fields in the lower ionosphere. As the field propagate into lower ionosphere self-absorption must be considered. The fields energize the electrons generating highly non-Gaussian electron distribution functions. The electron energization is computed with the help of a Fokker-Planck code. This Fokker-Planck code include inelastic loses due to collisions with the neutrals. This is how the fields give energy to the medium. Such inelastic losses will produce the emissions. The present model consists of a plasma formation simulation and a field propagation simulation. Together they calculate self-consistently the propagation through the ionosphere by electromagnetic fields due to the lightning discharge, which for our purposes is fractal.

B.1 Self-Absorption

As the lightning related fields propagate in the upper atmosphere and lower ionosphere, the field changes the properties of the medium by heating the electrons and therefore inducing self-absorption. The electromagnetic field propagation is

described by Maxwell's equations. We closely follow [*Gurevich* 1978] and write Maxwell's equations as

$$\nabla \times \mathbf{B} = \frac{4\pi}{c}\mathbf{J} + \frac{1}{c}\frac{\partial \mathbf{E}}{\partial t}$$

$$\nabla \times \mathbf{E} = -\frac{1}{c}\frac{\partial \mathbf{B}}{\partial t}$$

$$\nabla \cdot \mathbf{D} = 4\pi\rho$$

$$\nabla \cdot \mathbf{B} = 0$$

this form will be specially relevant for our further studies. The medium is incorporated as

$$\mathbf{D} = \hat{\varepsilon}\mathbf{E} \qquad \mathbf{J} = \hat{\sigma}\mathbf{E} + \frac{\partial}{\partial t}(\frac{\hat{\varepsilon}-1}{4\pi}\mathbf{E}) \tag{B.1}$$

where $\hat{\sigma}$ and $\hat{\varepsilon}$ are the conductivity and dielectric operators of the plasma, and in general depend on the field $\mathbf{E}$. The nonlinear wave equation describing E is then given by

$$\nabla^2\mathbf{E} - \nabla(\nabla \cdot \mathbf{E}) - \frac{4\pi}{c^2}\frac{\partial}{\partial t}(\hat{\sigma}\mathbf{E}) - \frac{1}{c^2}\frac{\partial^2}{\partial t^2}(\hat{\varepsilon}\mathbf{E}) = 0 \tag{B.2}$$

Suppose we can assume that $\hat{\sigma}$ and $\hat{\varepsilon}$ reach a steady state faster than the relevant time evolution of Eq. (B.2), as it will occur in our case, then a wave incident at the boundary preserves the frequency ω [Gurevich 1978]. In this approximation the wave equations simplifies as

$$\nabla^2\mathbf{E} - \nabla(\nabla \cdot \mathbf{E}) + \frac{\omega^2}{c^2}(\hat{\varepsilon} + \frac{4\pi i}{\omega}\hat{\sigma})\mathbf{E} = 0$$

To get an idea of how the field propagates through the plasma we make the following assumptions: (1) we take $\hat{\varepsilon} = \hat{\varepsilon}(z, E)$ and $\hat{\sigma} = \hat{\sigma}(z, E)$, (2) $|\hat{\varepsilon}| \gg |\frac{4\pi}{\omega}\hat{\sigma}|$. Furthermore, if we assume a normal polarization of the wave, we then obtain

$$\nabla^2\mathbf{E} + \frac{\omega^2}{c^2}(\hat{\varepsilon} + \frac{4\pi i}{\omega}\hat{\sigma})\mathbf{E} \simeq 0 \tag{B.3}$$

The solution in this ray approximation is then written as

$$\mathbf{E}(s,t) \simeq \frac{\mathbf{E}(0,t-\frac{s}{c})}{s^2}\theta(t-\frac{s}{c})e^{\frac{\omega}{c}\int_{\mathbf{s}}[i\widehat{n}-\widehat{\Gamma}]\cdot d\mathbf{s}} \tag{B.4}$$

where $\mathbf{s}$ is the path of the ray. By applying this solution to Eq. (B.3) we obtain

$$\widehat{n}^2 = \widehat{\varepsilon}$$

$$\{\widehat{n},\widehat{,}\}_+ = \frac{4\pi}{\omega}\widehat{\sigma}$$

where $\{\}_+$ is the anticommutator. We have assumed that

$$|\frac{\partial(i\widehat{n}-\widehat{,})}{\partial x_i}|\frac{\omega/c}{|i\widehat{n}-\widehat{,}|} \ll 1$$

Equation (B.4) is the solution to Maxwell's equations and will be used to describe the propagation and absorption of the fields generated by the fractal antenna. We must still estimate the dependence of $\widehat{\sigma}$ and $\widehat{\varepsilon}$ on the field E and the validity of the independence of $\widehat{\sigma}$ and $\widehat{\varepsilon}$ in time. Again following [*Gurevich* 1978] we will estimate the dependence of the $\widehat{\sigma}$ and $\widehat{\varepsilon}$ on the field strength by looking at the plasma average velocity and energy. When the field effects become important we will see later that the electron distribution will have a strong directional component with the average plasma velocity $\mathbf{v}$ given by

$$m\frac{d\mathbf{v}}{dt} = -e\mathbf{E} - \frac{e}{c}\mathbf{v}\times\mathbf{B}_o - m\nu_e\mathbf{v}$$

where $\mathbf{E}$ is the oscillating field, and ν_e the averaged collisional frequency with the neutrals. Only collisions with neutrals are relevant at these heights. Similarly, we don't consider transport effects in this region $h \leq 100$ km. Note that without fields, $\mathbf{v}(t) = \mathbf{v}(0)e^{-\nu_e t}$, therefore, the plasma velocity reaches a steady state velocity in $\tau_o \sim \frac{1}{\nu_e}$. For the region of interest, $70 \leq h \leq 90$ km, the background electron-neutral collisional frequency is $\nu_e \geq 10^5$ Hz and increases in the presence

of an electric field. For the case of an oscillating field $\mathbf{E} \sim \mathbf{E}_o e^{i\omega t}$ and a constant magnetic field $\mathbf{B}_o$ the velocity of the plasma is given by

$$\mathbf{v}_e = \frac{eE_o}{m[\Omega_B^2 + (i\omega - \nu_e)^2]}\{(i\omega - \nu_e)\hat{\mathbf{e}} + \frac{\Omega_B^2(\hat{\mathbf{b}} \cdot \hat{\mathbf{e}})}{(i\omega - \nu_e)}\hat{\mathbf{b}} + \Omega_B(\hat{\mathbf{e}} \times \hat{\mathbf{b}})\} \qquad \text{(B.5)}$$

where $\Omega_B = \frac{eB_o}{mc}$, $\hat{\mathbf{e}}$ is the unit vector in the direction of $\mathbf{E}_o$ and $\hat{\mathbf{b}}$ is the unit vector in the direction of $\mathbf{B}_o$. As it can be seen in Eq. (B.1), we can obtain $\hat{\sigma}$ and $\hat{\varepsilon}$ from the plasma current

$$\mathbf{J} = -n_e e\mathbf{v} = \hat{\sigma}\mathbf{E} - \frac{i\omega}{4\pi}(\hat{\varepsilon} - 1)\mathbf{E}$$

The explicit formulas of $\hat{\sigma}$ and $\hat{\varepsilon}$ are not very illuminating, but we are interested in the case in which $\omega \ll \Omega_B, \nu_e$ under the influence of the field. Let's define ϕ to be the angle between the magnetic field and the horizontal. In this approximation the conductivity tensor is

$$\hat{\sigma} \simeq \frac{\omega_o^2 \nu_e}{4\pi(\Omega_B^2 + \nu_e^2)} \begin{pmatrix} 1 + \zeta^2 \cos^2\phi & \zeta \sin\phi & \zeta^2 \frac{\sin 2\phi}{2} \\ -\zeta \sin\phi & 1 & \zeta \cos\phi \\ \zeta^2 \frac{\sin 2\phi}{2} & -\zeta \cos\phi & 1 + \zeta^2 \sin^2\phi \end{pmatrix}$$

and the dielectric tensor is

$$\hat{\varepsilon} - 1 \simeq \frac{\omega_o^2 \nu_e^2}{(\Omega_B^2 + \nu_e^2)^2} \begin{pmatrix} 1 - \zeta^2 + \zeta^2(3 + \zeta^2)\cos^2\phi & 2\zeta \sin\phi & \frac{\zeta^2(3+\zeta^2)\sin 2\phi}{2} \\ -2\zeta \sin\phi & 1 - \zeta^2 & 2\zeta \cos\phi \\ \frac{\zeta^2(3+\zeta^2)\sin 2\phi}{2} & -2\zeta \cos\phi & 1 - \zeta^2 + \zeta^2(3 + \zeta^2)\sin^2\phi \end{pmatrix}$$

where $\omega_o^2 = \frac{4\pi e^2 n_e}{m}$ is the electron plasma frequency, and $\zeta = \frac{\Omega_B}{\nu_e}$. If we take the angle $\phi \simeq 90^o$ and since the electric fields are mostly horizontal for a horizontal fractal discharge, we can finally obtain that

$$\hat{\sigma} \simeq \frac{\omega_o^2 \nu_e}{4\pi(\Omega_B^2 + \nu_e^2)} \begin{pmatrix} 1 & \zeta & 0 \\ -\zeta & 1 & 0 \\ 0 & 0 & 1 \end{pmatrix}$$

If we do not consider the diffraction effects so that $\widehat{\varepsilon} \simeq 1$ (for $\omega_o^2 < \Omega_B^2, \nu_e^2$), then

$$\frac{\omega}{c}\widehat{,} \simeq \frac{\omega_o^2 \nu_e}{2c(\Omega_B^2 + \nu_e^2)} \begin{pmatrix} 1 & \zeta & 0 \\ -\zeta & 1 & 0 \\ 0 & 0 & 1 \end{pmatrix}$$

Therefore, the field power density behaves as

$$E^2(\widehat{\mathbf{r}}s, t) = \frac{E^2(0, t - \frac{s}{c})}{s^2} \theta(t - \frac{s}{c}) e^{-\csc(\chi) \int_0^z K(z, E^2) dz} \tag{B.6}$$

where $K(z, E^2) = \frac{\omega_o^2 \nu_e}{c(\Omega_B^2 + \nu_e^2)}$, $\sin(\chi) = \frac{z}{\sqrt{x^2+y^2+z^2}}$ is the elevation angle of the point $\mathbf{r} = \widehat{\mathbf{r}}s = \{x, y, z\}$ and $\theta(t)$ is the step function. Equation (B.6) is a nonlinear equation for the field power density since the non-Maxwellian nature of the distribution function under an intense electric field (see latter the Fokker-Planck formalism) is incorporated through $\nu_e = \nu_e(z, |E|)$. The propagation of the fields through the lower ionosphere is computed including the loss due to self-absorption. This is how the field changes the properties of the medium. We will assume that the field power density is below the ionization threshold so that we don't have to estimate the time spatio-temporal dependence of the electron density.

B.2 Electron Distribution and the Fokker-Planck Approach

The plasma distribution function in the presence of an electric field is strongly non-Maxwellian, therefore, a kinetic treatment to compute the electron distribution function must be used. The kinetic treatment will be necessary to find the

relevant parameters for the field propagation, such as the averaged total electron-neutral collisional frequency $\nu_e = \nu_e(z, |E|)$, or for the optical emissions, such as the excitation rates of the different electronic levels. We use an existing Fokker–Planck code, which has been developed for the description of ionospheric RF breakdown [*Short et al.* , 1990; *Tsang et al.*, 1991; *Papadopoulos et al.*, 1993a], and later used for studying such phenomena as a triggered atmospheric breakdown [*Papadopoulos et al.*, 1993b], and remote photometry of the atmosphere [*Papadopoulos et al.*, 1994]. The code includes electron energization by collisional absorption of the EM power in the presence of inelastic losses due to molecular N_2 and O_2. It has been an invaluable tool in producing a fully kinetic description of ionospheric EM breakdown and has been successfully benchmarked against the experimental data. The Fokker-Planck formalism [*Gurevich* 1978] starts by taking the spatially homogeneous Boltzmann equation

$$\frac{\partial f}{\partial t} - e(\mathbf{E} + \frac{1}{mc}\mathbf{v} \times \mathbf{B}_o) \cdot \frac{\partial f}{\partial \mathbf{v}} = S|_{coll} \tag{B.7}$$

For a weekly ionized plasma the distribution of electrons is mainly governed by the interaction with neutrals, therefore, the electron-neutral collisional term

$$S|_{coll} = \int\int d\mathbf{v}_1 d\Omega \frac{d\sigma(\theta,\phi)}{d\Omega} |\mathbf{v} - \mathbf{v}_1| \{f(\mathbf{v})F(\mathbf{v}_1) - f(\mathbf{v}')F(\mathbf{v}_1')\} \tag{B.8}$$

include all the elastic and inelastic losses due to collisions with the neutrals. In this collision integral, $F(\mathbf{v})$ is the distribution function of the neutrals in the atmosphere, v′ and v are the velocity of the electron before and after the collision, v_1' and v_1 are the velocity of the neutral before and after the collision. The Scattering cross-section $\frac{d\sigma(\theta,\phi)}{d\Omega}$ relates the angles between the initial $v'-v_1'$ and final $v-v_1$ relative velocities. In the presence of an electric field, we expand

the Boltzmann equation in terms of directional terms [*Gurevich* 1978]

$$f(\mathbf{v},t) = f_o(\mathrm{v},t) + \frac{\mathbf{v}}{\mathrm{v}} \cdot \quad \mathbf{f}_1(\mathrm{v},t) + ...$$

By taking the zeroth and first velocity moments, i.e. integrate the angular variables over the shell $|\mathbf{v}| = \mathrm{v}$, of the resulting equation we obtain

$$\frac{\partial f_o}{\partial t} - \frac{e}{3m\mathrm{v}^2}\frac{\partial}{\partial \mathrm{v}}(\mathrm{v}^2\mathbf{E}\cdot\mathbf{f}_1) = S_0|_{coll} \tag{B.9}$$

$$\frac{\partial \mathbf{f}_1}{\partial t} - e\mathbf{E}\frac{\partial f_o}{\partial \mathrm{v}} - \frac{e}{mc}\mathbf{B}_o \times \mathbf{f}_1 = \mathbf{S}_1|_{coll} \tag{B.10}$$

where $S_0|_{coll} = \int d\Omega S|_{coll}$ and $\mathbf{S}_1|_{coll} = \int d\Omega \frac{\mathbf{v}}{\mathrm{v}} S|_{coll}$ are the collisional integrals respectively.

Since for weakly ionized plasmas the first moment of the collisional integral will converge faster than the zeroth moment [*Huang*, 1987], we expect that $S_1|_{coll} = -\nu(\mathrm{v})\mathbf{f}_1$, which is usually the closure scheme for expansion series of the above form. Such form for the first moment of the collisional integral is also suggested by the fact that the electron speed is larger than the neutral speed. The velocity dependent effective collisional frequency $\nu(\mathrm{v}) = N\mathrm{v}\sigma_{tot}(\mathrm{v})$ includes both elastic and inelastic processes, and σ_{tot} is the effective transport cross section. The elastic contribution to the collisional integral gives [*Gurevich* 1978]

$$S_0^e|_{coll} = \frac{1}{2\mathrm{v}^2}\frac{\partial}{\partial \mathrm{v}}\{\mathrm{v}^2\delta_e\nu(\mathrm{v})[\frac{kT}{m}\frac{\partial f_o}{\partial \mathrm{v}} + \mathrm{v}f_o]\} \tag{B.11}$$

where T is the temperature of the neutrals, and δ_e is the fraction of the electron energy lost in an inelastic collision. The total inelastic collision term is written as a sum of the following processes: rotational, vibrational, optical, dissociation, attachment (including dissociative and three-particle process), and ionization

$$S_0^i|_{coll} = L_{rot} + L_{vib} + L_{opt} + L_{dis} + L_{att} + L_{ion}$$

We use Eq.(B.8) adapted for discrete energy transitions to obtain the vibrational, dissociation and optical loses written as

$$L = L_{vib}+L_{opt}+L_{dis}+L_{rot} = -\frac{2}{m\mathrm{v}}\sum_{l,j,k} N_k[(\epsilon+\epsilon_{kj})f_o(\epsilon+\epsilon_{kj})\sigma_{kj}(\epsilon+\epsilon_{kj})-\epsilon f_o(\epsilon)\sigma_{kj}(\epsilon)]$$

representing loss due to a transition (excitations and de-excitations) from the state $k \to k+j$ and a gain due to a transition that ends with an electron energy ϵ. The σ_{ij} are the total cross sections for the respective processes.

The attachment loss term is

$$L_{att} = -(N_{O_2}\sigma_{att2}(\mathrm{v}) + N_{O_2}^2\sigma_{att3}(\quad \mathrm{v}))\mathrm{v}f_o$$

which includes dissociative attachment (1st term) along with triple attachment (2nd term).

The losses due to ionization are given by

$$L_{ion} = \sum_k N_k \int_{\nu_{ion}}^{\infty/3} \sigma_{ion}(\mathrm{v},\mathrm{v}')f_o(\mathrm{v}')d\mathrm{v}'$$

with $\mathrm{v}_{ion} = \sqrt{2\epsilon_i/m}$ and ϵ_i the ionization energy. In this case the solution to Eq. (B.10) is $\mathbf{f}_1 = -\mathbf{u}(\mathrm{v})\frac{\partial f_o}{\partial \mathbf{v}}$ with $\mathbf{u}(\mathrm{v})$, the directed electron velocity, satisfying

$$\frac{d\mathbf{u}}{dt} = -\frac{e\mathbf{E}}{m} - \frac{e}{mc}\mathbf{u}\times\mathbf{B}_o - \nu(\mathrm{v})\mathbf{u}$$

and the solution is given by Eq.(B.5), from which we derive that

$$\mathbf{u}\cdot\mathbf{E} = \frac{eE_o^2\nu}{m[\Omega_B^2+\nu^2]}\{1+\frac{\Omega_B^2}{\nu^2}\cos^2\theta_o\}$$

Therefore, the Fokker-Planck equation for the oscillating electric field is given by

$$\frac{df_o}{dt} - \frac{1}{3m\mathrm{v}^2}\frac{\partial}{\partial \mathrm{v}}(\mathrm{v}^2\nu(\mathrm{v})\widetilde{\epsilon}(E,\nu(\mathrm{v}))\frac{\partial f_o}{\partial \mathrm{v}}) = S_0|_{coll} \qquad \text{(B.12)}$$

where $\widetilde{\epsilon}(E,\nu) = \frac{e^2 E_o^2}{2m[\Omega_B^2+\nu^2]}\{1 + (\frac{\Omega_B}{\nu})^2 \cos^2\theta_o\}$ is the quiver energy that depends nonlinearly on the collisional frequency ν, the field E_o and the height h in the atmosphere. The averaged electron-neutral collisional frequency over the resulting distribution function is then denoted by ν_e.

The Fokker-Planck equation, given by Eq.(B.12), is solved numerically. The major assumption involved in the derivation of Eq.(B.12) are:

- The plasma is locally uniform, and spatial diffusion operates on much longer time scales than the time it takes for the distribution function to reach a steady state, so transport may be neglected

- The fractional ionization is low, so electron-electron and electron-ion elastic collisions, as well as detachment and recombination, may be ignored.

- The number of molecules in excited states is low, so superelastic collisions are unimportant.

We must now relate the results from Eq.(B.12) to the spatio-temporal field. The spatial variable does not affect the model since transport has been neglected, and the field is below the ionization threshold. Some relevant issues to notice:

- Since $\omega < \Omega_e, \nu_e$, the Fokker-Planck equation does not depend on the frequency ω of the field.

- In the absence of a field, the distribution function relaxes in a time $T_f \sim \frac{1}{\delta_e \nu_e}$ as can be inferred from Eq. (B.11). If $\omega < \delta_e \nu_e$ then the distribution function very quickly reaches a steady state in the presence of the slowly varying field $E_o^2 = E^2(x,t)$. On the other extreme, if $\omega > \delta_e \nu_e$ then the field is too fast for the electrons to catch up and the distribution

function also settles in a steady state in the presence of the field for which $E_o^2 = \frac{1}{T}\int E^2(x,t)dt$, i.e. the time envelope of the mean root square of the field. Hence, we expect that the distribution function will reach a steady state very quickly. In fact, we checked that for the heights of interest, the distribution function did reach a steady state in a time scale $T_p < \frac{1}{\omega} \sim 10$ μsec. Therefore, we can take the input field E_o^2 to the Fokker-Planck equation to be the instantaneous field $E^2(x,t)$.

- The type of electron distribution function generated are highly non-Maxwellian and can be found in *Tsang et al.* [1991]. There are two ways of examining the results of Eq. (B.12). The solutions to Eq. (B.12) can be parametrized in two ways. We can specify the altitude h and the electric field amplitude E_o^2. The alternative is to find the collision frequency $\nu_e(E_0, z)$ explicitly from the Fokker-Planck code, and proceed with the self-similar solution for f(v) as a function of $\tilde{\varepsilon}$. Under the steady state regime, the quiver energy $\tilde{\epsilon}(E, \nu_e)$,with ν_e as the averaged electron-neutral collisional frequency, serves as an excellent parametrization of the steady state distribution function. The quiver energy $\tilde{\epsilon} = \frac{e^2E^2(h)}{2m[\Omega_B^2+\nu_e^2(\tilde{\epsilon})]}\{1 + (\frac{\Omega_B}{\nu_e(\tilde{\epsilon})})^2\cos^2\theta_o\}$ becomes an implicit function of the height and the field strength [*Papadopoulos et al.*, 1993a].

- In the equations for $\hat{\sigma}$ and $\hat{\varepsilon}$, we use the value $\nu_e(E,h) = \nu_e(\tilde{\epsilon})$.

All of the above assumptions are well satisfied for the electric field intensities expected. In addition, in the implementation of the numerical solution, the neutral atmosphere is assumed to consist of molecular oxygen and nitrogen only, excluding trace neutral constituents. Finally, using the Fokker-Planck code with

the electric field distribution from the fractal antenna including the absorption, the intensities of the spatio-temporal optical emissions will be obtained.

B.3 Optical Emissions of $N_2(1P)$

Consider the excitation of the 1st positive ($B^3\Pi_g$) level of molecular nitrogen N_2 which has an excitation energy of 7.35 eV, and a lifetime of 8 μ sec. The emission from the 1st positive band is predominantly in the red. The other relevant line in the red part of the spectrum is the $b'\Sigma_g^+$ of molecular oxygen O_2 which has an excitation energy of 1.63 eV, but a very long lifetime of 12 sec, and it is collisionally quenched at the relevant heights. We can compute the excitation rate of the 1st positive of N_2 from the Fokker-Planck code for a given field power density

$$\nu_{ex}^{1p} = 4\pi N_{N_2} \int f(\mathrm{v})\mathrm{v}^3 \sigma_{ex}^{1p}(\mathrm{v}) d\mathrm{v}$$

where σ_{ex}^{1p} is the excitation cross-section. Under a steady state situation, which is consistent with the lifetime $\tau = 8\mu$ sec of this N_2(1P), the excitations are then followed by optical emissions where the number of photons emitted per sec, per cm^3 is given by $\nu_{ex}^{1p} n_e$ for an given electron density n_e. In order to compare with observations, we will need to average the number of photons in this band at a given position in space over a time Δt. Hence

$$< \nu_{ex}^{1p} n_e >= \frac{1}{\Delta t} \int_0^{\Delta t} \nu_{ex}^{1p}[E(t)] n_e dt$$

The intensity of the radiative transition in Rayleighs is then given by

$$I(R) = \frac{10^{-6}}{4\pi} \int < \nu_{ex}^{1p} n_e > dl \qquad \text{(B.13)}$$

where the integral is carried along the visual path of the detector (column integrated). Therefore, a Rayleigh (R) is the number of photons per sec per cm^2 column integrated and normalized to 10^6 photons.

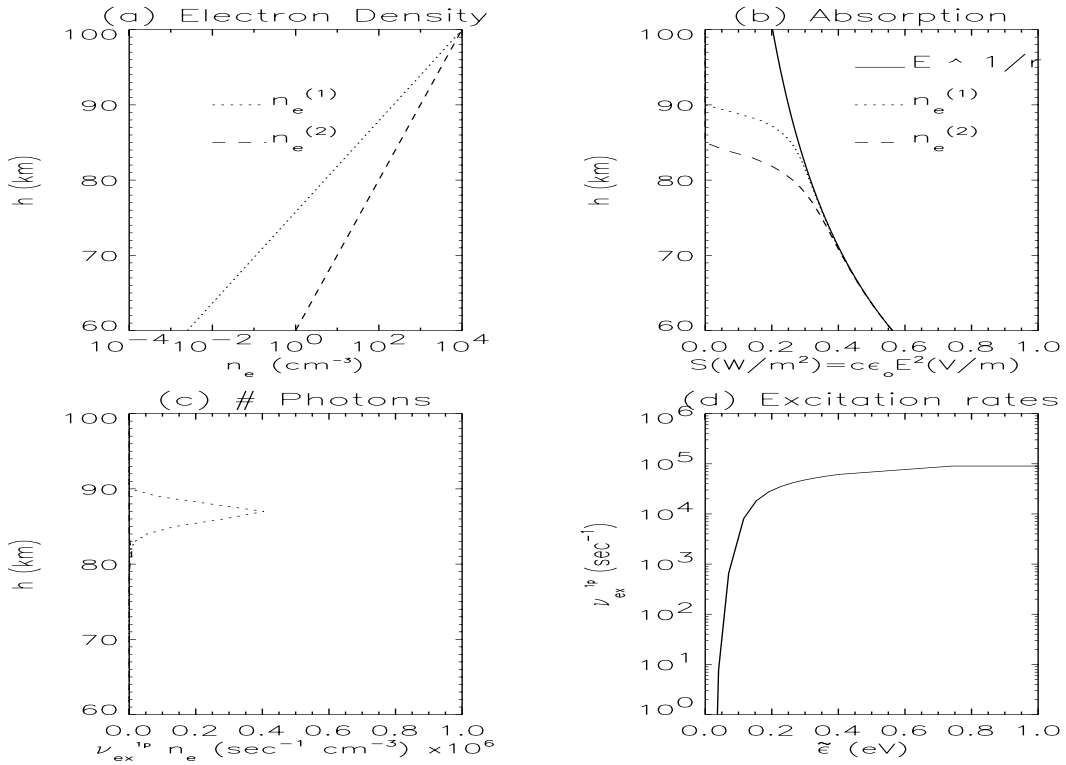

Figure B.1: (a) The two electrond density profiles as a function of heigh. (c) The absoption of the E field is followed by optical emissions of the N_2 (1P). (d) The exitation rates. Plots correspond to the tenous night-time $n_e^{(1)}$ electron density profile (dotted line) and dense night-time $n_e^{(2)}$ electron density profile (dashed line).

Consider first the field due to a point radiator, i.e. $E \sim \frac{E_o}{h} e^{i\omega t}$, we can then compute the field propagation including self-absorption, as shown in Fig B.1b, for the two electron density n $_e$ profiles shown in Fig. B.1a, typical tenuous and dense electron density profiles respectively. Similarly, we can compute the optical

emission intensity for the two profiles as shown in Fig. B.1 c. The excitations rates of $N_2(1P)$ for the different altitudes is given in Fig. B.1d as a function of the power density S(W/m^2)=cε_oE^2(V/m).

From now on we take the tenuous electron density profile $n_e = n_e^{(1)}$. We can compute the height dependent field propagation and photon emissions using this simple monopole model for different electric power density profiles starting at the height $h = 60$ km. Figure B.2 shows the field propagation and emissions for different field strengths propagating from h=60 km. It gives us an idea of the electric field power intensity required to produce observable emissions.

B.4 Ionization Threshold

As we commented above, the quiver energy $\tilde{\epsilon}$ can parametrize the steady state distribution function. As we increase the power density $S(W/m^2)$, we will reach a threshold value of $\tilde{\epsilon}$ where the electrons will gain enough energy to induce significant ionization. This threshold value occurs at $\tilde{\epsilon}(eV) = 1.7\,(2\pi\times 10^6)^2 \frac{\mathrm{E}^2(V/m)}{[\Omega_B^2+\nu_e^2]}\{1+(\frac{\Omega_B}{\nu_e})^2\cos^2\theta_o\} \sim 0.1$ eV [*Papadopoulos et al.*, 1993a] which can be computed at a given height and electric power density.

Taking $\theta_o = \pi/2$, we can estimate the power density required at h=60 km, from our point radiator model, to produce ionization at some height above 60 km. Of course ionization will not occur at h=60 km for these power densities, but assuming the propagation shown in Fig. B.2 we can estimate whether ionization will occur at a higher height for a given field strength at h=60 km. Figure B.3 shows the quiver energy height profile for the field profiles shown in Fig. B.2. Therefore, the ionization threshold will be reached at some height ($h \sim 90$ km)

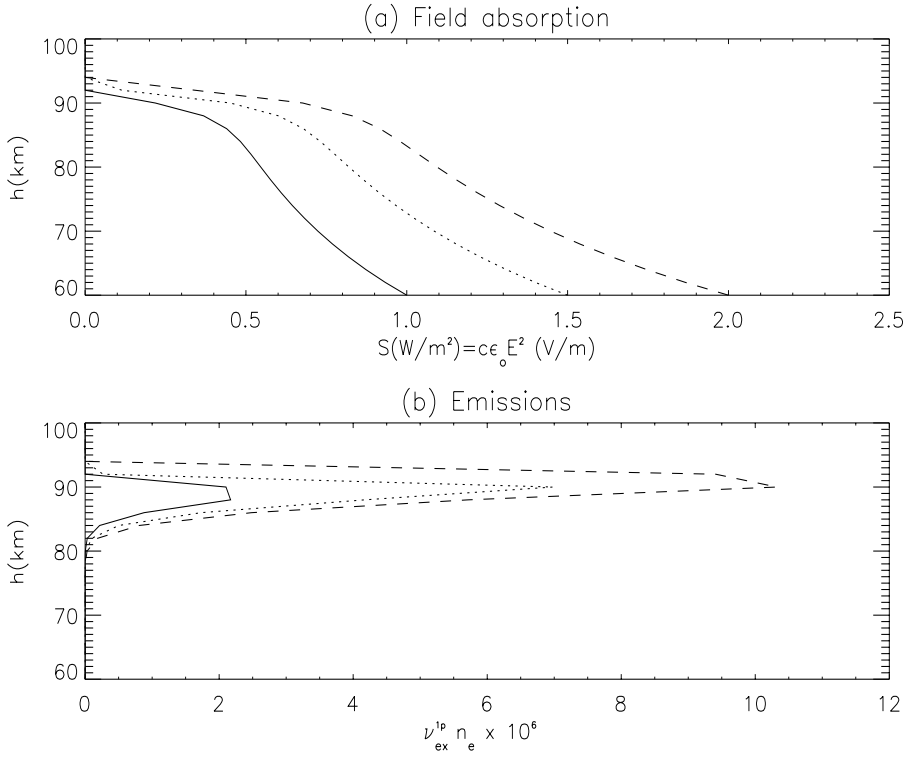

Figure B.2: (a) The field propagation for the point dipole model as a function of height for different power densitties hitting h=60 km. (b) The emissions produced by the fields shown in part (a). The three curves correspond to different field power densities at $h = 60$ km as seen in Fig. B.2.

if $S \simeq 2$ W/m^2 at a height of $h = 60$ km.

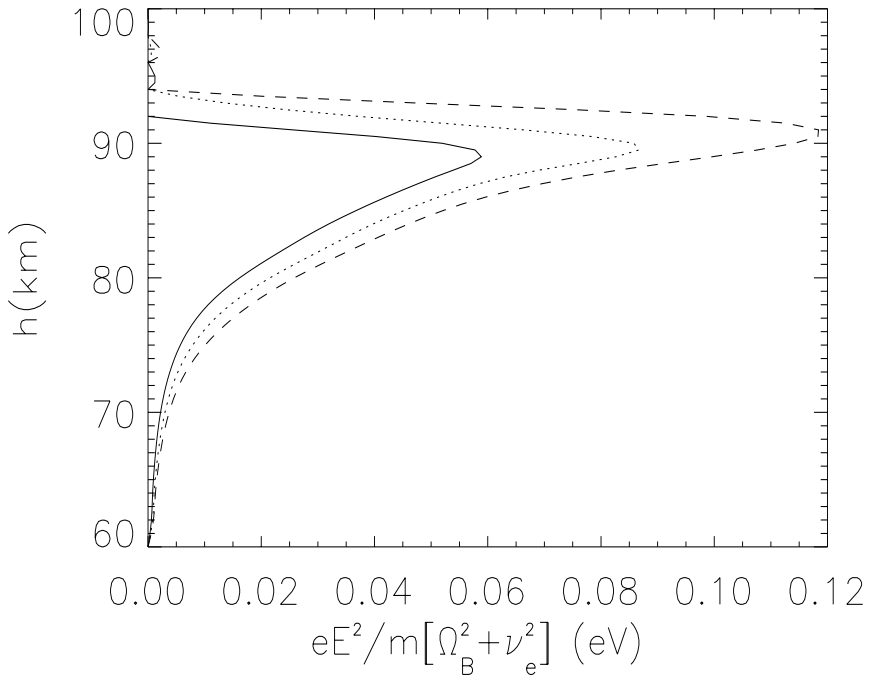

Figure B.3: The quiver energy as a function of height for the field intensities shown in Fig. B.2a. The three curves correspond to different field power densities at $h = 60$ km corresponding to Fig. B.2.

Appendix C

Population of N_2 Levels

The electron energization is computed with the help of the Fokker-Planck code (described in Appendix B). For definiteness we assume that the emission region is located at $z = 80$ km [*Lyons* , 1994; *Sentman et al.*, 1995; *Bossipio et al.*, 1995; *Winckler et al.*, 1996].

C.1 Computing the Radiative Intensity

In the current model we have retained only the electronic levels of N_2 shown in Fig. C.1. The computation of the intensity of a radiative transition connecting the v-th and v′-th vibrational levels of electronic states α and β is accomplished as following. We first compute the excitation rate ν_{ex}^{α} of the α electronic level of N_2 by electron impact

$$\nu_{ex}^{\alpha} = 4\pi N \int f(\mathrm{v})\mathrm{v}^3 \sigma_{ex}^{\alpha}(\mathrm{v}) d\mathrm{v}$$

using the excitation cross section of the B, B′, W, C and E electronic levels by electron impact from *Cartwright et al.* [1977]. While the excitation cross section of the $N_2(D)$ electronic level is taken from *Freund* [1971] and normalized by

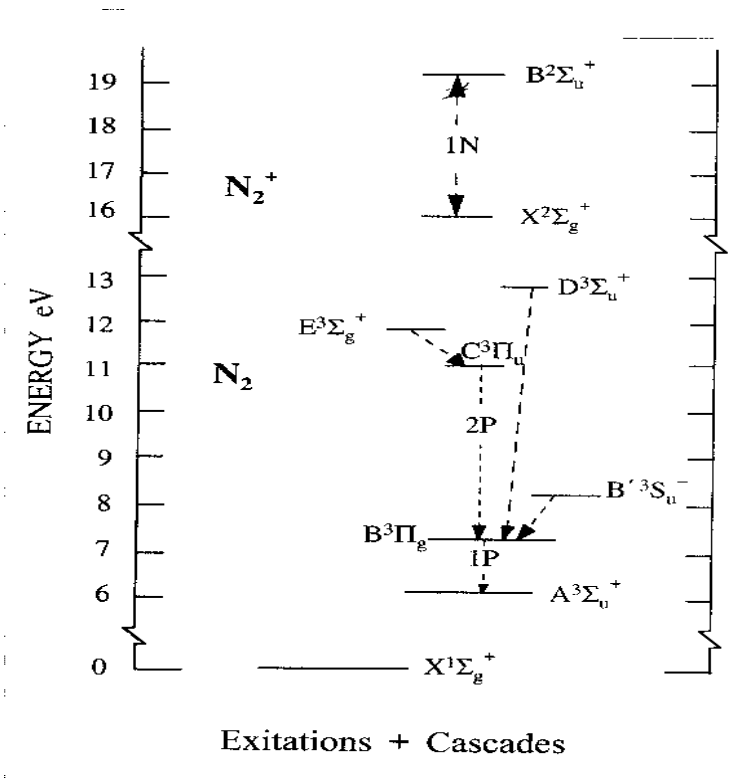

Figure C.1: Energy levels diagram for the nitrogen electronic levels considered in the discussed model. The relevant radiative transitions are shown by arrows

using the peak value from *Cartwright* [1970]. The excitation cross section of the $N_2^+(B)$ electronic level by the electron impact from the ground state was taken from *Van Zyl and Pendleton* [1995].

Figure C.2 shows the excitation rates for the relevant electronic levels of N_2 as a function of the electric field E_o at this height $z = 80$ km. We have neglected effects caused by the W$\rightarrow$B transition compared with that due to the B$\rightarrow$ B' transition, both having similar excitation threshold but different excitation rates as revealed by Fig (C.2). We then obtain the population of vibrational levels inside each of the electronic states by solving the following set of stationary

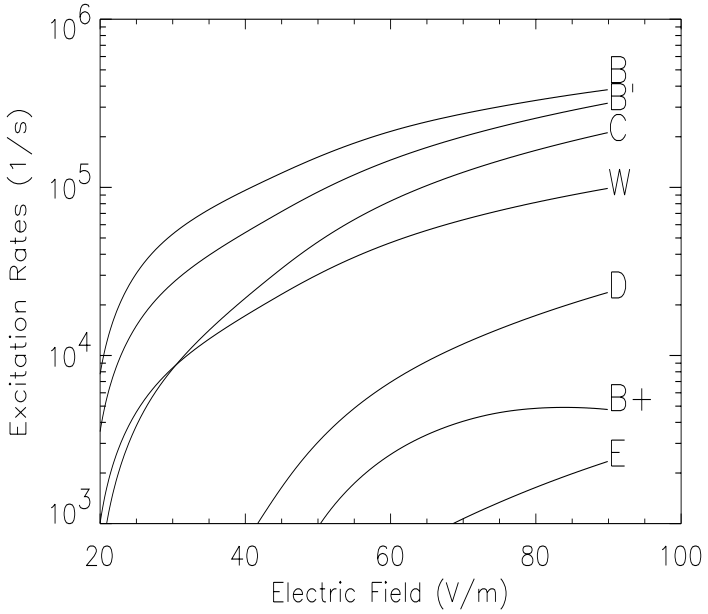

Figure C.2: The excitation rates for the different leves: B, B', W, C, E. for the h = 80 km.

equations [*Cartwright*, 1978]

$$\frac{dn_v^\alpha}{dt} = q_{ov}^{xa}\nu_{ex}^\alpha n_e + \sum_{\beta j} A_{jv}^{\alpha\beta} n_j - n_v^\alpha \sum_{\beta j} A_{vj}^{\alpha\beta} - k_{q,v}^\alpha N n_v^\alpha = 0 \qquad \text{(C.1)}$$

where:

- n_e is the electron density,
- n_j^α is the number density of the v-th vibrational level of electronic state α,
- q_{ov}^{xa} is the Franck-Condon factor which shows the transition probability to the v vibrational level of the α electronic state from the 0 vibrational level of the ground state X (in a cold ambient gas only the lowest vibrational level is populated),

- $A_{vv'}^{\alpha\beta}$ is the Einstein spontaneous transition probability,
- $k_{q,v}^{\alpha}$ is the rate constant of collisional quenching of the v vibrational level of the α electronic state
- N is the air density.

Therefore, the first term in the right side of Eq. (C.1) shows the direct pumping of the v vibrational level of the α electronic state by the electron impact. While the second term shows cascade excitation, the third term describes the radiation losses. The last term reveals losses due to the collisional quenching. Note that the usage of the stationary equations for the population of vibrational level is justified by the fact that radiative lifetime of the relevant electronic states have to be shorter than the duration T of electromagnetic pulse from lightning in order to be effectively pumped. Therefore, a stationary distribution of n_v^{α} is established during the pulse.

From Eq. (C.1) we obtain now the population of the α electronic level as

$$n_v^{\alpha} = \nu_{ex}^{\alpha} n_e F_{1,v}^{\alpha} + \sum_{\beta} \nu_{ex}^{\beta} n_e F_{2,v}^{\alpha\beta}$$

$$F_{1,v}^{\alpha} = \frac{q_{ov}^{xa} \tau_v^{\alpha}}{1 + \tau_v^{\alpha} k_{q,v}^{\alpha} N}$$

$$F_{2,v}^{\alpha\beta} = \frac{\tau_v^{\alpha}}{1 + \tau_v^{\alpha} k_{q,v}^{\alpha} N} \sum_{j} F_{1,j}^{\alpha} A_{jv}^{\alpha\beta} \qquad \text{(C.2)}$$

here $\tau_v^{\alpha} = 1/\sum_{j\beta} A_{vj}^{\alpha\beta}$ is lifetime of v-th vibrational level of the α electronic state. The coefficients $F_{1,v}^{\alpha}$ and $F_{2,v}^{\alpha\beta}$ reveal relative importance of the direct and cascade excitation of v-th vibrational level of state α, and are calculated using the data from Gilmore et al., [1992]. Moreover, the quenching factor $(1 + \tau_v^{\alpha} k_{q,v}^{\alpha} N)^{-1}$ was calculated for the relevant electronic levels using the quenching rate coefficient

recently revised by *Morill and Benesh* [1996], see Fig (C.3). The calculation revealed that the collisional quenching can be neglected at heights above 70 km, since the photon of all three bands of interests $N_2(1P)$, $N_2(2P)$, $N_2^+(1N)$ is not affected by the collisions.

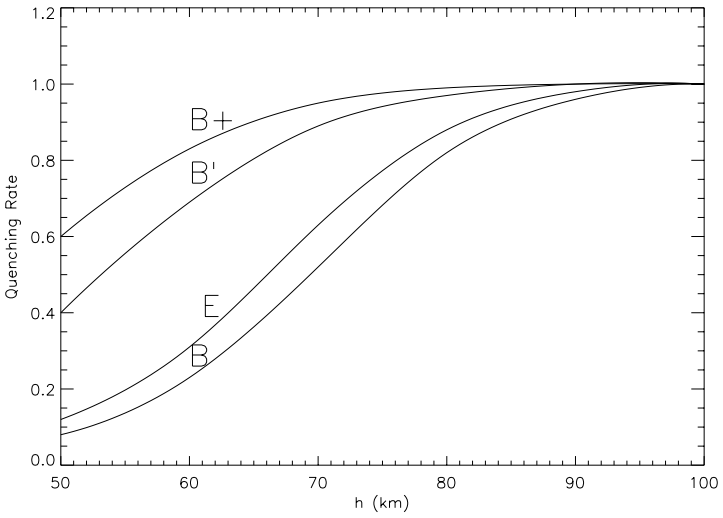

Figure C.3: The effective quenching factor for the transitions of interest: B, B', C, D

Note that collisional transfer between the N_2(B) and other excited N_2 states could affect the N_2 optical spectrum [*Morill and Benesh*, 1996] and is an important issue for quasistationary auroras. However, in order to affect sprite spectra, the collisions has to occur faster than the duration of a sprite, T$\sim$ 10 msec, which requires that the density of the excited nitrogen molecules to be larger than $\frac{1}{k_{tr}T} \simeq 2.5 \times 10^{12}$ cm^{-3}. (Here the collision rate coefficient is assumed to be $k_{tr} \simeq 4 \times 10^{-11}$ cm^{3}s^{-1} [*Morill and Benesh* 1996]). To produce such significant abundance of the electronically excited molecules about 10^9 J km^{-3} has to be released. Such value limits the application of the above effect to some local

spots, since the total energy released when a charge of hundreds of Coulombs is transferred from cloud to ground is about 10^{11} J [*Uman* , 1987], and only a small fraction of this energy is absorbed in the ionosphere producing the red sprite.

The intensity of the radiative transition in Rayleighs connecting the v-th and v′-th vibrational levels of electronic states α and β by

$$I^{\alpha\beta}_{\nu\nu'}(\lambda) = \frac{10^{-6}}{4\pi} \int n^{\alpha}_{v} A^{\alpha\beta}_{vv'} dl \tag{C.3}$$

A similar scheme is applied in order to obtain intensities of the $N_2(2P)$ and the $N_2^+(1N)$ bands from which we obtain the spectrum $I_s(E_o, \lambda)$.

C.2 Atmospheric Attenuation

The observed spectrum depends on the location of the detector. If observed from space, the spectrum is the same as the source spectrum $I_s(E_o, \lambda)$, while if observed from either ground or airplane it will be distorted by atmospheric attenuation. Atmospheric attenuation depends on the zenith angle χ of the optical source, the altitude h_o of the detector, and on the properties of the atmosphere, such as relative humidity and aerosol density. We consider the following contributions to the attenuation: absorption by ozone, oxygen and water vapor, the Rayleigh scattering by air molecule, and Mie scattering by aerosols. The total attenuation of the optical emission is the result of the above contributions and is given by

$$I(h, \chi, \varepsilon, \lambda) = I_s(\varepsilon, \lambda) e^{-\tau(h, \chi, \varepsilon, \lambda)} \tag{C.4}$$

$$\tau(h, \chi, \varepsilon, \lambda) = \sec \chi \sum_s \sigma^s_{abs}(\lambda) \int_h^{h_o} N_s(z) dz$$

where h_o is the altitude of the sprite, I_s is the sprite source spectrum shown in Fig (4.1), $\sigma^s_{abs}(\lambda)$ is the corresponding effective wavelength dependent attenuation cross section, and N_s (z) is the density of particles that absorb or scatter the photons:

- The absorption by molecular oxygen is computed by taking into consideration the fact that the absorption spectrum of O_2 has four narrow peaks centered at λ = 6872, 6893, 7608 and 7638 A [*Greenblatt et al.* , 1990].

- The absorption by ozone is computed using the absorption cross-section from *Lenoble* [1993], and applying the mid-latitude ozone model [*Bresseur and Solomon*, 1984].

- The absorption caused by the water vapor is calculated using the cross section from *Lenoble* [1993]. We assume 80% relative humidity, take the dependence of the water vapor pressure on the temperature from *Handbook of Chemistry and Physics* [1983, Fig. 18–13], and assume also that the temperature in the troposphere follows the profile observed at Wallops Island (38 N^o) during summer time [*Handbook of Geophysics*, 1985, Fig. 15–13].

- The Rayleigh scattering was calculated using the wavelength dependence of the cross section given by *Nicolet et al.* [1982].

- Finally the Mie scattering was calculated by assuming the vertical distribution of the aerosol attenuation (at 0.55 μm) from the background spring-summer model [*Handbook of Geophysics*, 1985, pg. 18–13], and then we

extend the attenuation to any wavelength by using the tropospheric aerosol model [*Handbook of Geophysics*, 1985, Fig. 18–21]. For the sake of definiteness we assumed 5,000 particles/cm^3 number density of aerosols.

Bibliography

[1] Bell, T. F., V. P. Pasko, and U. S. Inan, Runaway electrons as a source of Red Sprites in the mesosphere, *Geophys. Res. Lett.*, 22, 2127–2130, 1995.

[2] Bethe, H. A., and J. Ashkin, Passage of radiations through matter, in *Experimental Nuclear Physics* (ed. E. Segre) Wiley, New York 1953, pp. 166–357.

[3] Boeck, W. L., O. H. Vaughan, Jr., R. Blakeslee, B. Vonnegut, and M. Brook, Lightning induced brightening in the airglow layer, *Geophys. Res. Letts.*, 19(2), 99–102, 1992.

[4] Bossipio, D. J., E. R. Williams, S. Heckman, W. A. Lions, I. T. Baker, and R. Boldi, Sprites, ELF transients, and positive ground strokes, *Science*, 269, 1088–1091, 1995.

[5] Brasseur, G., and S. Solomon, Aeronomy of the Middle Atmosphere, D. Reidel, Norwell, Mass., 1984.

[6] Cartwright, D. C, Total Cross Sections for the Excitation of the Triplet States in Molecular Nitrogen, *Phys. Rev., A2*, 1331–1347, 1970.

[7] Cartwright, D. C, S. Trajamar, A. Chutjian, and W. Williams, Electron impact excitation of the electronic states of N2. II. Integral cross sections at incident energies from 10 to 50 eV, *Phys. Rev., A*16, 1041–1051, 1977.

[8] Cartwright, D. C., Vibrational Populations of the Excited States of N2 Under Auroral Conditions, *J. Geophys. Res.*, A83, 517–531, 1978.

[9] Connor, J. W., and R. J. Hastie, Relativistic limitation on runaway electrons, *Nucl. Fusion*, 15, 415–424, 1975.

[10] Daniel, R. R., and S. A. Stephens, Cosmic-ray-produced electrons and gamma rays in the atmosphere, *Rev. Geophys. Space Sci.*, 12, 233–258, 1974.

[11] Dreicer, H., Electron and ion runaway in a fully ionized gas. II, *Phys. Rev.*, 117, 329–342, 1960.

[12] Farrel, W. M., and M. D. Desch, Cloud-to-stratosphere lightning discharges: a radio emission model, *Geophys. Res. Lett.*, 19(7), 665–668, 1992.

[13] Farrel, W. M., and M. D. Desch, Reply to comment on "Cloud-to-stratosphere lightning discharges: a radio emission model", *Geophys. Res. Lett.*, 20(8), 763–764, 1993.

[14] Femia, H., L. Niemeyer, V. Tucci, Fractal Characteristics of electrical discharges: experiments and simulations, *J. Phys. D: Appl. Phys.*, 26, p. 619, 1993.

[15] Fishman, G. J., P. N. Bhat, R. Mallozzi, et al., Discovery of intense gamma-ray flashes of atmospheric origin, *Science*, 264, 1313–1316, 1994.

[16] Franz, R. C., R. J. Memzek, and J. R. Winckler, Television image of a large upward electrical discharge above a thunderstorm system, *Science*, 249, 48–51, 1990.

[17] Freund, R. S., Electron Impact and Excitation Functions for the and States of N2, *J. Chem. Phys.*, 54, 1407-1409, 1971.

[18] Gilmore, F. R., R. R. Laher, and P. J. Espy, Franck-Condon factors, r-centroids, electronic transition moments, and Einstein coefficients for many nitrogen and oxygen systems, *J. Phys. Chem.* Ref. Data, 21, 1005–1067, 1992.

[19] Goodman, J. W., *Statistical Optics*, Wiley-interscience, 1985.

[20] Greenblatt, G. D., J. J. Orlando, J. B. Burkholder and A. R. Ravishankara, Absorption Measurements of Oxygen between 330 and 1140 nm, *J. Geophys. Res.*, 95, 18,577–18,582, 1990.

[21] Gurevich, On the theory of runaway electrons, *JETP*, 39, 1996–2002, 1960; *Sov. Phys. JETP*, 12, 904–912, 1961.

[22] Gurevich, A. V., *Nonlinear phenomena in the Ionosphere*, Springer, 1978

[23] Gurevich A. V., G. M. Milikh, and R. Roussel-Dupre, Runaway electrons mechanism of the air breakdown and preconditioning during thunderstorm, *Phys. Lett. A*, 165, 463, 1992.

[24] Gurevich A. V., G. M. Milikh, and R. Roussel-Dupre, Nonuniform runaway breakdown, *Phys. Lett. A*, 187, 197, 1994.

[25] Gurevich, A. V., J. A. Valdivia, G. M. Milikh, K. Papadopoulos, Runaway electrons in the atmosphere in the presence of a mangetic field, *Radio Science*, 31, 6, p. 1541, 1996.

[26] Hale, L. C., and M. E. Baginski, Current to the ionosphere following a lightning stroke, *Nature*, 329, 814–816, 1987.

[27] Hampton, D. L., M. J. Heavner, E. M. Wescott, and D. D. Sentman, Optical spectral characteristics of sprites, *Geophys. Res. Lett.*, 23, 89–92, 1996.

[28] *Handbook of Chemistry and Physics*, 64–th Edition, Ed. R. C. Weast, CRC Press, Boca Raton, Florida, 1983–1984.

[29] *Handbook of Geophysics and Space Environment*, 64–th Edition, Ed. A. S. Jursa, Air Force Geophysics Laboratory, US Air Force, 1985.

[30] Huang, K., *Statistical Mechanics*, Wiley, 1987.

[31] Jackson, J. D., *Classical Electrodynamics*, Wiley, 1975.

[32] Jaggard, D. L., On fractal electrodynamics, In *Recent Advancements in Electromagnetic Theory*, edited by H. N. Kritikos and D. L. Jaggard, p. 183, Springer-Verlag, New York, 1990.

[33] Kerr, R. A., Atmospheric scientists puzzle over high-altitude flashes, *Science*, 264, 1250–1251, 1994.

[34] Kim, Y., and D. L. Jaggard, The fractal random array, *Proceedings of the IEEE*, 74, 1986.

[35] Krider, E. P., On the electromagnetic fields, pointing vector, and peak power radiated by lightning return strokes, *J. Geophys. Res.*, 97, 15913–15917, 1992.

[36] Krider, E. P., On the peak electromagnetic fields radiated by lightning return strokes toward the middle atmosphere, *J. Atmos. Electr.*, 14, 17–24, 1994.

[37] Le Vine, D. M., and R. Meneghini, Simulations of radiation from lightning return strokes: the effects of tortuosity *Radio Science*, 13, 801–810, 1978.

[38] Lebedev, A. N., Contribution to the theory of runaway electrons, *Sov. Phys. JETP*, 21, 931–933, 1965.

[39] Lenoble, J., *Atmospheric Radiative Transfer*, A. Deepak Publishing, Hampton, Virginia, 1993

[40] Longmire, C. L., On the electromagnetic pulse produced by nuclear expulsion, *IEEE Trans. Antenna Propag.*, 26, 3–13, 1978.

[41] Luther, F. M., and R. J. Gelinas, Effect of molecular multiple scattering and surface albedo on atmosphere photodissociation rate, *J. Geophys. Res.*, 81, 1125–1138, 1976.

[42] Lyons, W. A., Characteristics of luminous structures in the stratosphere above thunderstorms as imaged by low-light video, *Geophys. Res. Lett.*, 21, 875–878, 1994.

[43] Marion, J. B., M. A. Heald, Classical Electromagnetic Radiation, Harcourt Brace Jovanovich, 1980.

[44] McCarthy, M. P., and G. K. Parks, Om the modulation of X-ray fluxes in thunderstorms, *J. Geophys. Res.*, 97, 5857–5864, 1992.

[45] Massey, R. S., and D. N. Holden, Phenomenology of trans-ionoispheric pulse pairs, *Radio Science*, 30(5), 1645, 1995.

[46] Mende, S. B., R. L. Rairden, G. R. Swenson and W. A. Lyons, Sprite Spectra; N2 1 PG Band Identification, *Geophys. Res. Lett.*, 22, 1633–2636, 1995.

[47] Milikh, G. M., K. Papadopoulos, and C. L. Chang, On the physics of high altitude lightning, *Geophys. Res. Lett.*, 22, 85–88, 1995.

[48] Morill, J. S., and W. M. Benesh, Auroral N2 emissions and the effect of collisional processes on N2 triplet state vibrational populations, *J. Geophys. Res.*, 101, 261–274, 1996.

[49] Nemzek,, R. J., and J. R. Winckler, Observation and integration of fast subvisual light pulses from the night sky, *Geophys. Res. Lett.*, 16, 1015–1019, 1989.

[50] Nicolet, M., R. R. Meier, and D. E. Anderson, Radiation Field in the Troposphere and Stratosphere — II. Numerical Analysis, *Planet. Space. Sci.*, 30, 935–941, 1982.

[51] Niemeyer L., L. Pietronero, H. J. Wiesmann, Fractal Dimension of Dielectric Breakdown, *Phys. Rev. Lett.*, 52, 12, p. 1033, 1984.

[52] Ogawa, T., and M. Brook, The mechanism of the intracloud lightning discharge, *J. Geophys. Res.*, 69, 5141–5150, 1964.

[53] Ott, E, *Chaos in dynamical systems*, Cambridge University Press, 1993.

[54] Papadopoulos, K., G. Milikh, A. Gurevich, A. Drobot, and R. Shanny, Ionization rates for atmospheric and ionospheric breakdown, *J. Geophys. Res.*, 98(A10), 17,593–17,596, 1993a.

[55] Papadopoulos, K., G. Milikh, and P. Sprangle, Triggering HF breakdown of the atmosphere by barium release, *Geophys. Res. Lett.*,20, 471–474, 1993b.

[56] Papadopoulos, K., G. Milikh, A. W. Ali, and R. Shanny, Remote photometry of the atmosphere using microwave breakdown, *J. Geophys. Res.*, 99(D5), 10387–10394, 1994.

[57] Papadopoulos, K., G. M. Milikh, J. A. Valdivia, Comment on "Can gamma radiation be produced in the electrical environment above thunderstorms", *Geophys., Res. Lett.*, 23, 17, p. 2283, 1996.

[58] Pasko, V. P., U. S. Inan, Y. N. Taranenko, and T. Bell, Heating, ionization and upward discharges in the mesosphere due to intense quasi-electrostatic thundercloud fields, *Geophys. Res. Lett.*,22, 365–368, 1995.

[59] Rowland, H. L., R. F. Fernsler, and P. A. Bernhardt, Ionospheric breakdown due to lightning driven EMP, submitted to *J. Geophys. Res.*, 1994.

[60] Roussel-Dupre R. A. , A. V. Gurevich, T. Tunnel, and G. M. Milikh, Kinetic theory of runaway breakdown, *Phys Rev. E*, 49, 2257, 1994.

[61] Roussel-Dupre, R. A., A. V., Gurevich, On runaway breakdown and upward propagating discharges, *J. Geophys. Res.*, 101, 2297–2311, 1996.

[62] Royden, H. L., *Real Analysis*, Prentice Hall, 1963.

[63] Sander, L. M., *Fractal growth process*, Nature, 322, 1986.

[64] Sentman, D. D., and E. M. Wescott, Observations of upper atmospheric optical flashes recorded from an aircraft, *Geophys. Res. Lett.*, 20, 2857–2860, 1993.

[65] Sentman, D. D., The middle atmosphere: a porous buffer separating the lower and upper atmospheres (abstract), *EOS Trans. AGU*, 75, Spring Meeting Suppl., p. 49, 1994.

[66] Sentman, D. D., E. M. Wescott, D. L. Osborne, D. L. Hampton, and M. J. Heavner, Preliminary results from the sprites94 aircraft campaign, 1, red sprites, *Geophys. Res. Lett.*, 22, 1205–1208, 1995.

[67] Short, R., P. Lallement, D. Papadopoulos, T. Wallace, A. Ali, P. Koert, R. Shanny, and C. Stewart, Physics studies in artificial ionospheric mirror (AIM) related phenomena, *Tech. Rep.* GL–TR–90–0038, Geophysics Lab., Air Force Systems Command, Hansom Air Force Base, Mass, 1990.

[68] Taranenko, Y., R. Roussel-Dupre, High altitude discharges and gamma-ray flashes: a manifestation of runaway air breakdown, *Geophys., Res. Lett.*, 23, 5, p.571, 1996.

[69] Tsang, K., K. Papadopoulos, A. Drobot, P. Vitello, T. Wallace, and R. Shanny, RF ionization of the lower ionosphere, *Radio Science.*, 20(5), 1345–1360, 1991.

[70] Uman, M. A., *The Lightning Discharge*, Academic Press, Orlando 1987.

[71] Van Zyl, B., and W. Pendleton Jr., , and production in e— + N2 collisions, *J. Geophys. Res.*, 100, 23,755–23,762, 1995.

[72] Vaughan, Jr., O. H., R. Blakeslee, W. L. Boeck, B. Vonnegut, M. Brook, and J. McKune, Jr., A cloud-to-space lightning as recorded by the Space Shuttle payload-bay TV cameras, *Mon. Weather Rev.*, 120, 1459–1461, 1992.

[73] Vecchi, G., D. Labate, F. Canavero, Fractal approach to lightning radiation on a tortuous channel, *Radio Science*, 29, p. 691, 1994.

[74] Werner, D. H., and P. L. Werner, On the synthesis of fractal radiation patterns, *Radio Science,* 30, 29–45, 1995.

[75] Wescott, E. M., D. Sentman, D. Osborne, D. Hampton, M. Heavner, Preliminary Results from the Sprite94 aircraft campaign, 2, blue jets, *Geophys. Res. Lett.*, 22, 10, p.1213, 1995.

[76] Williams, E. R., The electrification of thunder storms, *Scientific American*, 88–99, November 1988.

[77] Wilson, C. T. R., The acceleration of -particles in strong electric fields such as those of thunderclouds, *Proc. Cambridge Phys. Soc.*, 22, 534–538, 1924.

[78] Winckler, J. R., R. C. Franz, and R. J. Nemzek, Fast low–level light pulses from the night sky observed with the SKYFLASH program, *J. Geophys. Res.*, 98(D5), 8775–8783, 1993.

[79] Winckler, J. R., Further observations of cloud-ionosphere electrical discharges above thunderstorms, *J. Geophys., Res.*, 100, 14335, 1995.

[80] Winckler, J. R., W. A. Lyons, T. E. Nelson, and R. J. Nemzek, New high-resolution ground-based studies of sprites, *J. Geophys. Res.*, 101, 6997, 1996.